NTNU
Norwegian University of
Science and Technology

# Study of mist flow inside a vane pack geometry

**Fredrik Carlson**
**Mauritz-Arne Olaisen Talseth**

Master of Science in Energy and Environment
Submission date: June 2009
Supervisor: Maria Fernandino, EPT

Norwegian University of Science and Technology
Department of Energy and Process Engineering

# Problem Description

Background and objective:
Gas-liquid separation is a crucial step in the process of gas conditioning in the oil and gas industry. During the project work in the fall semester 2008, the two candidates performed CFD simulations of a vane pack geometry in order to optimize the design of an existing vane pack device so as to obtain a better separation efficiency. Different turbulence models were tested in a single phase flow and the separation efficiency was evaluated by studying the behaviour of solid particles that were introduced at the inlet of the separation device. As a second part of the project, the two candidates suggested modifications to an existing experimental test facility so that the new proposed geometry could be incorporated into the facility.

Experiments are needed in order to validate the proposed new design of the test section. Experimental measurements should also be complemented by further CFD analysis, this time using more advanced turbulence models and incorporating a liquid dispersed phase instead of solid particles. In this way, the interaction among the particles in the dispersed phase (i.e.: coalescence and breakage) could be taken into account, resulting in a better estimation of the separation efficiency of the proposed vane pack.

The following questions should be considered in the project work:

1. Perform CFD analysis of the proposed vane pack geometry by introducing a liquid phase.
2. Perform measurements after the new test section is constructed.

Assignment given: 20. January 2009
Supervisor: Maria Fernandino, EPT

# Study of mist flow inside a vane pack geometry

**Fredrik Carlson and Mauritz Talseth**

Energy and Environmental Engineering

June 16, 2009

**Master in Science Thesis**

Department of Energy and Process Engineering
**The Norwegian University of**
**Science and Technology**

Associate Professor: **Maria Fernandino**

## Acknowledgements

In the last semester of the master program at The Norwegian University of Science and Technology in Trondheim a master thesis of 30 credits is the closure of the education program. We have chosen the Department of Energy and Process Engineering at the Faculty of Engineering and Technology for the master thesis. This thesis has been written in collaboration between Natco Norway AS and the Norwegian University of Science and Technology.

We would like to take the opportunity to thank people that has helped us made this work possible. First we want to express our sincere thanks to our Principal Supervisor Maria Fernandino at NTNU that has supported us and showed genuine involvement in our thesis.

We would also express our gratitude to the staff at Natco Norway for the great experience and support through the thesis. We would like to thank Bjørn Christiansen for giving us the opportunity for this thesis, Kåre Nordnes and Kenneth Kildal for helping us with software and Knut Sveberg for guidance through the high pressure lab. We would like to direct a special thank to Dag Kvamsdal that has guided and helped us through this thesis, and for his great enthusiasm and fruitful discussions, it has been invaluable. Finally we want to thank Andreas Carlson for his critical comments through this thesis.

Trondheim 16.06.2009

Fredrik Carlson Mauritz Arne Olaisen Talseth

## Abstract

This science in master thesis was a continuation of the project thesis. Vane pack demisters in the industry operate with natural gas at pressures up to 100 bara. At those pressures the gas has high density, this high density was imitated by the use of $SF_6$ gas in the laboratory. A new vane pack has been compared with the traditional one used by the industry. The vane packs have been investigated through experiments and Computational Fluid Dynamics, CFD. The fluid flow inside a vane pack consist of turbulence and two fluid phases. The simulations were carried out with a Large Eddy Simulation model, LES, and a Scale-Adaptive Simulation, SAS, model. Those two models where chosen based on a test simulation. Phenomena observed in the experiments were confirmed by CFD. A transient DPM model that should be capable of modeling the generation of a liquid film together with droplets was used. The turbulent transient DPM simulations gave a mist flow pattern that agreed with the one observed in the laboratory, but did not generate film physics like re-entranment. Since re-entrainment has a large impact on the separation efficiency the efficiency reported from CFD was not representative of the real situation.

Standards for the oil and gas industry, states that the scrubber should have a maximum liquid carry over of 0.1 USgal/MMSCF, this implies a minimum separation efficiency of typically 99.9% or more, for the vane pack. Vane packs are often tested by the manufacturer at low pressure air/water systems. At such conditions, the droplets have large velocity and inertia and the effects of re-entrainment are small, which gives the demisters high efficiencies. A typical sizing factor for vane packs are k-value from 0.2 - 0.25 m/s. Separation efficiency measurements of the two vane packs with Exxsol D60 as liquid and SF6 as gas where performed at different pressures, ranging from 1 to 8 barg. Non of the experiments achieved the specification mentioned above. Efficiencies of 99.9% or more were only achieved at k-values below 0.05 m/s. The efficiency measurements did show that the pressure had a great influence on the performance. The low pressure measurements were the only experiments which had a efficiency above 97% at a k-value between 0.2 - 0.25 m/s.

# Contents

# List of Figures

# List of Tables

# Nomenclature

## Roman Symbols

| | |
|---|---|
| $(\ )_{coarse}$ | coarse grid notation |
| $(\ )_{d}$ | droplet notation |
| $(\ )_{d,\infty}$ | stable droplet notation |
| $(\ )_{fine}$ | fine grid notation |
| $(\ )_{g}$ | gas notation |
| $(\ )_{l}$ | liquid notation |
| $(\ )_{t}$ | throat notation |
| $(\ )^{t}$ | turbulent notation |
| $\overline{(\ )}$ | time averaged |
| $a_{(\ )}$ | constants |
| $B$ | Collision parameter |
| $C_S$ | Smagorinsky constant |
| $C_D$ | drag coefficient |
| $C_{DES}$ | dimensionless constant |
| $C_{vm}$ | virtual mass coefficient |
| $d$ | opening into drainage chamber |
| $D$ | diameter |
| $D$ | fluid domain |
| $D_{d\infty}$ | maximum droplet diameter after fragmentation |
| $D_h$ | hydraulic diameter |
| $E$ | impact energy |
| $f_{d,coal}$ | coalescence frequency |
| $f_i$ | source term |
| $F_{(\ )}$ | Force notation |

| | |
|---|---|
| $F1$ | blending function |
| $F2$ | blending function |
| $F_{SST}$ | blending function |
| $F_{DES}$ | blending function |
| $G$ | Filter function |
| $g$ | gravitational acceleration |
| $l$ | length of bend |
| $l_e$ | turbulent length |
| $I_{turb}$ | turbulence intensity |
| $k$ | turbulent kinetic energy |
| $K$ | K-value |
| $l$ | length |
| $L$ | turbulent length scale |
| $L_t$ | length scale |
| $L_{vk}$ | von Karman length scale |
| $\dot{m}$ | mass rate |
| $n$ | number of bends |
| $n$ | normal coefficient |
| $n_d$ | droplet density number |
| $\dot{n}_{d,(\ )}$ | droplet production term |
| $p$ | pressure |
| $P_k$ | production term |
| $P_\omega$ | production term |
| $P_{SAS}$ | scale adaptive term |
| $Q$ | flow rate |
| $r$ | radius |
| $s$ | standard deviation |
| $s$ | height in vane pack channel |
| $s'$ | height in vane pack channel |
| $S_{ij}$ | strain rate tensor |
| $u$ | instantaneous velocity in direction $i$ |
| $u_{rel}$ | relative velocity |
| $U$ | mean velocity vector |
| $u'$ | fluctuating velocity vector |

| | |
|---|---|
| $U_{g,cr}$ | Critical gas velocity |
| $v$ | velocity term |
| $V$ | volume |
| $y^+$ | distance to wall non-dimensionalized with inner variables |
| $t$ | time |
| $t$ | tangential coefficient |
| $t_{br}$ | fragmentaion time |
| $T$ | time scale |
| $V$ | volume |
| $Vol$ | volume |
| $Y_k$ | dissipation term for turbulent kinetic energy |
| $Z$ | Z-factor |

## Greek Symbols

| | |
|---|---|
| $\alpha$ | angle of bend |
| $\alpha$ | volume fraction |
| $\chi$ | distance between droplets |
| $\delta_f$ | film height |
| $\delta_{ij}$ | Kronecker delta in index notation |
| $\varepsilon$ | dissipation |
| $\eta$ | separation efficiency |
| $\eta$ | length scale |
| $\rho$ | density |
| $\mu$ | dynamic viscosity |
| $\mu_t$ | turbulent dynamic viscosity |
| $\omega$ | dissipation |
| $\nu$ | kinematic viscosity |
| $\nu_t$ | turbulent kinematic viscosity |
| $\sigma$ | surface tension coefficient |
| $\sigma$ | turbulent Prandtl number |
| $\tau$ | time scale |
| $\tau$ | viscous shear stress |
| $\tau_t$ | turbulent shear stress |
| $\tau_{SGS}$ | SGS shear stress |

| | |
|---|---|
| $\sigma$ | surface tension coefficient |
| $\zeta$ | flow coefficient |

## Non-dimensional numbers

| | |
|---|---|
| $Fr$ | Froude number |
| $Oh$ | Ohnesorge number |
| $Re$ | Reynolds number |
| $We$ | Weber number |

## Abbreviations

| | |
|---|---|
| BL | Boundary Layer |
| CFD | Computational Fluid dynamics |
| CFL | Courant Friedrichs Lewy number |
| CPU | Central Processing Units |
| DES | Detached Eddy Simulation |
| DNS | Direct Numerical Simulation |
| DPM | Discrete Phase Modeling |
| FEA | Finite Element Analysis |
| FEM | Finite Element Method |
| FVM | Finite Volume Method |
| geo2 | geometry 2 |
| HP | High Pressure |
| k-$\epsilon$ | k-$\epsilon$ turbulence model |
| LCO | Liquid Carry Over |
| LES | Large-Eddy Simulation |
| LP | Low Pressure |
| MC | Measuring Cup |
| MSm3 | Thousand Standard cubic metre |
| NGL | Natural Gas Liquid |
| NS | Navier-Stokes |
| RAM | Random Access Memory |
| RANS | Reynold Averaged Navier-Stokes |
| ref | reference geometry |
| URANS | Unsteady Reynold Averaged Navier-Stokes |

| | |
|---|---|
| SAS | Scale Adaptive Simulation |
| SCF | Standard cubic feet |
| SGS | Sub Grid Scale |
| SST k-$\omega$ | Shear-Stress Transport k-$\omega$ trubulence model |
| USgal | US gallon |
| UW | Up-Wind |
| VG | Gas Vessel |
| VOF | Volume of Fluid |
| VX | Liquid Vessel |

# Chapter 1

# Introduction

The petroleum sector on the Norwegian continental shelf produced a total of 238 millions $Sm^3$ marketable oil equivalents in 2007, where 89 billions where $Sm^3$ natural gas. Oljedirektoratet (2008) reported that the oil and gas industry covered 38% of the state revenues and 48% of Norway's total export value in 2007. The gas share of the petroleum sector is expected to increase from 38 % in 2007 to 46% in 2012. The growth in the gas production is mainly because of the decrease in oil field discovering, and the focus on more environmental friendly fuels. The decrease in new petroleum fields has driven the oil and gas companies towards fields that had no interest for 20 years ago. These fields are often small and on deep water. Small fields have small margins for profit and rely more on fully functioning process equipment, a malfunctioning separator can lead to breakdown of downstream equipment, which are crucial to the fields economy (Brigadeau, 2007). The efficiency of the separator is often the factor that constraints the production capacity. In most cases the design of the separator is based on knowledge from experiments carried out on air/water, low pressure systems. Efficiencies decrease with increasing pressure and load, so enhancements in separation efficiency will gain production capacity (Austrheim, 2006). Overloading the separators capacity often cause troublesome conditions for downstream equipment, it can damage compressors, measuring equipment, decrease life time due to corrosion or lead to hydrate formation in pipelines. A malfunctioning scrubber can in the worst cases cause platform shut down, which are all followed by huge financial losses due to reduced income. The separation technology development, lies mainly on the knowledge in fluid physics at extreme operating condition. The understanding of turbulence and two phase flow are fundamental when designing high efficiency scrubbers. And of especially importance how to simulate these phenomena.

## 1.1 Natural gas processing

Before the gas can be transported to the gas market, it goes through several process steps, listed in chronological order:

**Removal of oil, condensate and solids.** To obtain merchantable quality, the oil and condensate are removed from the gas. This can be achieved in a separation vessel, by reducing the pressure so that the heavy hydrocarbons condense out. Solids are typically sand, and are a difficult problem subsea, the separation is not difficult but the problem is where to put it afterwards.

**Water removal.** Water is the main obstacle for transporting hydrocarbons in pipelines, since present water gives a potential of hydrate formation. Under pipe transport the hydrocarbons are cooled by the surrounding water temperature and the pressure decreases due to the pressure loss. Hydrates form when water condenses from the natural gas and are presented at pressure and temperature below equilibrium line. Antifreeze chemicals are usually injected to lower the hydrate formation temperature. Typically 50 vol% of antifreeze, relative to water, has to be injected, which is very expensive. Future concept is to avoid this expense by separating water at the well head.

**Gas cleaning.** Natural gas liquids, NGLs, are removed to get the correct dew point on the gas, by a batch of pressure reduction the NGLs can be removed.

**Gas sweetening.** Usually hydrogen sulfide, $H_2S$, and carbon dioxide, $CO_2$. Both are hazardous substances and very corrosive when liquid water is present. They have no contribution on the heating value of the gas. $CO_2$ is not as bad as $H_2S$, but most treating processes that remove the latter also remove $CO_2$. Sweetening is done by an absorption technique by the use of an amine solution.

## 1.2 Separator and scrubber vessels

Separators are divided into two divisions, separator and scrubber vessels. The former, handling small gas to oil ratios, GOR, usually horizontally oriented and the latter vertically with large GOR values. They both consist of many similar internals, figure 1.1 shows an example of both vessel types.

The separator to the left in figure 1.1 is a three phase separator handling gas, water and oil. The three phases enters through the inlet pipe and flows through four inlet cyclones. The separation of the phases starts in the inlet cyclones. The inlet internal is supposed to separate and evenly distribute the three phases. The perforated plates prevent foaming, reduce the emulsion layer and calm the flow. Demisting cyclones are located at the outlet of both vessels.

The scrubber vessel in figure 1.1 has a Inlet Vane Distributor, IVD, that evenly distributes and separates the flow after entering the scrubber. The mist flow leaving the IVD enters a mesh pad which work as a demister and/or a coalescer. The separation made by the IVD and the mesh pad is often referred to as the bulk separation. Axial cyclones are placed above the mesh pad. Equipment designed for one phase flow, e.g. compressors, usually have a scrubber vessel installed in front, just to avoid the presence of multiphase flow.

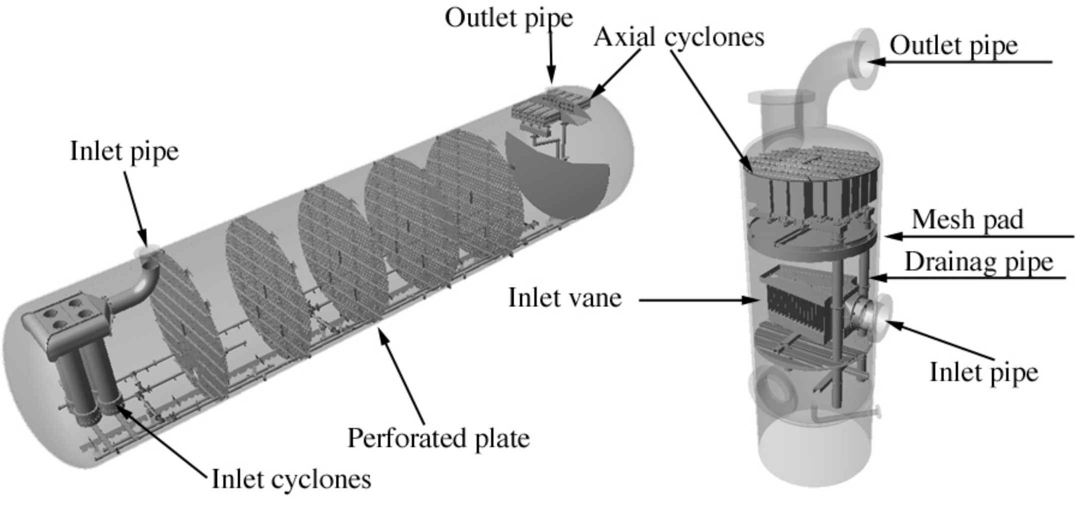

Figure 1.1: Three phase separator vessel (left) and a scrubber vessel (right).

The outlet internals in both vessel types are often referred to as demisting equipment, since they operate with a mist flow. Two types of demisters are traditionally used, cyclones or vane packs. Cyclones are not studied here, but are throughly investigated by

Verlaan (1991) , Swanborn (1988) and Austrheim (2006). Different internals are explained by Carlson and Talseth (2008).

NORSOK (2001) states the following " A typical general specification of maximum liquid entrainment has historically been 13 litre/MSm3 (0.1 USgallon/Million SCF)". To illustrate this in a demisting perspective the following example is included: according to Natco (2009) a typical liquid load for a scrubber vessel is 0.5 % liquid volume fraction. Typically 90% gets separated upstream the demister, here assumed independent of pressure. Meaning that 10 % liquid passes on to the demisting internals. The liquid load for the scrubber is assumed constant. NORSOK (2001) then specifies the lower limit of the demister efficiency: The lower limit for the demister decreases as the pressure increases, while the difficulties regarding the separation increases, discussed in the next section.

Table 1.1: Example of demister section efficiency to achieve 0.1 USgallon/MMSCF

| P [barg] | T [C$^o$] | $\rho_{NG}$ | $\alpha_{inlet,vane}$ [%] | $\eta_{\text{demister limit}}$ | Carry-over [USgal/MMSCF] |
|---|---|---|---|---|---|
| 1 | 15 | 0.76 | 0.005 | 99.9976 | 0.0997 |
| 20 | 15 | 16.65 | 0.005 | 99.9480 | 0.0986 |
| 40 | 15 | 34.30 | 0.005 | 99.9000 | 0.0921 |
| 80 | 15 | 75.12 | 0.005 | 99.7700 | 0.0967 |

## 1.3 Vane pack demisters

Vane packs consist of many profiled plates mounted upon each other, figure 1.2. The design varies a lot for the different manufacturers, from simple bent plates to complex geometries with drainage slits. A vane pack can be horizontally or vertically oriented, depending on available space, use and design. In scrubber vessels they are typically vertically oriented, and in separator vessels horizontally oriented.

The droplet laden gas enters and follows the bended channel. The droplets have a larger inertia than the gas and will hit the wall. The droplets will form a film on the wall. This film can be drained away by different techniques. For a vertically oriented vane pack without drainage slits, the film is drained away counter current to the gas flow, by gravity.

For a horizontally oriented vane pack, the liquid is drained away perpendicular to the gas flow, also by gravity. The plates can be designed with a drainage system that will lead the film into drainage chambers where it is drained away by gravitational forces, as in figure 1.2. Different designs of drainage system for vane packs are reported by Verlaan (1991)

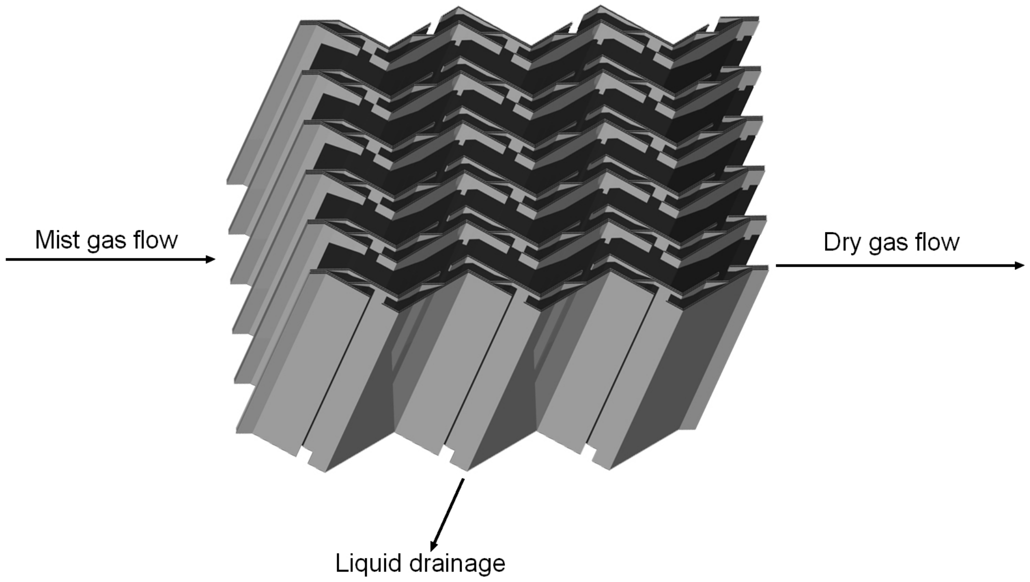

Figure 1.2: Horizontal oriented vane pack with drainage chambers. Gravitational force in or out of the paper.

The maximum gas capacity is limited by different types of phenomena depending on the vane design. In the case of counter current drainage it is limited by flooding. Flooding occurs when the drag force from the gas on the film interface is larger than the gravitational drainage force. If the force balance is equal to zero, flooding point, the liquid film thickness will build up, and either cause high re-entrainment or plug the channel. If the gas throughput is much more than the maximum capacity the film will flow along with the gas and out of the separator. Liquid that flows through the outlet can be fatal to downstream equipment. Feind (1960) developed an empirical correlation for the flooding point.

Vane packs designed with a drainage chambers have a larger gas capacity than those without, because the liquid is protected from the gas shear by the drainage chambers. The maximum gas capacity is limited due to the onset of re-entrainment from the film.

Re- entrainment is when droplets get shredded of the wavy surface of the film and back into the gas stream (Brigadeau, 2007).

The onset of re-entrainment is not only dependent on the gas shear, but also on the operating pressure. When the pressure increases the surface tension decreases and the gas/liquid density ratio decreases. The critical gas speed that gives an unstable film is $U_{g,cr} = \sqrt{\frac{2(\rho_l \sigma g)^{0.5}}{\rho_g}}$, Verlaan (1991). So if the surface tension and $\frac{\rho_l}{\rho_g}$ decrease the onset of unstable film and re-entrainment occurs at a lower gas loading. The average droplet size will also decrease with decreasing surface tension. These features emphasis some of the difficulties in high pressure separation.

## 1.4 Scope of this thesis

The aim of this work is to gain knowledge on the vane pack demisters investigated and proposed by Carlson and Talseth (2008). The strategy to enhance the understanding of phenomena regarding separation of liquids from gases was:

- Study turbulence physics and transient turbulence models.
- Study fundamentals of dispersed two-phase dynamics and suitable simulation techniques.
- Couple the theory of two-phase physics with turbulent one-phase simulations.
- Include a dispersed phase by simulating droplets with a transient discrete phase model.
- Experimentally test different vane pack demisters at high pressure with $SF_6$ as gas and Exxol D60 as liquid.

# Chapter 2

# Theoretical basis and numerical methods

The structure of theoretical basis and numerical methods is:

- Fluid flow behavior
- Governing equations
- Numerical modeling
- Turbulence models
- Multi phase flow behavior
- Discrete phase modeling

## 2.1 Dimensionless numbers

**The Reynolds number**: This number gives the ratio between the inertia forces and the viscous forces. For high values the flow is turbulent, low values imply laminar flow and for $Re < 1$ a Stokes flow

$$Re = \frac{\rho u L}{\mu} \ , \tag{2.1}$$

where u and L are characteristic velocity and length scales of the flow.

**Weber number**: The Weber Number is the ratio between the inertial force and the surface tension force, and is defined as

$$We = \frac{\rho u^2 L}{\sigma} \ , \tag{2.2}$$

where L is the characteristic length scale, typically the droplet diameter. The Weber number can be used to describe the behavior of droplets and films.

## 2.2 Fluid flow behavior

The characteristics of a fluid flow is divided into three regimes, laminar, turbulent or transition. These regimes are normally described by the Reynolds number, $Re$, see equation 2.1. The $Re$ number gives a measure of the relative importance between the inertia forces and the viscous forces. At some value of $Re$ a transition occurs, where the flow behavior changes dramatically from steady to chaotic, this is the critical Reynolds number, $Re_{crit}$. Smoke from a cigarette is a good example of all regimes. First the smoke flows with no disruption, until it transforms into a mixing chaotic flow.

For values below $Re_{crit}$ the flow is steady, calm and streamlined, which is the laminar regime. Laminar flows have no typical separation of the time and length scales, meaning that the viscous forces are of such magnitude that small perturbations will be damped by viscous dissipation. This flow behavior can be found where high viscosity fluids are used, for example in lubricating systems.

Values above $Re_{crit}$ is the turbulent regime. Meaning that inertia forces are dominating and perturbations are no longer fully damped. The flow is of random and chaotic fashion, involving stretching of vortex filaments, both internally self-stretchning eddies, and externally stretching due to the mean flow. The time and length scale for the eddies, range from large to extremely small. The ratio between the small and the large scales can be estimated by

$$\text{Length scale: } \frac{\eta}{l} \approx Re_l^{-\frac{3}{4}} \ , \tag{2.3}$$

$$\text{Time scale: } \frac{\tau}{T} \approx Re_l^{-\frac{1}{2}} \ , \tag{2.4}$$

$$\text{Velocity scale: } \frac{\upsilon}{v} \approx Re_l^{-\frac{1}{4}} \ . \tag{2.5}$$

Where the $\eta$, $\tau$ and $v$ are the small scales and $l$, $T$, $v$ are the large scales. The smallest eddies are where the inertia and the viscous forces are equal and are named the Kolmogorov microscales (Versteeg, 2007). The ratio between the small and large eddies are of several orders of magnitude. This phenomena is called scale separation and is the main challenge for numerical modeling of turbulence. Most flows occurring in nature and in industrial applications are turbulent, for example: motion of clouds, rivers, flow in a turbine, boundary layer development over a car, scrubber equipment in the petroleum industry (Tennekes and Lumley, c1972).

## 2.3 Governing equations

Fluid flow motion is described by the continuity equation and the Navier-Stokes, NS, equations. They are today well accepted as the solution for macroscopic flow phenomena in fluid mechanics

$$\frac{\partial}{\partial x_j}(\rho u_j) = 0 \ , \tag{2.6}$$

$$\rho\frac{\partial}{\partial t}(u_i) + \rho\frac{\partial}{\partial x_j}(u_i u_j) = -\frac{\partial p}{\partial x_i} + \mu\frac{\partial}{\partial x_j}\left(\frac{\partial u_i}{\partial x_j} + \frac{\partial u_j}{\partial x_i}\right) + \rho f_i \ . \tag{2.7}$$

The fluid is assumed incompressible with fluid stresses divided into a viscous term and a pressure term. The second term on the left hand side is the convection term, this term makes the NS equations non-linear and impossible to solve directly for most geometries. Another problem is that the velocity and pressure are coupled, and that very often a equation for the pressure is missing.

## 2.4 Numerical modeling

There are many discretization methods for solving the governing equations, where the finite element method, FEM, and the finite volume method, FVM, are the most common ones. The latter is used by Fluent and is therefore shortly described. The meshed domain is divided in finite control volumes around the nodes. The discrete equations are preserving conservation of all variables in an infinitesimal control volume, and FVM is doing the same over a finite volume. Divergence terms in the discrete partial differential equations, PDE, are transformed into surface integrals, through the Gauss theorem, to represent fluxes in and out of the surface of the control volume. If one considers the Navier Stokes equation in vector form:

$$\frac{\partial \vec{u}}{\partial t} + \vec{\nabla} \cdot (\rho \vec{u}\vec{u}) = -\vec{\nabla}(p) + \vec{\nabla} \cdot (\mu \nabla(u)) \ . \tag{2.8}$$

Integrating the equation over a control volume, $V_i$.

$$\int_{V_i} \frac{\partial \vec{u}}{\partial t} dV_i + \int_{V_i} \vec{\nabla} \cdot (\rho \vec{u}\vec{u}) dV_i + \int_{V_i} \vec{\nabla}(p) dV_i - \int_{V_i} \vec{\nabla}(\mu \nabla(u)) dV_i = 0 \ . \tag{2.9}$$

Fluid velocity is well known connected to the pressure gradient, the Semi-Implicit Method for Pressure-Linked Equations, SIMPLE, solution algorithm is used for the pressure-velocity coupling, description can be found in (Versteeg, 2007).

## 2.5 Turbulence models

As mentioned turbulence gives arise to the phenomena of scale separation. A numerical setup that resolves all the turbulent scales is called a direct numerical simulation, DNS. No modeling is required in a DNS. The grid size necessary for a DNS is proportional to $Re^{\frac{9}{4}}$, which constrains it to very simple geometries. A different approach is to Reynolds decompose the properties in the governing equations, into mean and fluctuating values, and then time average them over a much longer period than the time scale of the largest eddies. This approach gives the Reynolds Averaged Navier Stokes, RANS, models. Solutions of RANS give the mean flow properties. For a mist flow where eddies and droplet physics are of interest, a transient model that resolves the unsteady eddies is preferable. Standard unsteady RANS models are available, they solve the mean stream instability and are therefore only mildly unstable. Large Eddy Simulations, LES, lies between DNS and URANS, figure 2.1 illustrate the scale resolution of the different modeling approaches. The $\Delta_{LES}$ is commonly dependent on the grid spacing. In recent years different versions of LES and RANS have been made, like Detached Eddy Simulations, DES, and Scale-Adaptive Simulations, SAS. In the following four different models will be described, and in the next chapter their performance are tested.

### 2.5.1 The Shear-Stress Transport $k$-$\omega$ model

The Shear-Stress Transport, SST, $k$-$\omega$ is a RANS model that uses the Reynolds Averaged governing equation, where the velocity, $u$, is decomposed into a mean, $U$, and a fluctuating,

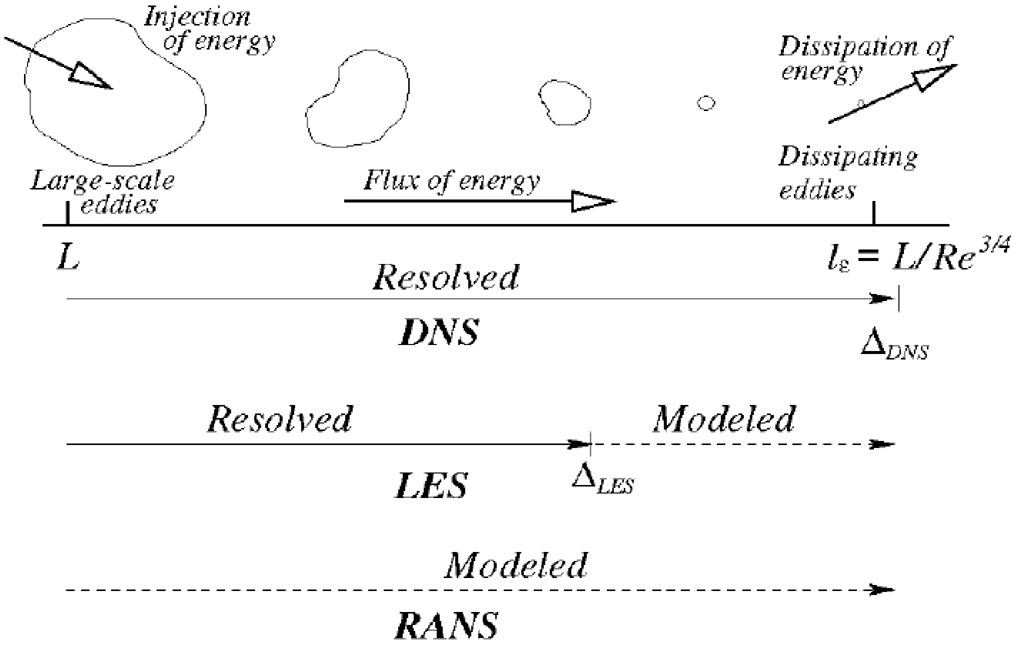

Figure 2.1: Illustration of the energy scale resolved for the different turbulence approaches

$u'$, velocity, and then averaged in time. The RANS equations are

$$\frac{\partial}{\partial t}(\rho U_i) + \frac{\partial}{\partial x_j}(\rho(U_iU_j + \overline{u_i'u_j'}) = -\frac{\partial \overline{p}}{\partial x_i} + \frac{\partial \overline{\tau}}{\partial x_j} + \rho \overline{f_i}\ . \tag{2.10}$$

The fluctuations contribute through the second term in the convection term and are modeled by the Boussinesq eddy viscosity hypothesis, $-\overline{u_i'u_j'} = \mu_t(\frac{\partial U_i}{\partial x_j} + \frac{\partial U_j}{\partial x_i}) + \frac{2}{3}(\rho k + \mu_t\frac{\partial U_l}{\partial x_l})$. This eddy-viscosity RANS model was introduced by Menter (1994). Menter (1994) mixed together two models, the $k$-$\varepsilon$ and the $k$-$\omega$ model, by transforming the $\varepsilon$ equation into $\omega$, then adding a blending that allows it to slide from one model to the other. Both base models have drawbacks and advantages. The $k$-$\varepsilon$ tends to become too diffuse in the sublayer and the log layer. On the other hand it is very well defined in the boundary layer edge and in the free stream, it is free stream insensitive. The $k$-$\omega$ is accurate in the sublayer and in the log layer but, it is sensitive to the free stream. The SST model was developed with the purpose of combining the advantages of these two models. The SST $k$-$\omega$ ensures a proper relation between turbulent stresses and the turbulent kinetic energy, $k$, which allows it to accurately and robustly predict flows with flow separation. This model uses the same formulation for $k$ in the boundary layer as for the $k$-$\varepsilon$ with enhanced wall treatment, described in (Ansys, 2009). The governing equations for the SST $k - \omega$ are

$$\frac{\partial k}{\partial t} + \frac{\partial U_i k}{\partial x_i} = \frac{\partial}{\partial x_j}\left[\left(\nu + \frac{\nu_t}{\sigma_k}\right)\frac{\partial k}{\partial x_j}\right] + P_k - \beta^* k\omega\ , \tag{2.11}$$

$$\frac{\partial \omega}{\partial t} + \frac{\partial U_i \omega}{\partial x_i} = \frac{\partial}{\partial x_j}\left[\left(\nu + \frac{\nu_t}{\sigma_\omega}\right)\frac{\partial \omega}{\partial x_j}\right] + P_\omega - \beta\omega^2 + 2(1 - F_1)\sigma_{\omega 2}\frac{1}{\omega}\frac{\partial k}{\partial x_j}\frac{\partial \omega}{\partial x_j}\ . \tag{2.12}$$

The first equation is the transport equation for the turbulent kinetic energy. The latter is the equation for the specific dissipation rate $\omega$ where the $2(1-F_1)\sigma_{\omega 2}\frac{1}{\omega}\frac{\partial k}{\partial x_j}\frac{\partial \omega}{\partial x_j}$ term allows the model to slide between the $\omega$ behavior near a wall and the $\varepsilon$ behavior in the free stream. A full description of all the terms in this model can be found in Ansys (2009). This subsection is based on the discussions and lectures at the Turbulence Workshop by Ansys (2008). A drawback with this model is that it has a isotropic eddy viscosity assumption, so that the eddy viscosity is equal in every direction. The only factor that indicates some direction is the derivates of the mean flow, which constraints the turbulence down to always be in the same directions as the mean flow.

### 2.5.2 Scale-Adaptive Simulation theory

A Scale-Adaptive Simualtion, SAS, is an improved URANS formulation that includes an additional length scale to the calculation. In the following the SST k-$\omega$ based SAS is introduced. The scale adaptive behavior is achieved by adding a term, $P_{SAS}$ to the $\omega$ equation 2.12. The $P_{SAS}$ term is

$$P_{SAS} = F_{SAS} \max\left( \tilde{\zeta}_2 \kappa S^2 \frac{L}{L_{vK}} - \frac{2k}{\sigma_\Phi} \max\left( \frac{1}{\omega^2}\frac{\partial \omega}{\partial x_j}\frac{\partial \omega}{\partial x_j}, \frac{1}{k^2}\frac{\partial k}{\partial x_j}\frac{\partial k}{\partial x_j} \right), 0 \right) . \tag{2.13}$$

The standard $k$-$\omega$ SST model applies when $P_{SAS}$ is equal to zero, further referred to as the RANS-regime. The scale adapting behavior is active when $P_{SAS}$ is larger than zero, SAS-regime. In the coming this dynamic behavior will be described, but first the $\omega$-equations contribution to the fluid flow is explained. Recalling the RANS equation for an eddy viscosity turbulence model, the contribution of the $\overline{u_i' u_i'}$-stresses are modeled by added viscous dissipation through the $\mu_t$ term. The calculation of the turbulent viscosity in the $k$-$\omega$ SST model is

$$\mu_t = \frac{\rho k}{\omega} \frac{1}{\max(\frac{1}{\alpha}, \frac{SF_2}{\alpha\omega})} . \tag{2.14}$$

An increase in $\omega$ will lead to a reduction of $\mu_t$, and thereby less damping of the flow. The interesting term is the von Karman length scale,

$$L_{vK} = \kappa \left| \frac{\partial U/\partial y}{\partial^2 U/\partial y^2} \right| . \tag{2.15}$$

The second derivative of the velocity is supposed to go to zero when approaching a wall, giving a small $L_{vK}$ and then a higher $\omega$. So when turbulence is resolved this length scale is supposed to be much smaller than traditionally length scales. The $\frac{L}{L_{vK}}$ term becomes large when unsteady velocities are resolved, leading to less damping of perturbations, by increasing the $\omega$ and thereby reducing $\mu_t$ (F.Menter and Y.Egorov, 2006). Davidson (2006) investigated the standard SST model against the SST-SAS and concluded that the $\frac{L}{L_{vK}}$ term make the SST-SAS capable of resolving much more fluctuations than the standard SST. Standard turbulence models provide a length scale that is independent of local flow topology, usually proportional to the thickness of the shear layer. As reported by Ansys (2008),Lec (2008), F.Menter and Y.Egorov (2006) and Davidson (2006), this "rigid" definition of the length scale makes them incapable of finding instabilities and make them very diffusive. The effect of $P_{SAS}$ on the SST $k - \omega$ is investigated in chapter 3.1. This SST based SAS is further called SAS.

### 2.5.3 Detached-Eddy Simulations

First proposed in 1997 and used in 1999. The development of this technique is focused on high-Reynolds number, wall bounded flows with massively separated behavior. The idea behind DES as originally proposed is to employ the good performance of RANS in the boundary layer and the LES technique outside the boundary layer. A switch function based on the ratio between the turbulent length-scale and the grid size, control the different numerical treatment of the flow, "RANS mode" or "LES mode" Ansys (2008). In principal this only means that one change the dissipation term of the standard SST $k-\omega$ model. The SST based DES is presented here. The RANS model calculates the turbulent length scale, $L_t$, and when it is larger than the local mesh size it switches to "LES mode". The switch function can be of the form

$$\widetilde{L_t} = min(L_t; C_{DES}\Delta) \ , \tag{2.16}$$

where $\Delta = max(\Delta_x, \Delta_y, \Delta_z)$. $C_{DES}$ is a constant that can be estimated by investigating the relaxation time for turbulence. One problem for DES formulations might arise if the user specifies the grid incorrectly, and switches between the models appear in the boundary layer, as illustrated in figure 2.2. Another problem occurs if the separated regions are not of massive order, then the switch may not happen and a RANS solution appears in the hole domain. Software developers try to reduce this shortcoming by adding blending functions, so that RANS mode is forced to the wall region. A SST based DES was tested in the preliminary calculations, where this was the problem. All the equations will not be presented in this section, please refer to Ansys (2009). As explained the

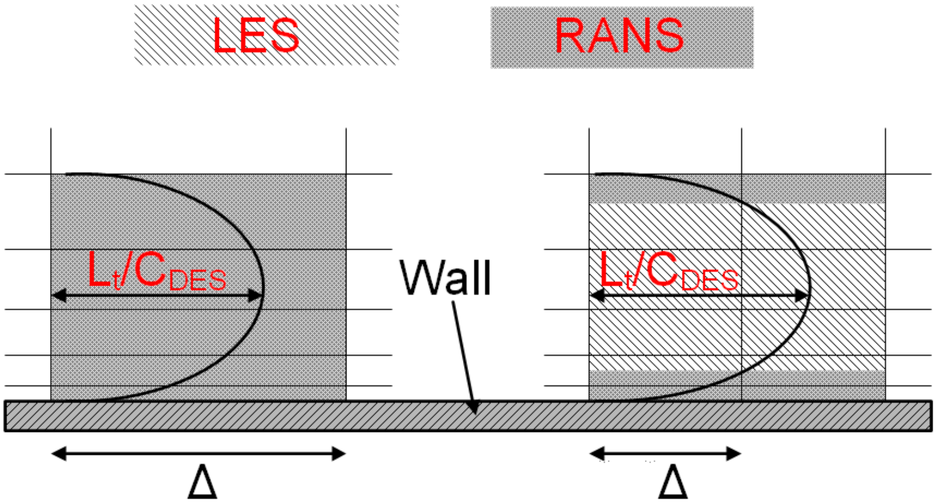

Figure 2.2: Illustration of problems with the switch in a DES simulation, figure to the left is correct and to the right is incorrect.

performance of the switch function together with the grid is crucial for the result. The dissipation term of the turbulent kinetic energy is

$$Y_k = \rho\beta^* k\omega F_{DES} \tag{2.17}$$

and the switch function is:

$$F_{DES} = max(\frac{L_t}{C_{des}\Delta}(1 - F_{SST}), 1) \tag{2.18}$$

Where $L_t = \frac{\sqrt{k}}{\beta^*\omega}$. The approach is very similar to the SAS method, except that here the switch is indirectly set by the user through the mesh size, further in this thesis this SST based DES is called DES.

### 2.5.4 Large Eddy Simulation, LES

Large eddies are responsible for mostly of the transport of momentum and energy, they are anisotropic and strongly dependent on boundary conditions, which make their modeling difficult. Small eddies tend to be more universal, geometry independent and homogeneous, thus a model for these scales require less adjustments than a model for the large scales. This is the basic idea behind the development of this modeling technique. Based on the resolving of some scales, LES is an intermediate approach between RANS and DNS. The ability to differ between when to solve large scales and when to model small scales, is achieved through a filtering operation. The filtered variable used is

$$\widetilde{\phi}(\mathbf{x}) = \int_D \phi(\mathbf{x}')G(\mathbf{x},\mathbf{x}')dx' \ , \tag{2.19}$$

where D is the fluid domain and G is the filter function. The filter function used in Fluent 12 is

$$G(\mathbf{x},\mathbf{x}') = \begin{cases} \frac{1}{V}, & x' \in \nu \\ 0, & x' \text{ otherwise} \ . \end{cases} \tag{2.20}$$

This filter should be in the inertia range of the energy spectrum, and very often the user is incapable of knowing where this is. If the filtering operation is applied to the governing equations, one gets the governing equations for LES. For incompressible flow of a Newtonian fluid they are

$$\frac{\partial \widetilde{u_i}}{\partial x_i} = 0 \ , \tag{2.21}$$

$$\frac{\partial \widetilde{u_i}}{\partial t} + \frac{\partial}{\partial x_j}(\widetilde{u_i}\widetilde{u_j}) = -\frac{1}{\rho}\frac{\partial \widetilde{p}}{\partial x_i} + \nu\frac{\partial^2 \widetilde{u_i}}{\partial x_j \partial x_j} - \frac{\partial \tau_{ij}}{\partial x_j} \ . \tag{2.22}$$

A new term is introduced, the subgrid-scale, SGS, which is defined as

$$\tau_{ij} \equiv \widetilde{u_i u_j} - \widetilde{u}_i \widetilde{u}_j = L_{ij} + C_{ij} + R_{ij} \ . \tag{2.23}$$

The effects of the small scales appears through this term. This definition is usually abandoned, described by Piomelli (1999). The common for most models is that they employ the Boussinesq hypothesis by assuming that the SGS stresses are proportional to the filtered strain rate, $\widetilde{S}_{ij} = \frac{1}{2}(\frac{\partial \widetilde{u}_i}{\partial x_j} + \frac{\partial \widetilde{u}_j}{\partial x_i})$, of the large scales:

$$\tau_{ij} - \frac{\delta_{ij}}{3}\tau_{kk} = -2\nu_T \widetilde{S}_{ij} \ . \tag{2.24}$$

The isotropic part of the SGS stresses, $\tau_{kk}$, is not modeled, but added to the filtered static pressure term.

### The subgrid-scale stresses and their modeling

The subgrid-scale stresses in a LES are unsolved and can be modeled with different models. The success of a LES lies on the grid spacing and on how accurate the SGS stresses are modeled. The smallest scales represent the dissipation, so the SGS model represents the sink term in the simulation. This emphasizes the importance of an accurate SGS model. If this sink term is too big the solution will become too diffusive. The model developed by Smagorinsky (1963) is the most used model today. The Smagorinsky model is, as most models are, based on the assumption of total equilibrium between the small scales, meaning that they dissipate entirely and instantaneously all the energy delivered by the larger scales. The Smagorinsky model is

$$\nu_T = C\Delta^2 |\widetilde{S}_{ij}| \widetilde{S}_{ij} \ , \tag{2.25}$$

with $C_S = \sqrt{C}$ and $\Delta = (cellvolume)^{\frac{1}{3}}$. The proportionality constant has the same value if it is in the mean flow or close to a wall, so this model is incapable of reducing the length scale close to a wall. More sophisticated models have some kind of dampning function close to solid boundaries, like the Wall-Adapting Local Eddy- Viscosity, WALE, model developed by Nicoud and Ducros (1999). The wall damping in the WALE is accounted for without using an explicit damping function. The turbulent viscosity is approximated as

$$\mu_T = L_s^2 \frac{(S_{ij}^d S_{ij}^d)^{\frac{3}{2}}}{(\widetilde{S}_{ij}\widetilde{S}_{ij})^{\frac{5}{2}} + (S_{ij}^d S_{ij}^d)^{\frac{5}{4}}} \ , \tag{2.26}$$

where the mixing length, $L_s$ and $S_{ij}^d$ are defined as

$$L_s = min(\kappa d, C_\omega V^{\frac{1}{3}}) \tag{2.27}$$

$$S_{ij}^d = \frac{1}{2}(\tilde{g}_{ij}^2 + \tilde{g}_{ji}^2 - \frac{1}{3}\delta_{ij}\tilde{g}_{kk}^2) \ , \tag{2.28}$$

with $\tilde{g}_{ij} = \frac{\partial \tilde{u}_i}{\partial x_j}$. Nicoud and Ducros (1999) developed WALE for the purpose of reproducing the proper scaling at the wall, $y^3$, and to be able to handle structured and unstructured grids.

The use of LES in boundary layer, BL, flows at high Reynolds numbers is almost as expensive as a DNS and therefore very time consuming for industrial simulations. On the other hand, turbulent structures can be resolved in massively separated regions, where the large turbulent scales are of the same dimensions as the geometrical structure generating them, this structures are less time consuming compared to the small BL structures. During the last decade a lot of focus has been on trying to add terms to the standard RANS models, so that the can achieve LES like behavior. Traditionally this is done by changing the turbulent viscosity, as done in the DES and the SAS model.

## 2.6 Multi phase flow behavior

Turbulence is one difficulty regarding CFD simulations of a gas/liquid separator. The available transient turbulence models in Fluent has been described in the previous section. Introducing another fluid phase makes it even more complex and adds more uncertainties.

Objectives of this section are:

- Give a short description of multiphase flow and the different modeling approaches.
- Explain the mechanisms and theory regarding fragmentation and coalescence.
- Describe the transient discrete phase modeling approach in Fluent, including fragmentation, coalescence and wall-film.

Multiphase flow plays an important role in nature, and is defined as a fluid flow consisting of more than one phase or component. Ansys (2009) defines a phase as an "indentifiable class of material that has a particular inertial to and interaction with the flow and the potential field in which it is immersed". The subject multiphase flow encounters a vast field of different challenges, e.g. microscopic effects in a macroscopic view, different time and length scales involved, surface tension between phases, different interactions between the phases or/and particles.

Multiphase flow can be categorized into four flow regimes:

- Gas - liquid
- Liquid-liquid
- Liquid/Gas - Solid
- Three phase flow

Since the two-phase flow inside the vane pack are droplet laden, this multiphase study focuses mainly on two-phase droplet dynamic.

A droplet in a surrounding fluid introduces several phenomena. The first obstacle regarding modeling of a droplet, is when the surrounding fluid is moving, the drag force from the continuum append forces on the interface of the droplet, which imposes it to move. If the droplet is large and the continuum generates a velocity gradient through the drop, it might change shape or if the gradient is big, it might split into several droplets, called fragmentation. For a mist flow, where there are several droplets, a droplet might collide with another droplet. The outcomes of such a collision are several, they might collide and become a bigger droplet, called coalescence, or they might bounce away from each other. Or if the momentum of the impact is big enough they might fragment into several smaller droplets. If the multiphase involves a solid surface the collision might also happen there. Introducing a second phase gives as mentioned several additional physics, which are even complex to model correctly for a laminar multiphase flow. There are two phases in a vane pack, where the secondary phase is present both as a film and as droplets. There are two major approaches for numerical calculation of multiphase flows, Euler-Lagrange or the Euler - Euler approach. Those will in the following be described.

The Euler - Langrange description tracks the position and velocity of individual particles, based on Newton's laws. The Euler - Lagrange description is less computational expensive than the Euler -Euler description, and is useful for describing sprays, dispersed particles and droplets. The drawback of the Euler - Lagrange approach is the lack of capability to handle large number of particles, and segregated flows. A challenge is how to describe the interaction among the particles themselves and between the particles and the continuum. Fluent has a Descrete Phase Model, DPM, that optional includes a wall - film model, two-way coupling and particle interactions. The volume fraction of the discrete phase is limited to be less than 10-12%.

In contrast to the Euler - Langrange description that follows individual particles, the Euler - Euler description defines a flow domain and describes the passage of fluid through the domain. The Euler - Euler approach treats the different phases as interpenetrating continua. This approach treats a large number of multiphase flows and handles several phases with optional volume fraction. The NS equations describe the flow in each phase and the challenge is to formulate closure models for the interaction between the different phases. Fluent has three available models with the Euler- Euler approach, Eulerian model, Mixture model and Volume of fluid, VOF, model. Each model treats a given section of multiphase flows. The VOF model handles segregated flows well, while the Eulerian model is intended for dispersed flow. At the present time there is no available model in an Eulerian reference frame that combines a segrated flow with a dispersed phase in Fluent.

The vane packs that are modeled in this thesis will have a volume fraction, $\alpha_l$, of the dispersed phase below 1%. The dispersed droplets will encounter the wall wich creates a liquid film. Simulations in Fluent of both the dispersed droplets and a liquid film on the wall are at the present situation only available with the Euler - Lagrange approach. The two phase dynamics in a vane pack are liquid film behavior, droplet- fragmentation and coalescence. Film behavior involves waves on the surface and re-entrainment. Due to this the present physics regarding fragmentation and coalescense is studied in the following section. First some definitions describing a dispersed flow are presented.

The volume fraction, $\alpha_l$, describes the ratio between the volume occupied by phase $d$, and the total volume occupied by the flow mixture, $\sum_{d=1}^{i} Vol_d$.

$$\alpha_d = \frac{Vol_d}{\sum_{d=1}^{i} Vol_d} \ , \tag{2.29}$$

where $\sum_{d=1}^{i} Vol_d$ is the total volume for $i$ phases. The droplet number density, $n_d$, is defined as the volume-averaged number of discrete droplets of the fluid d, e.g. droplets, per unit flow volume. For a locally mono-dispersed droplet field, the droplet number density is defined as:

$$n_d = \frac{6}{\pi}\frac{\alpha_d}{D_d^3} , \tag{2.30}$$

where $D_d$ is the diameter of the droplet.

### 2.6.1 Droplet physics

This section gives a short description of the theory around fragmentation and coalescence physics of droplets in a continuum gas phase, in a macro perspective.

Dispersed droplets in a continuous phase can as mentioned interact with each other, coalesce or get fragmented by acceleration or turbulence. The continuous gas phase is denoted, $()_g$, and the dispersed droplets are denoted $()_d$, in the following. A dynamic model of fragmentation and coalescence that corresponds to the real physics is therefore crucial in many multiphase CFD simulation. A short description of the main mechanism will be presented in the following text. The theory is based on Kolev (2005) and Pilch et al. (1981)

When neglecting the diffusion, the time-averaged conservation equation for a droplet quantity is expressed as

$$\frac{\partial}{\partial t}(n_d) + \nabla(\mathbf{V_d} n_d) = \dot{n}_{d,kin} - \dot{n}_{d,coal} + \dot{n}_{d,sp} , \tag{2.31}$$

$\dot{n}_{d,kin}$ represents the generation or loss of droplets due to evaporation and condensation, $\dot{n}_{d,sp}$ is the droplet production term caused by fragmentation of droplets and $\dot{n}_{d,coal}$ is a sink term that represents decrease in number of droplets due to coalescence. Since there is no heat source in this study, the evaporation and condansation term, $\dot{n}_{d,kin}$, can be neglected.

#### 2.6.1.1 Fragmentation

There are two principal ways of fragmentation, droplet that disintegrates into a continuum and unstable droplets that disintegrates and forms finer droplets. Kolev (2005) states the following main characteristics and assumptions of a fragmentation process:

- The stable droplet diameter after fragmentation is $D_{d\infty}$.

- The duration time of a fragmentation process is $\Delta t_{br}$.
- The total mass of the droplets are the same as before fragmentation.
- The newly formed droplets has the same temperature.

If the maximum droplet diameter after the fragmentation, $D_{d\infty}$, and the droplet number density before the fragmentation is known, the time averaged production rate can be found:

$$\dot{n}_{d,sp} \approx \frac{n_d}{\Delta t_{br}} \left[ \left( \frac{D_d}{D_{d\infty}} \right)^3 - 1 \right] . \tag{2.32}$$

Equation 2.32 shows clearly the need of an estimation of the stable diameter after fragmentation and the duration of the fragmentation. The fragmentation process is induced by two main mechanism, acceleration induced fragmentaion and turbulence induced fragmentation.

### Acceleration induced droplet fragmentation

The critical Weber number is used as a limit to predict whether the droplet is stable or unstable. The droplet Weber number, $We_d$, describes the hydrodynamic stability, usually the ratio between the forces acting to destroy the droplet, shear forces, and the force acting to retain the shape, the surface tension. $We_d$ is

$$We_d = \overrightarrow{t} \pi D_d^2 / (\sigma_d \pi D_d) \ , \tag{2.33}$$

where $\overrightarrow{t}$ is the tangential forces per unit surface. After a fragmentation process the droplets are stable, and denoted $()_{d,\infty}$, with a Weber number, $W_{d,\infty}$, which is the critical Weber number defined as:

$$We_{d,\infty} \equiv \frac{\rho_g (u_g - u_{d,\infty})^2}{\sigma_d / D_{d,\infty}} \ . \tag{2.34}$$

Haas (1964) studied mercury droplets in air and found that fragmentation did not occur for droplets with $We_d \leqslant 5.20$ and for droplets with $We_d \geqslant 6$ it did. Experimental analysis shows that $W_{d,\infty}$ for low vicosity liquids are in the range of

$$5 < We_{d,\infty} < 20 \ , \tag{2.35}$$

with the most common value, $We_{d,\infty} \approx 12$ .

There is however a dependence of droplet Reynolds number in the given range of $We_{d,\infty}$ , equation 2.35, which is not accounted for above. The droplet Reynolds number is defined as $Re_d = (\rho(u_g - u_d)D_d/\mu)$. A new definition of $We_{d,\infty}$ with a correlation with $Re_d$ was developed for $Re_d > 200$. The value of $Re_d = 200$ was found by Schroede.RR and Kintner (1965), which reported that droplets only oscillate when a vortex tail is present. The vortex tail requires $Re_d > 200$. The dependence of $We_{d,\infty}$ on the viscosity was also considered and a correction factor applied, which is correlated with the Ohnesorge number, $Oh_d$. This has been confirmed experimentally. $Oh_d$ is defined as

$$Oh_d = \mu_d/\sqrt{\rho_d D_d \sigma_d} = \sqrt{We_d}/Re_d \ . \tag{2.36}$$

Pilch et al. (1981) stated that for low viscous droplets, $Oh_d < 0.1$, the approximation of $We_{d,\infty} \approx 12$ is applicable. Kolev (2005) recommends however the following expression based on both the initial $Re_d$ and $Oh_d$. For $We_d > We_{d,\infty}$ and $Re > 200$ the droplet is unstable, and the following expression for $We_{d,\infty}$ for droplets in gas can be used

$$We_{d,\infty} = 55\left(\frac{24}{Re_d} + \frac{20.1807}{Re_d^{0.615}} - \frac{16}{Re_d^{2/3}}\right)[1 + 1.077Oh_d^{1.64}] \ , \tag{2.37}$$

for $200 < Re_d < 2000$ and

$$We_{d,\infty} = 5.48[1 + 1.077Oh_d^{1.64}] \ . \tag{2.38}$$

for $Re_d > 2000$. Based on equation 2.34, one can calculate $D_{d,\infty}$, but an estimation of the droplet velocity after fragmentation, $u_{d,\infty}$, is needed. This is done by modifying the momentum equation for the the relative velocity between the continuum and dispersed phase, $u_g - u_d$,

$$\left[1 + \left(\frac{\alpha_g\rho_g + \alpha_d\rho_d}{\alpha_g\rho_g}\right)C_{vm}\right]\frac{\partial(u_g - u_d)}{\partial t} + \left(\frac{1}{\rho_g} - \frac{1}{\rho_d}\right)\nabla p \\ + \frac{\alpha_g\rho_g + \alpha_d\rho_d}{\alpha_g\rho_g}\frac{3C_d}{4D_d}|u_g - u_d|(u_g - u_d) = 0 \ , \tag{2.39}$$

where $C_d$ is the drag coefficient and $C_{vm}$ is the virtual mass coefficient. Pilch et al. (1981) used experimental data and equation 2.39 to find an empirical description of the final fragment velocity. Pilch et al. (1981) recommends the following correlation

$$u_{d,\infty} = u_g\sqrt{\rho_g/\rho_d}\left(\frac{3}{4}C_d\Delta t_{br} + 3b\Delta t_{br}^2\right) \ , \tag{2.40}$$

where $C_d = 0.5$ and $b = 0.078$ for incompressible fluids and evaluated the break-up time from experimental data, see table 2.1, and calculated by means of the Weber number for the initial droplet, $We_d$

$$We_d = \frac{\rho_g(u_g - u_d)^2}{\sigma_d/D_d} \tag{2.41}$$

The different break-up modes will not be further discussed in this thesis, but the reader is refered to Kolev (2005),Pilch et al. (1981) and Crowe (2006) for further information.

To summarize the fragmentation study: $W_{d,\infty}$ is defined in equation 2.34 and can be calculated by equation 2.37 and equation 2.38. The final velocity of the fragments is found from equation 2.40, where the break-up time is estimated in table 2.1. Knowing this, one can compute the diameter after the fragmetation

Table 2.1: Break up time for low viscous fluids, $Oh_d < 0.1$. (Pilch et al., 1981)

| Break-up time correlation | Lower limit for $We_d$ | Upper limit for $We_d$ | Brak-up mode |
|---|---|---|---|
| $\Delta\tau_{br} = 7(We_d - W_{d,\infty})$ | 1 | 12 | Vibration mode |
| $\Delta\tau_{br} = 6(We_d - W_{d,\infty})^{-1/4}$ | 12 | 18 | Bag break-up |
| $\Delta\tau_{br} = 2.45(We_d - W_{d,\infty})^{1/4}$ | 18 | 45 | Bag- stammen- break-up |
| $\Delta\tau_{br} = 14.1(We_d - W_{d,\infty})^{-1/4}$ | 45 | 351 | Sheet stripping |
| $\Delta\tau_{br} = 0.766(We_d - W_{d,\infty})^{1/4}$ | 351 | 2670 | Catastrophic break-up |
| $\Delta\tau_{br} = 5.5$ | 2670 | $\infty$ | |

$$D_{d,\infty} \approx We_{d,\infty}\sigma_d/[\rho_g(u_g - u_{d,\infty})^2] \ . \tag{2.42}$$

### Turbulence induced droplet fragmentation

A droplets reaction to a fluctuation in the surrounding continuum can be analysed by studying the simplified momentum equation 2.39, for a single droplet in a gas phase. The local acceleration in a turbulent field is dependent on the size of the vortex and the turbulent characteristics. Neglecting the drag force and gravity forces equation 2.39 reduces to

$$\frac{\partial(u_g - u_d)}{\partial t} = \frac{\rho_d - \rho_g}{\rho_d + \rho_g C_{vm}} \frac{\partial u_g}{\partial t} \ . \tag{2.43}$$

From equation 2.43 one can clearly see that the velocity difference between a droplet and the continuum phase may increase, since $\rho_d > \rho_g$. Since the turbulent fluctuations in a turbulent field can induce a higher velocity difference a new way of calculating the velocity difference based on turbulent characteristics is required. Kolev (2005) shows that the maximum velocity difference can be expressed as:

$$\Delta(u_g - u_d)^2_{max} = (\rho_d - \rho_g)\frac{\epsilon_g^{2/3} l_{eg,max}^{2/3} + g l_{eg,max}}{\rho_d + \rho_c C_{vm} + \rho_g \frac{3}{4}\frac{Cd}{D_d} l_{ec,max}} \ , \tag{2.44}$$

where $\epsilon_c$ is the turbulent dissipation ratio for the continuum and $l_{ec}$ is the length scale of the small eddies. Droplets in gas field will obey the mechanical stability criterion as discussed in the previous section, but with the velocity calculated from equation 2.44.

#### 2.6.1.2 Coalescence

Coalescing of droplets is caused by the existence of a velocity difference between the droplets. There are several outcomes of two colliding droplets. Figure 2.3 shows the different outcomes from hydrocarbon droplet collisions, (Crowe, 2006). The different regimes are defined by the collision parameter, $B$, and $We$ relative to the colliding droplet. $B$ is defined as

$$B = \frac{\chi}{r_1 + r_2}, \tag{2.45}$$

where $\chi$ is the distance between the droplets and $r$ are the radius of the two colliding droplets. $We$ relative to the colliding droplets is defined as

$$We = \frac{\rho_d u_{rel,d}(r_1 + r_2)}{\sigma}, \tag{2.46}$$

where $u_{rel,d}$ is the relative velocity between the droplets. $B = 0$ imply a head on collision, while $B = 1$ imply a grazing collision. Inertia dominated collisions, high $We$ and low $B$, corresponds to regime (c) and (d) in figure 2.3. The collision results in a deformation of the droplets and the creation of a expanding thin film surrounded by a rim. This leads to two possible outcomes, the liquid film could recede an thereby cause coalescence or the liquid film continues to expand until fragmentation. The stretching separation, high $We$ and high $B$, leads to a stretching filament which gets fragmented.

At low $We$ the outcome of collision are either bouncing or coalescence. This is the most relevant regime for the droplets in the vane pack. The phenomena is governed by the film located in the gas/liquid gap between the colliding droplet. The process can roughly be divided into three main phases, the colliding phase, film drainage phase and at last either bouncing or coalescence. If the film ruptures, the droplets coalesce, which occur if the thickness of the film is drained to the characteristic distance connected to the van der Waals force (Crowe, 2006).

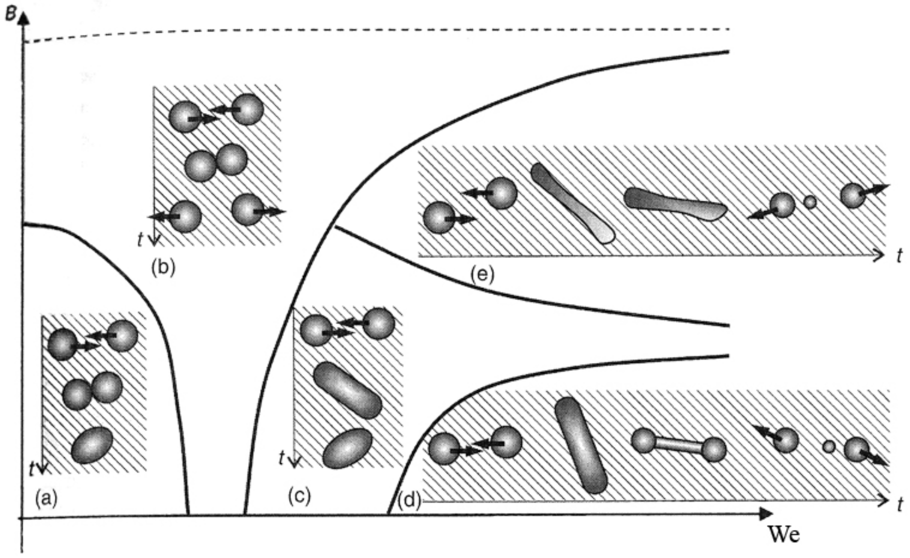

Figure 2.3: Schematic overview of the different regimes for hydrocarbon drop collision. (a) coalescence; (b) bouncing; (c) coalescence; (d) reflexive separation; (e) stretching separation. Taken from (Crowe, 2006)

A typical approach for numerical modeling of droplet collisions, where the outcome is either coalescence or bouncing, are to define a coalescence frequency. The coalescence production term can then found by multiplying the coalescence frequency and the droplet number density (Kolev, 2005),

$$\dot{n}_{d,coal} = -f_{d,coal} n_d / 2, \tag{2.47}$$

where $f_{d,coal}$ is the coalescence frequency.

The coalescence frequency is a product between the collision frequency and the coalescence probability. The calculation of the collision frequency is typically based on the relative velocity between droplets, droplet diameter and $\alpha_l$. The outcome of the collision is then decided by the coalescence probability, usually a stochastic variable with two outcomes.

#### 2.6.1.3 Film behavior

Physics that arises if a film is present to droplets and turbulence are, wavy film surface due to the surrounding fluid and droplet crash on film surface. A criteria called the

Kelvin-Helmholtz instability describes the minimum gas velocity for a film to become wavy. From this wavy surface, droplets could get sheared off and taken into the gas flow. Droplets that impacts on the film surface do either stick to the surface, bounce back into the gas flow, coalesce into the film or splash. Droplets that have a high inertia and velocity difference between the film and droplet, will splash into the film, which means that the droplets forms a crater in the film surface with a surrounding crone. The crone can then get fragmented and re-entrain droplets into the gas flow.

In numerical modeling of droplet - film interaction, in a macro perspective, the outcome of the impact are often sharply categorized by the energy of the droplet and the impact angle. Experiments by Duez (2007) shows however that the outcome of the impact are not only dependent of these variable, but also to other unforeseen variables. These experiments with water showed, among others phenomena, that super hydrophobic impacts creates a splash at any velocities.

## 2.7 Discrete Phase Modeling

As mentioned the DPM in Fluent allows one to simulate a dispersed phase in a continuum, with a liquid film on the walls. The following section is a short description of the available models, please refer to the Ansys (2009) for a thoroughly description.

The DPM model is suitable for simulations of particles, droplets and bubbles. Simulations in this thesis will focus on dispersed droplets in a gas continuum. The droplet trajectories are calculated in a Langrangian reference frame. When neglecting the gravity and the viscosity in the droplet, one achieves the following force balance for a spheric droplet:

Particle acceleration:

$$m_d \frac{d\overrightarrow{u}_d}{dt} = \overrightarrow{F}_{drag} + \overrightarrow{F}_{virtualmass} + \overrightarrow{F}_{pressure} + \overrightarrow{F}_{other} \ . \tag{2.48}$$

Drag force:

$$\overrightarrow{F}_{drag} = m_d \frac{3}{4} \frac{\rho_g C_d}{\rho_d D_d} |\overrightarrow{u}_g - \overrightarrow{u}_d| (\overrightarrow{u}_g - \overrightarrow{u}_d) \ . \tag{2.49}$$

Virtual mass:

$$\overrightarrow{F}_{virtualmass} = \frac{m_d}{2} \frac{\rho_g}{\rho_d} \frac{d(\overrightarrow{u}_g - \overrightarrow{u}_d)}{dt} \tag{2.50}$$

Pressure force:

$$\overrightarrow{F}_{pressure} = -\frac{m_d}{\rho_d}\nabla p \ . \tag{2.51}$$

Other forces can be forces due to rotational reference frames, thermophoretic forces, brownian forces, staffman lift forces and user-defined forces. The chosen drag coefficient, $C_d$ is the Morsi-alexander coefficient and defined as:

$$C_d = a_1 + \frac{a_2}{Re_d} + \frac{a_3}{Re_d} \ , \tag{2.52}$$

where the constants $a_1$, $a_2$ and $a_3$ apply to a smooth spherical droplet. The droplet Reynolds number is defined as

$$Re_d = \rho_g D_d(u_g - u_d)/\mu \ . \tag{2.53}$$

The DPM model is the only multiphase model in Fluent which can optionally include all of the following physical characteristics, fragmentation, change off diameter, particle-wall collision, particle-particle collision and coalescence. The following section give a short description of the implemented models.

**Coupling between phases**

The discrete phase has their own set of equations and algorithms apart from the Fluent solver. This leads to a specific convergence behavior and settings, and the convergence of the coupled flow will fail if the discrete phase algorithms fails. The two-way coupling transfers momentum and energy between the continuous phase and the dispersed phase, and is considered by source terms, see figure 2.4. The procedure for a two-way coupled transient simulation is listed in table 2.2

## 2.7.1 Fragmentation model

The fragmentation process is modeled in two ways in Fluent, the Taylor Analogy Breakup, TAB, model which fits well for low $We_d$ injections and the wave-model which fits for high $We_d$ injections. In principle the TAB-model covers vibration-, bag- and bag-stammen-break-up, while the wave model covers sheet stripping and catastrophic break-up, see figure 2.5. The droplets in this thesis will be injected with a small relative velocity, which gives a low $We_d$, so the TAB model is chosen. The TAB model uses the Taylor analogy between a distorting and oscillating droplet and a spring mass system, where the restoring force of the spring is analogous to the surface tension, external force on the

Table 2.2: Procedure for coupling a transient DPM simulation

```
↱       • Freeze continuous gas phase field.
|   ↱   ○Take particle at current position.
|   |   ○ Compute the droplet time steps based on local velocity.
|   |   ○ Integrate trajectory, until the droplets leaves the domain,
|   |     deposite on the wall or the flow time step is reached.
|   |   ○ Store droplet at new location and step to next particle
|       • Continue with the continuous gas phase time step
```

spring to the droplet drag force and damping force in the spring to the droplets viscosity force. When the distortion and oscillation of a droplet exceeds a critical value the droplet breaks into secondary droplets. Please refer to Ansys (2009) and O'Rourke and Amsden (1987) for more information.

### 2.7.2 Coalescence model

Fluent offers one droplet collision model in DPM simulations, which is shortly described in the following and mainly based on Ansys (2009). In a droplet spray with $N$ droplets, there are $N-1$ possible collision pairs, and thereby $\frac{1}{2}N^2$ possible collision pair. There could be several million droplets in a typical spray, and the computational cost to treat all combinations is impracticable. This is solved by a simplification and an algorithm developed by O'Rourke and rewritten in Ansys (2009). First the number of computational elements is reduced by using parcels to represent a number of individual droplets, e.g. if a set parcel represents $10^i$ droplets each, the number of possible collision partners are reduced by $(10^i)^2$. The computational cost may, however, still be impracticable large.

The algorithm by O'Rourke is a stochastic estimations of collision. If the continuous phase cells are small compared to the spray size, the developer claims that the method is second order accurate for collisions. Only parcels in the same continuous phase cell can collide. The collision has only two outcomes, coalescence and bouncing, based on the $We_d$ and an accommodation to experimental data. A problem of this approach is that

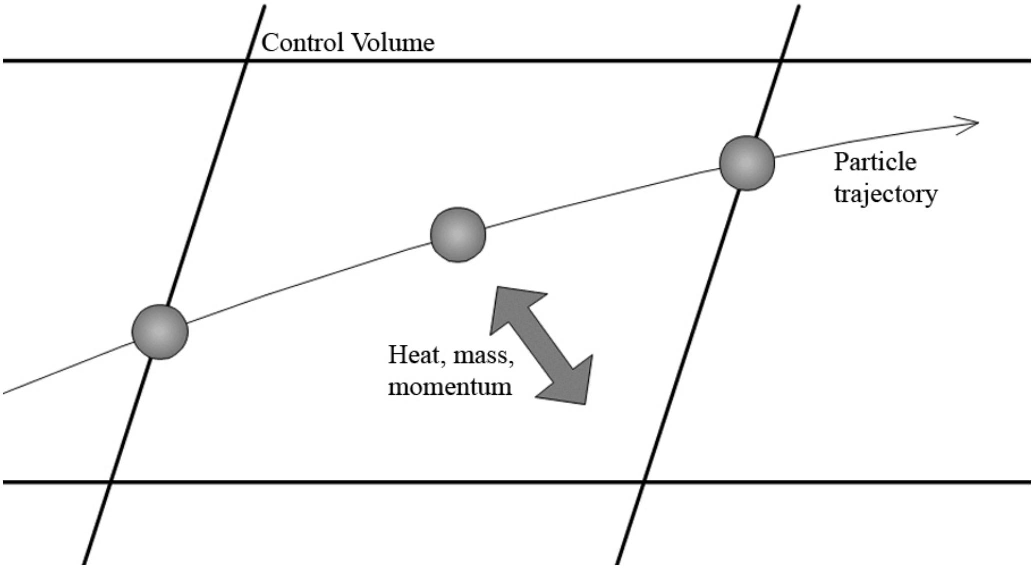

Figure 2.4: Principle drawing of the coupling between the phases

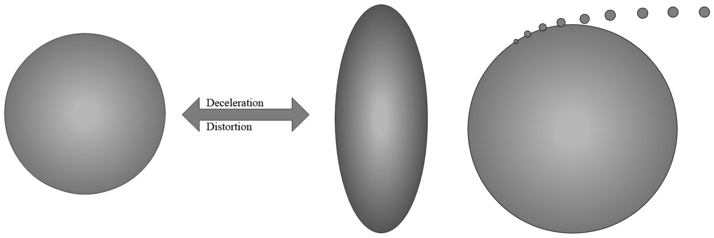

(a) TAB-model (b) Wave-model

Figure 2.5: Principle drawing of the the two different fragmentation models

two parcels that are close to each other, but not in the same cell, will not collide. This error is reduced by letting some parcels which are further apart to collide. If the particle time step is too large, the result of the simulation can be time dependent, because the model assumes that the frequency of collisions is much smaller than the particle time step. The model is also most applicable for low Weber number collisions, where bouncing and coalescence is the result of a collision.

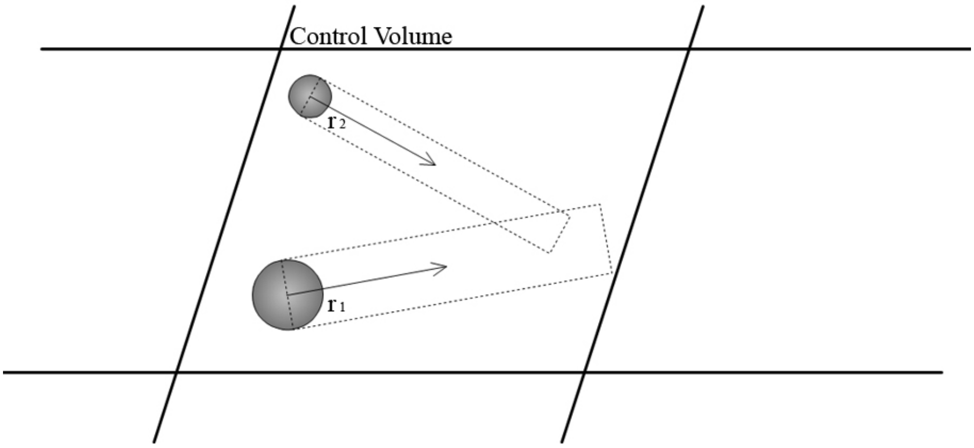

Figure 2.6: Principle drawing of the coalescence model

### 2.7.3 Wall-Film Model

The wall-film model in Fluent is designed for mixture formation process in port fuel injected engines, where a fuel spray impinges on a surface and subsequently evaporates. Still, this is the only available option to apply a dynamic liquid film on the wall, and many of the features in the model should fit well with the mechanism in the vane pack flow. This short introduction is based on Ansys (2009) and Stanton (1995).

The model is activated by implementing the model on the desired wall boundaries. There are three main mechanism in the model, interaction during the initial impaction with a wall, subsequent tracking on surface, calculating film variables and the coupling with the gas phase. Fluent lists up the following assumptions and restrictions to the model:

- The film thickness is thin, less than 500 microns, due to the assumption that the velocity field is linear in the film.

- Film particles are assumed to be in direct contact to the wall.
- The film temperature never exceeds the boiling temperature of the liquid.
- The simulation has to be transient.

The droplets that collide with the wall boundaries are divided into four different regimes, based on the wall-temperature and the impact energy: stick-, rebound-, spread- and splash- regime. When the wall temperature exceeds the boiling temperature of the liquid, the droplets will either rebound or splash, but this will not be the case for the simulations in this thesis. This leaves three regimes for this particular simulations, stick spread or splash, only based on the impact energy

The impact energy is a modification of $We_d$ relative to the impinging droplet and wall. The outcome of the different impingement regimes is illustrated in figure 2.7.

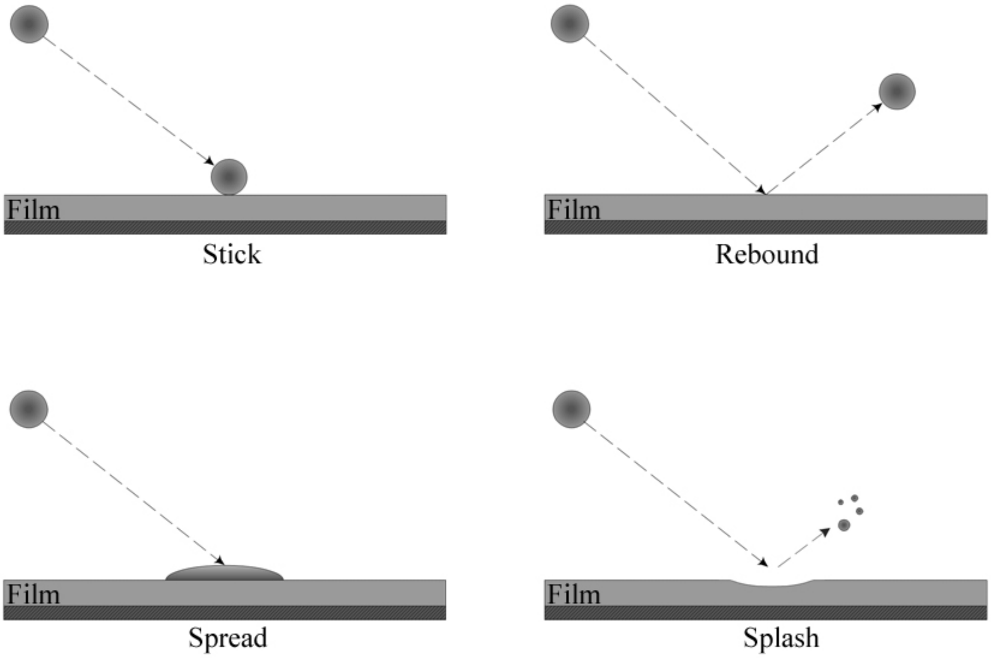

Figure 2.7: Different impignement regimes in the wall-film model

When the impact energy is extremely low, droplets adhere to the film surface with a spherical shape. This regime is called the stick regime. The droplet velocity is set equal to the wall velocity and the droplet will coalesce with the film. The behavior and criteria of the regime is based on different experimental data.

The spread regime is similar to the stick regime, but occurs at higher impact energy. The droplets coalesce with the film upon impact, and the initial direction and velocity is set by using the wall-jet model. The criteria for the spread regimes lays between the stick regimes and the critical energy threshold.

$$E_{stick\ regime} < E < E_{cr} \tag{2.54}$$

When the impact energy is higher than the critical energy threshold, droplets will splash on the wall-film. The impinging droplets forms a crater on the film and with encircling crown which break up into secondary droplets, figure 2.8 There are many quantities that has to be calculated in this regime, e.g. the quantity of the droplet mass that embodies into the film, the size, direction and velocity of the secondary droplets. An eventual film on a wall will suppress splashing, but at the same time not give unphysical results when the film height approaches zero. In Fluent the number of secondary droplets created by each impact are explicitly set by user.

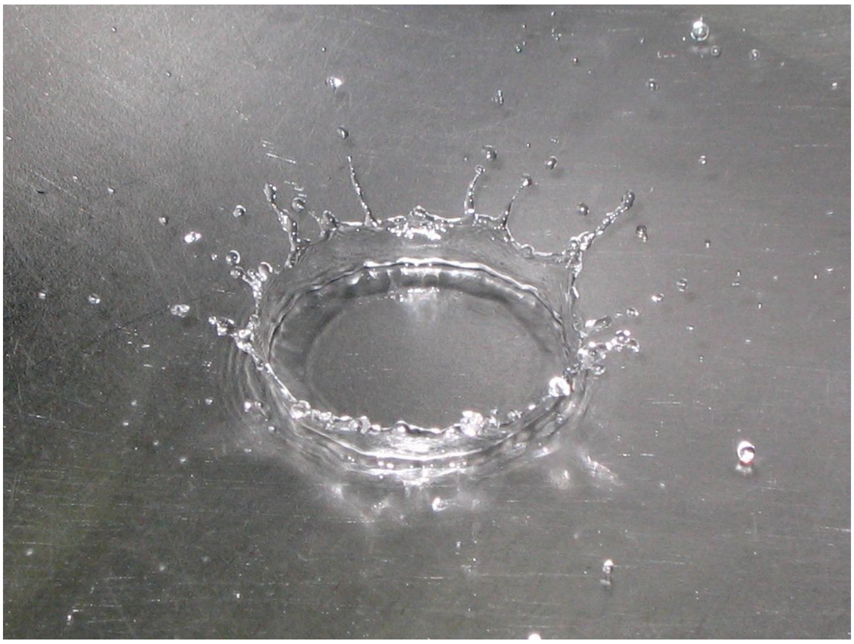

Figure 2.8: Droplet splash

# Chapter 3

# One-phase simulation

A simulation of a multiphase turbulent flow is challenging and credible results are difficult to achieve, since each phenomena alone are challenging. For this reason a one-phase turbulence simulation and a two-phase turbulence simulation were preformed.

The strategy was to investigate the performance of different turbulence models, on a simplified vane pack geometry, and then check the grid quality. And finally simulate the flow inside a vane pack as a turbulent one-phase flow and connect the result with relevant theory around two-phase behavior.

## 3.1 Preliminary calculations

From section 2.5 it was obvious that the choice of turbulence model had to be evaluated. In this section different models are tested. The physical problem is transient and thereby all models tested are unsteady. Different models are usually categorized based on the amount of turbulence energy they model, illustrated in figure 3.1. Four different models have been tested, SST, DES, SAS and LES. The objectives are:

- To determine which models that have an unsteady solution.
- To study the different models capability to represent three dimensional effects.
- To give a rough estimate of where the hybrid models have their cut-off in the energy spectrum.
- And finally decide which model that is most appropriate to use on the NJORD cluster.

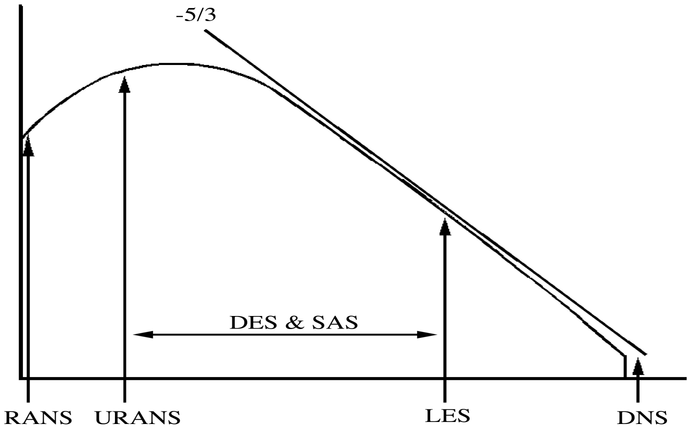

Figure 3.1: Illustration of the energy spectrum, and which parts that are resolved by the different models. For each model the right hand side is modeled.

The simulations in this section where preformed on a 3GHz Pentium4 dual core processor with 3.5Gb RAM and Microsoft Windows XP 32bit operating system.

### 3.1.1 Computational domain

As discussed by Carlson and Talseth (2008) a fluid flow involving separation points is challenging to compute with CFD, especially when the separation points are not clearly set by the geometry. There were two domains available, the reference geometry and geometry 2. Since the purpose of geometry 2 was to remove re-circulation bubbles, the separation points are weakly present or not present at all. This is the reason for why geometry 2 was chosen as domain for the turbulence model study. If the reference geometry had been used, the performance for each model may have been different, and when the models further had been tested on geometry 2 they might not have worked properly. The reference geometry are further called ref and geometry 2, geo 2.

The calculations have been performed on a section of geo 2, see figure 3.2. The geometry has two lines, which are oriented perpendicular to the middle line of the geometry. The width of the channel, s, at these lines are the same and the distance from the bottom wall are i. Coming figures are plotted against the fraction $\frac{i}{s}$, the convex side of each bend has a low pressure, LP, zone and the concave side a high pressure, HP, zone.

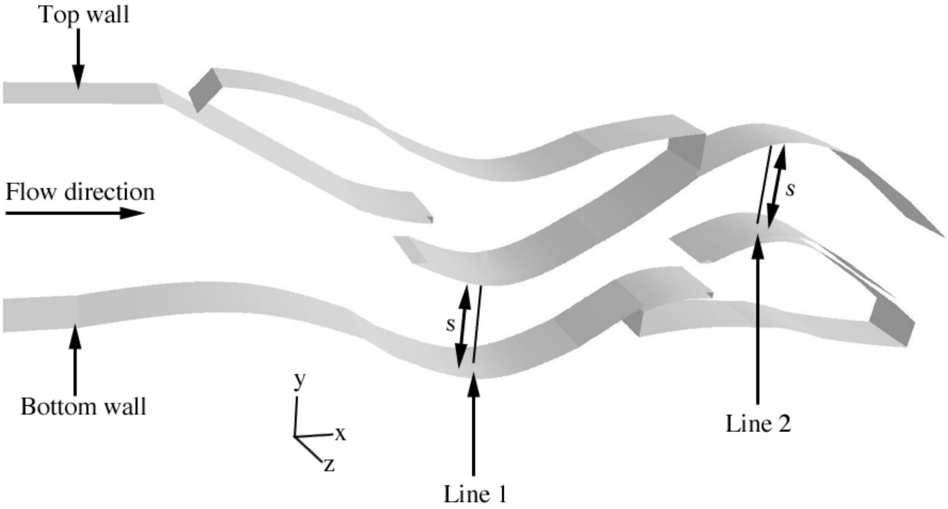

Figure 3.2: The test geometry for the preliminary calculations, a section of geometry 2, with the lines where the data has been reported.

### 3.1.2 Numerical setup

A CFD simulation is dependent on the choice of grid, and each model has it's own ”perfect” grid. A grid study for each model was not preformed due to limitations in time. The proposed grid in Carlson and Talseth (2008) was used. It should be noted that this grid was designed for 2D simulations where the focus was to optimize it for RANS modeling, and it might therefore be favorable for this modeling technique. The grid has a BL in the y-direction of the flow, with a growth factor of 1.2 on 20 cells. The wall adjacent cell is within $y^+ = 1$ and the mean cell is $0.31mm$. The geometry was stretched with 20 cells in the third direction giving a total of 695100 grid cells and a span in z of $6.2mm$. A vane pack on a platform is typically 1-2 meter in z, giving a hydraulic diameter of 56mm. The small span in the z-direction will be negative for the models that manage to solve some turbulence, since the fluctuations in the third direction will be limited by the boundary condition in the z-direction. There where two possible boundary conditions at these boundaries, either define the walls in the z-direction with slip condition, or as periodic. Slip condition allows the fluid to have velocity along the wall, but limits the perpendicular velocity to zero. The periodic boundary condition means that everything that goes out on one side comes in on the other side. Both alternatives will remove the viscous contribution from a boundary layer on the z-boundaries, which is positive regarding the

Reynolds number. The slip wall will anyhow force the z-velocity component down to zero adjacent to the z-boundary and it will lower the Reynolds number, equation 2.1, through the hydraulic diameter. The Reynolds number is less affected with the periodic condition, since one can say that the hydraulic diameter becomes, somehow, less affected. The periodic condition was applied. It has to be mentioned that the periodic condition will limit the turbulent structures down to be less than $6.2mm$ in the z-direction. The inlet was defined with a Dirichlet condition that specified the inlet velocity, $U_0 = 1.0131m/s$. A Neumann condition was used at the outlet. No-slip condition was applied to the walls, the walls are shown in figure 3.2. Transient CFD simulations need a step size in time, the time step should allow a fluid particle to at least be in a grid cell once each time step, this is called the Courant-Friedrichs-Lewy, CFL, condition and is for one-dimesional cases given by

$$\frac{u\Delta t}{\Delta x} < CFL \tag{3.1}$$

In this case the CFL was set to 0.5, meaning that a fluid particle spend two time steps or more to travel through a cell. The time step size was calculated with the use of the inlet velocity, giving a $\Delta t = 0.0002s$. If one can say that the periodic boundary condition is similar to infinite length in z the $Re$ number will be 137.580. Equation 2.3 gives an estimate of the separation of the scales,

$$\begin{aligned}\text{Length scale: } \frac{\eta}{l} &\approx \frac{1}{7150}\,, \\ \text{Time scale: } \frac{\tau}{T} &\approx \frac{1}{370}\,, \\ \text{Velocity scale: } \frac{v}{v} &\approx \frac{1}{20}\,.\end{aligned}$$

The largest scales can be of the size of s in the geometry, which are $20mm$. This gives an estimate of the smallest scales to be around $0.0028mm$. Approximately 110 times smaller than the mean grid cell size. From these estimates it is clear that the size of the grid is the most problematic factor.

All models, except LES, need a turbulence intensity, $I_t$, at the inlet boundary, together with a hydraulic diameter, $D_h$, to estimate the influence of the turbulence at the inlet boundary. The $I_t$ was set to 3% together with a $D_h$ of 56mm. The assumption of a infinite channel was used. The LES initial boundary condition was set to No Perturbations, meaning that the stochastic components at the velocity inlet are neglected. Carlson and Talseth (2008) concluded that for a RANS model, the turbulence intensity at the inlet was not of particular importance, but that most of the turbulence were generated inside the vane pack. In addition the flow is coming from the settling zone in the scrubber vessel where the cross section area are much larger, low $Re$, than the cross section in the vane pack, higher $Re$ than before the inlet.

All the simulations had a convergence criteria of $10^{-3}$ and they where all calculated for approximate 1.3 seconds, real time, which corresponds to ten flow throughs, and 6500 timesteps. Central differencing was used for LES, DES and SAS and first order upwind for the SST model. Discretization schemes with smaller truncation error would have given a better solution, but the focus in this thesis was not to minimize the numerical error.

### 3.1.3 Results

Instantaneous velocity and turbulent kinetic energy, $k$, were dumped to text files on every timestep. The turbulent kinetic energy dumped from Fluent will be referred to as modeled $k$. For the LES simulation only the instantaneously velocity was dumped. Average velocities were calculated from the text files and turbulent kinetic energy for LES and SAS was calculated by the formula

$$k = \frac{1}{2}(\overline{u'^2} + \overline{v'^2} + \overline{w'^2}) \tag{3.2}$$

$$\text{with } \overline{u'_i u'_i} = \frac{\sum_{i=1}^{N}(u(t) - U)^2}{N} \ . \tag{3.3}$$

Calculating $k$ from this definition will only give the part of $k$ that is being resolved by the model, called resolved $k$.

A code for importing the data and then calculating the outputs was written in Visual Basic, see Appendix D. The code was optimized since it further was used on the post processing of the data from the cluster, and it was programed to handle both windows- and linux- syntax on the data files.

Figure 3.3a shows the instantaneous velocity for $\frac{i}{s} = 0.99$ on line 1, close to the convex wall. As seen in figure 3.3a DES uses approximately 2600 time steps to initiate fluctuations around a mean velocity, which is almost 40% of the total simulation time. LES starts fluctuating after 4% of the total simulation and SAS after 12% of the total simulation time. So DES uses approximately ten times as much CPU time to get unstable, compared to LES. DES also poorly resolves the unsteady motion since it has a noticeably lower amplitude on the fluctuations, as can be seen from time step 2500 in figure 3.3a and in figure 3.4. Ansys (2009) says that the DES needs to be triggered towards "LES mode", which can be seen by comparing line 1 with line 2 in figure 3.4. The reason for the bad DES performance is caused by the switch function or more correct, the grid. Revisiting the treatment of the dissipation term of turbulent kinetic energy, $Y_k = \rho\beta * k\omega max(\frac{L_t}{C_{DES}\Delta}, 1)$, here presented without the blending function, to make it clearer for the reader. "LES mode" is when the first term in the max statement is active, so if the $\Delta$ is too large the standard SST equations are active. Since the DES solution became mildly unstable the $\Delta$ is probably too large. A plot of the "LES mode" are shown in figures 3.3b,3.3c, and it is clear that the "RANS mode" are not only acting adjacent to the wall. The switch from "RANS mode" to "LES mode" happens too far away from the wall and need one bend to be triggered over to LES mode. It would probably had worked better for the reference geometry, since it has a more separated flow. DES is not working well with this grid on geometry 2, so it will not be included in the graphs further.

Figure 3.4 shows the instant velocity for line 1 and line 2. Line 1 is shown in figures 3.4a, 3.4c, 3.4e and line 2 in figures 3.4b, 3.4d, 3.4f. At line 1 SAS generates unsteady motion at the LP side, and here it is similar to the LES solution. The max amplitude of the fluctuations are almost similar to the max amplitude for LES at LP sone on line 1. At the middle of line 1, figure 3.4c, SAS generates a steady frequency with constant amplitude for the velocity, which seems unnatural for turbulence, but maybe natural for the mean flow. At the HP zone at line 1 SAS has a mildly unsteady motion compared to LES. Further downstream on line 2 the SAS solution became more unsteady at all three points. It is being more "triggered" by the flow, so that the SAS capability is working in the whole channel. Small fluctuations upon the bigger fluctuations can be seen for the LES, this might come from the fact that LES resolves smaller structures than SAS. SST has a stationary solution.

The average velocity profile for the two lines are shown in figure 3.5. The profiles have been averaged between timestep 1000 and 6500. None of the models give re-circulations bubbles, meaning that if there are re-circulation it is generated and destroyed between these two lines. SST has the highest velocity profiles and similar shape, except for $\frac{i}{s} = 0.9 - 1.0$. There is similarity between SAS and LES on line2, except that SAS has a peak around $\frac{i}{s} = 0.1$. Steeper profiles are seen for the LES simulation on both lines close to the walls.

As mentioned in section 2.5, SAS is a modified version of the SST k-w model and it is therefore interesting to see that the SAS term makes the SAS result more similar to LES than SST.

Figure 3.6 shows the average z-velocity at line 2, where $\frac{i}{s} = 0$ is a LP zone and $\frac{i}{s} = 1$ is a HP zone. SST generate very small velocities at the LP side of the bend, and zero velocity in the rest of the channel. The LES model has some three dimensionality in the whole channel, with a peak around $\frac{i}{s} = 0.01$. The SAS model has negative velocity in the middle of the channel, a small positive peak at the LP zone and a high peak at the HP

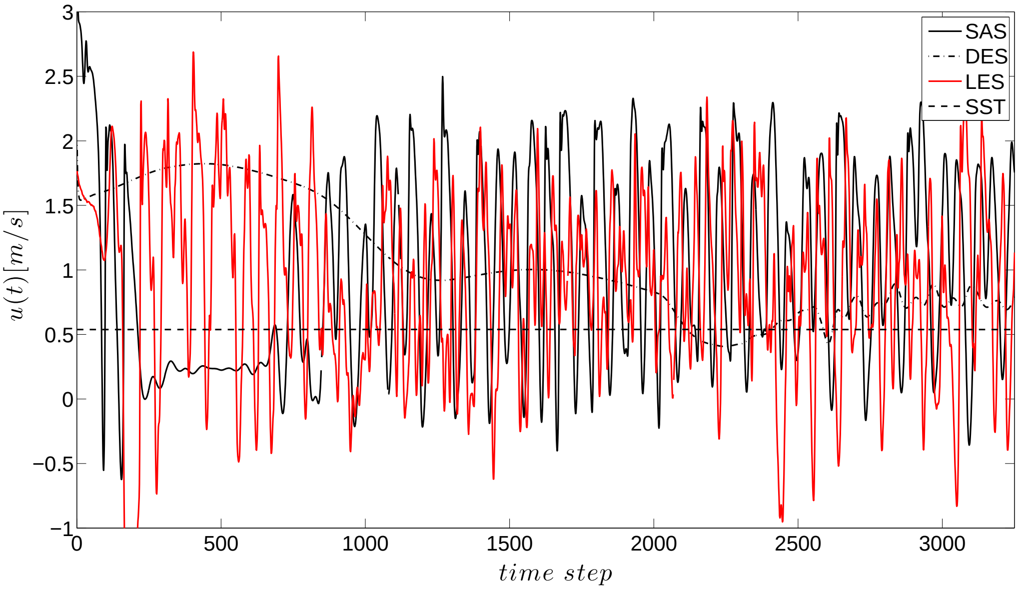

(a) Instant velocity for $\frac{i}{s} = 0.99$ Line 1

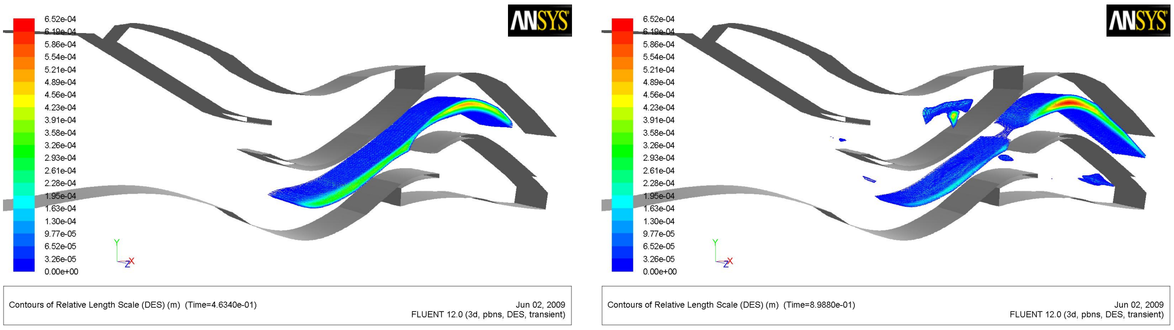

(b) Contours of $L_{rel}$, with a sharp contour cut-off at $Lrel = 0$, at $t = 0.46s$

(c) Contours of $L_{rel}$, with a sharp contour cut-off at $Lrel = 0$, at $t = 0.90s$

Figure 3.3: Figures illustrating the problem with DES at this case.

zone. LES and SAS have a clear three dimensional solution, but they are not at all similar at the HP side of the bend. The phenomena turbulence is of three dimensional fashion, a functioning transient model should re-generate some motion in the third direction. SAS and LES are the only models that have three-dimensional effects. SST in this particular case is suitable for two dimensional simulations.

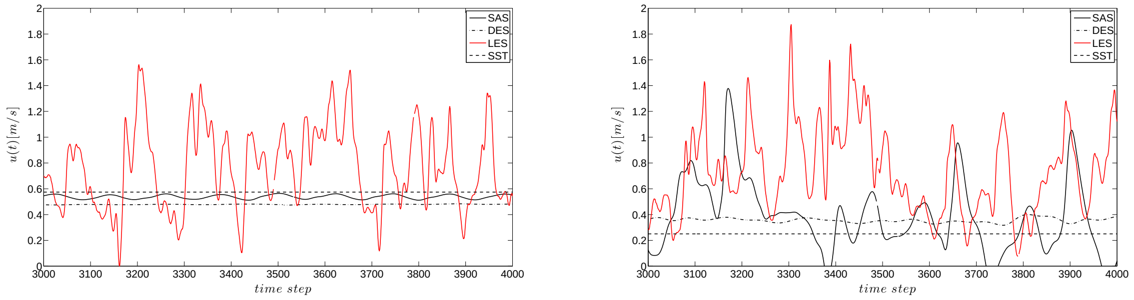

(a) $\frac{i}{s} = 0.01$, HP, line 1 (b) $\frac{i}{s} = 0.99$, HP, line 2

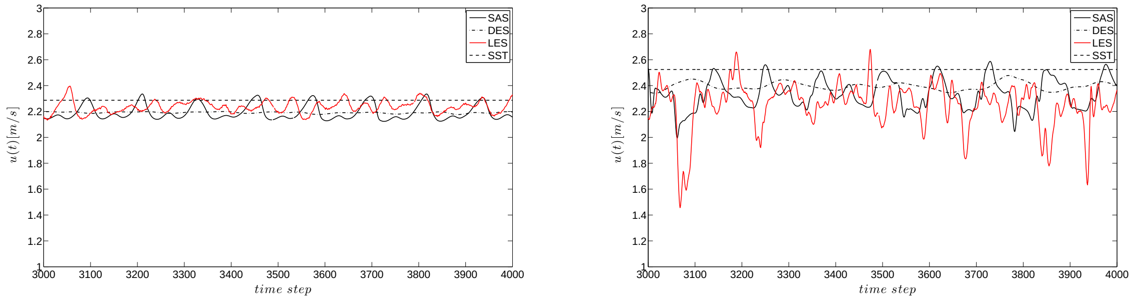

(c) $\frac{i}{s} = 0.50$, line 1 (d) $\frac{i}{s} = 0.50$, line 2

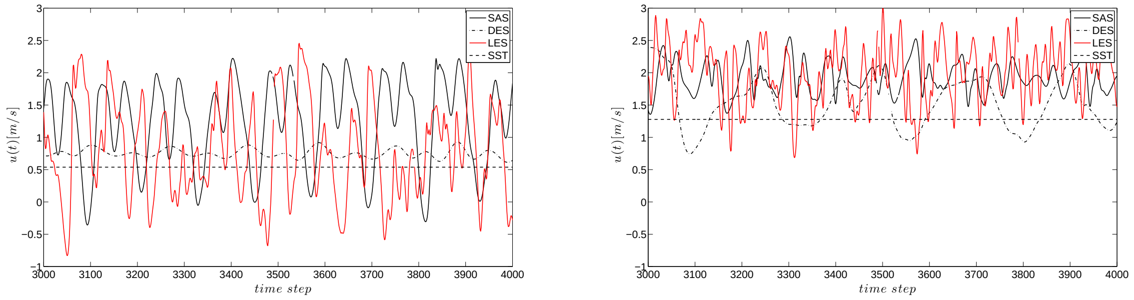

(e) $\frac{i}{s} = 0.99$, LP, line 1 (f) $\frac{i}{s} = 0.01$, LP, line 2

Figure 3.4: Instant velocity at three different positions on line 1 and line 2, for five different turbulence models. HP=high pressure zone, LP=low pressure zone.

Figure 3.8 shows turbulent kinetic energy, k, divided by the inlet kinetic energy, $\frac{1}{2}U_0^2$, for both lines. $k_{LES}$ and $k_{SAS}$ have been calculated from the definition in equation 3.3, this $k$ is resolved by the models. For SAS and SST one can report the modeled $k$. For LES this is not possible, since this part is being dissipated by the subgrid-scale model. If one adds the modeled part with the resolved part one gets the total $k$. For a perfect model, $k$ total should be consistent with a $k$ from a DNS. Absolute values in this figure must not be paid specially attention to, since their correctness can not be stated without velocity measurements or DNS data. LES provides a $k$ that is lower than SAS for almost both lines, except on line 1 at the HP sone. The reason for the low values from LES

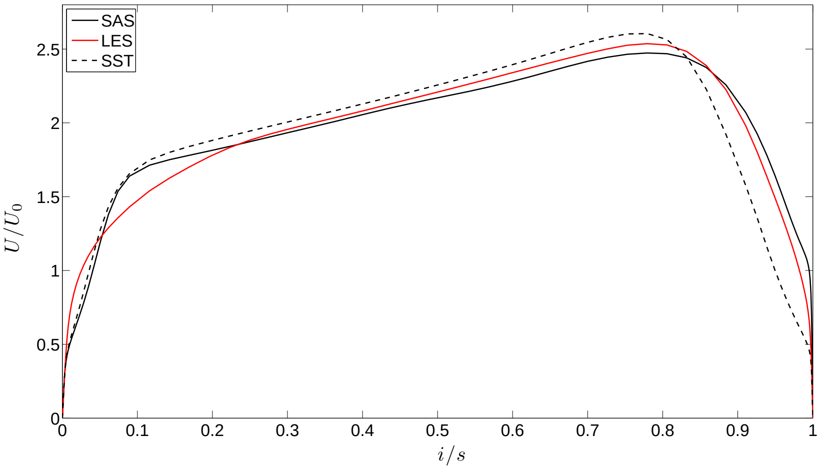

(a) $\frac{U}{U_0}$ profile for line 1

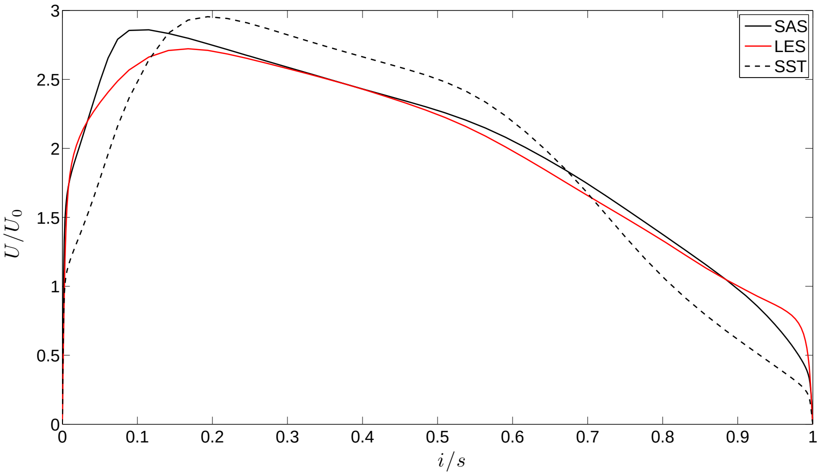

(b) $\frac{U}{U_0}$ profile for line 2

Figure 3.5: Average velocity, $U$, divided by the inlet velocity, $U_0$ on line 1 and 2 for five different turbulence models

are probably because the mesh size that sets the filter cut-off are too big. The resolved $k_{SAS}$ has the highest value compared to $k_{LES}$, which is strange, since it also, somehow, is limited by the cell size. An interesting test would have been to do a SAS on a coarser grid, and then see if the total $k$ is the same. Such a test, if the model is correct, should only distribute the total $k$ differently between resolved- and modeled- $k$.From figure 3.4 and figure 3.8 one can say that the standard SST model reports a too low $k$, since it lies below the LES and the resolved LES are limited by the grid.

The objective for the $P_{SAS}$ term is to reduce the damping when unsteady motion are detected by the momentum equations, so that the models go easier over to unsteady mode. The effect from the $P_{SAS}$ term can be seen through the turbulent viscosity, $\mu_t$, plotted for SAS and SST on line 2 in figure 3.7. $\mu_t$ for SAS is clearly influenced by the $P_{SAS}$ term, it has a lower damping at the whole line. The developers say that this is caused by the von Karman length scale, $L_{vk}$, but this was not verified here. The dissipating effects from the turbulent viscosity for the DES model, are almost of same magnitude as for SST, this is the reason for why DES became only mildly unsteady. The two-phase simulations in chapter 4 was simulated on the latest Fluent version where the SAS model is available. The choice was SAS, since it might be less grid dependent. The Fluent version installed on the cluster had only the DES and LES models available. Since the results from the LES gave fluctuations and a three dimensional solution this model was applied to the simulations preformed on the cluster. In the coming section the LES model

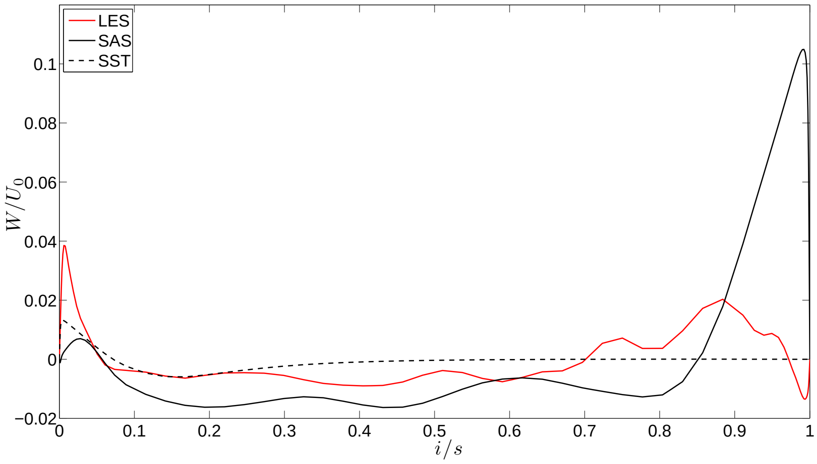

Figure 3.6: Plot of the z-velocity for line 2.

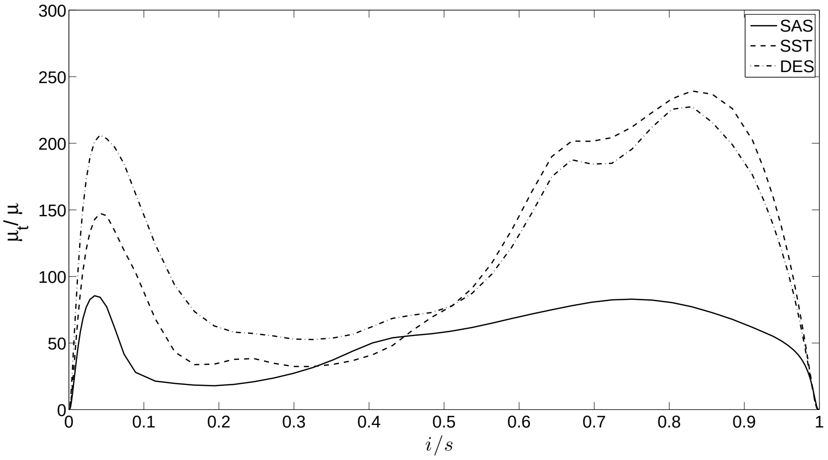

Figure 3.7: The turbulent viscosity ratio.

was tested on two different grids for the reference geometry and geometry 2.

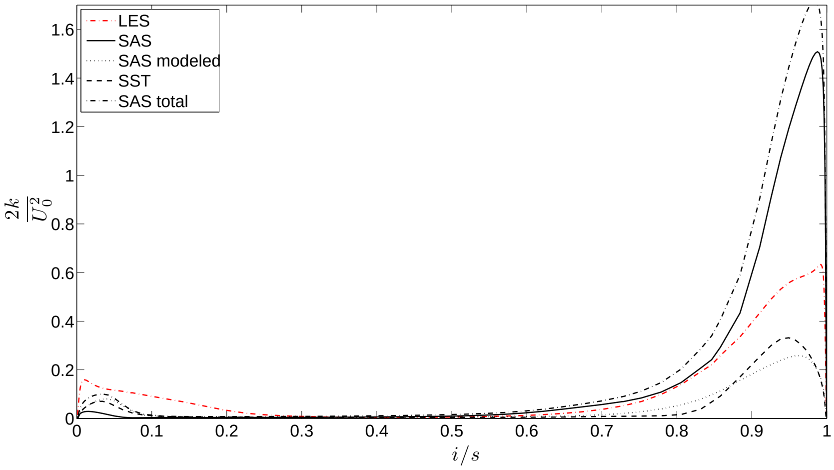

(a) k for line 1

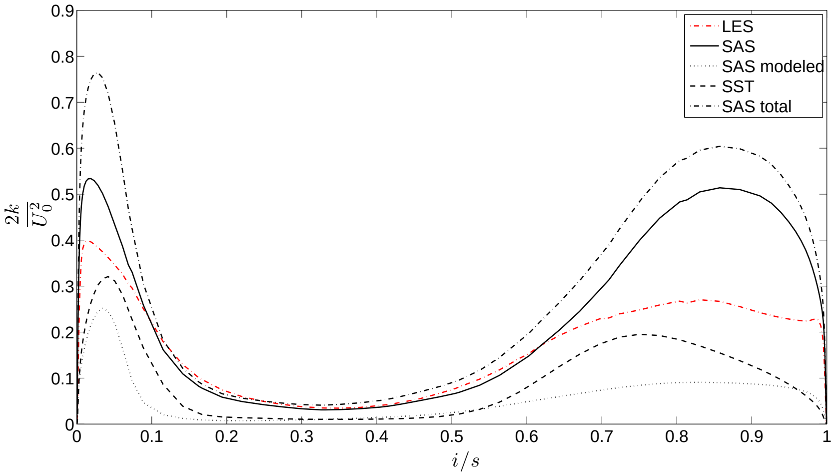

(b) k for line 2

Figure 3.8: Turbulence kinetic energy for three models where SAS has been calculated manually and SAS modeled has been reported by Fluent.

### 3.1.4 Grid dependency of LES

Both geometries were simulated with two grids, one fine and one coarse. The calculations on the fine grid was simulated on a supercomputer named NJORD. It has 59 compute nodes with 8 dual-core power 5+ processors. This project had access to two nodes. The coarse grid was simulated on a desktop computer. The size of the grids are tabulated in table 3.1. All the grids were body-fitted, see appendix A. The simulations were performed for a $k = 0.28m/s$. The boundary conditions are the same as for the LES for the simplified geometry. The lines for both geometries are placed on top of each bend, shown in figure 3.9. Velocities for each line were dumped every time step.

Table 3.1: Different grid sizes tested

| | Grid size $*10^{-6}$ | |
|---|---|---|
| | Cluster | Desktop |
| Reference geometry | 7.0 | 0.6 |
| Geometry 2 | 5.5 | 0.5 |

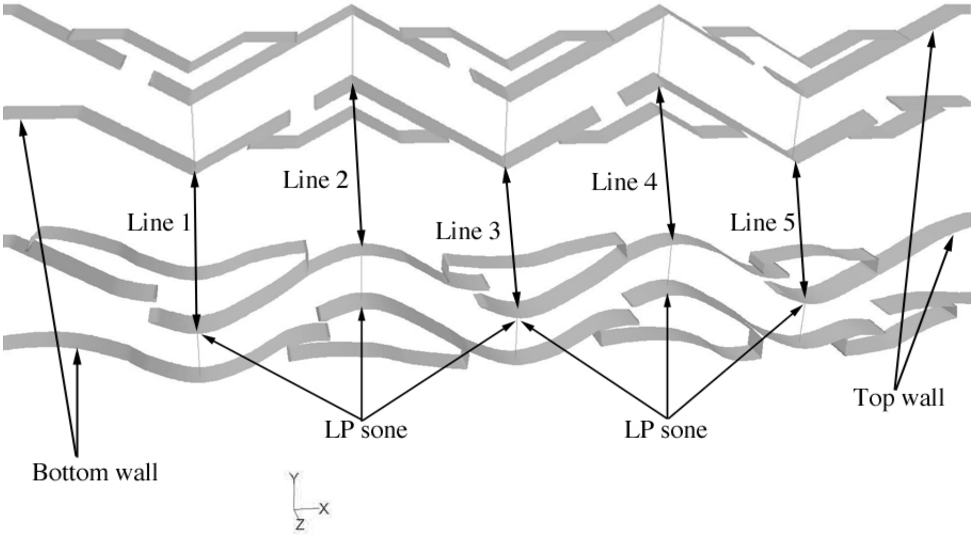

Figure 3.9: Both geometries, with indications of where each line are. Reference geometry at the top and geometry 2 at the bottom.

Average velocity profiles for four different lines has been calculated, shown in figure 3.10. A numerical calculation needs some time steps to become stable, the average quantities have been calculated from this time step. The profiles on line 2, figure 3.10a, have a very similar shape and value. Negative velocities indicates that a re-circulation is present. The re-circulation ends at the same position on line 2, figure 3.10a. Figure 3.10a might indicate that the grid size is acceptable. The fine and the coarse solution becomes more different from each other further downstream. This increasing difference appears most likely because an error is continuously added through the domain, due to the coarse cell size. The high velocity peaks appears in the wall-adjacent cell and is caused by the no-slip condition, due to the fact the wall-adjacent cell is to big.

Figure 3.11 shows the turbulent kinetic energy, $k$, relative to the kinetic energy at the inlet, $\frac{1}{2}U_0^2$. The subscript $()_{fine}$ and $()_{coarse}$ indicates the fine and the coarse grid, respectively. The $k$ profiles for line 2 look similar. This is strange since the grid resolution are very different and the amount of resolved $k$ for a LES is a function of the grid resolution, figure3.11a. This similar behavior might come from the fact that the inlet conditions are affecting this line and that the amount of turbulence generated from the geometry upstream are small. Less turbulence gives bigger structures and then the coarse grid managed to resolve it. The fine- and coarse- solution on Line 3, figure 3.11b, have their highest value in the middle of the channel. $k_{fine}$ has a maximum value of almost 90% of the inlet kinetic energy meaning that this part is highly turbulent. $k_{coarse}$ has a maximum of 60%. Figures 3.11c and 3.11d shows that almost the whole cross section has reached a very high level of $k_{fine}$. The difference between $k_{fine}$ and $k_{coarse}$ has grown, and the coarse grid poorly resolves turbulence. The fine grid resolves much smaller structures than the coarse grid, this is clearly seen in figure 3.12.

The pressure loss over the vanepacks was reported experimentally and by CFD. The up- and down- stream channel of the vanepack have a hydraulic diameter of $D_h = 0.1575m$. To ensure good measurements the pressure taps were placed $2D_h$ upstream- and $4D_h$ downstream- the vanepack. The pressure loss for the two geometries was taken from three different runs and each run lasted for approximately 15 minutes. The reported pressure in the lab is the static pressure loss and the pressure loss reported from the CFD calculations it is the total pressure loss. The inlet- and outlet- velocity in the laboratory were assumed equal, which means that the dynamic pressure loss could be neglected. This

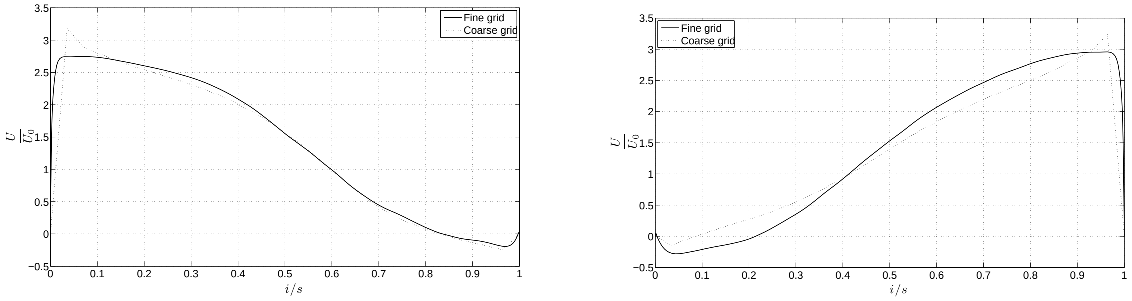

(a) Line 2

(b) Line 3

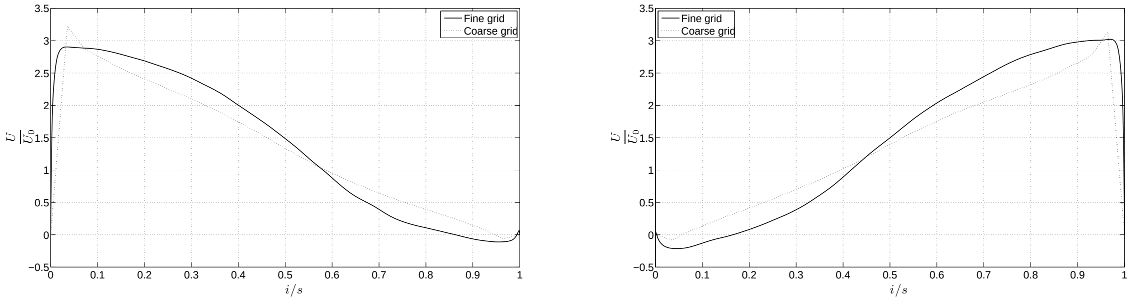

(c) Line 4

(d) Line 5

Figure 3.10: Average velocity profiles for different positions in the domain

assumption allows one to compare the results in the lab and in the CFD, tabulated in table 3.2. Carlson and Talseth (2008) predicted the pressure loss over the vane packs by the use of the standard SST model. Comparing the results for both geometries, the CFD calculations give a very strange result. For geometry 2, geo 2, the fine grid is closer to the measurements than the coarse. This trend seems realistic. For the reference geometry the coarse grid is most similar to experiments. This is very strange. The conclusion can be that correct pressure loss calculations for the reference geometry is difficult to achieve, due to the presence of several re-circulation zones, and that the result for the coarse grid just are a coincidence. A SAS might have given a better solution since it has a more well tested calculation of separated wall-bounded flows.

Table 3.2: Pressure loss in Pascal from experiments and CFD for both geometries.

| | Reference | Geometry 2 |
|---|---|---|
| Experiment | 188 | 134 |
| CFD, fine grid | 417 | 180 |
| CFD, coarse grid | 266 | 213 |
| Carlson and Talseth (2008) | 642 | 245 |

### 3.1.5 Summary

The SST model and the DES model resolved almost no fluctuations, due too a high dissipation from the turbulent viscosity. The instantaneously velocity profiles showed that DES utilize to much CPU time to get unstable and it is not a good choice for this domain, unless one makes a grid more suitable to use with DES. SAS is a modified SST model and by adding the scale adaptive term to the $\omega$ equation, it solves almost the same order of unsteady motions as the LES model. A rough estimate of the resolved part of the energy spectra for the SAS can be said to be adjacent to the LES. Since the scale-adaptive term, $P_{SAS}$, in the SAS model is added without disturbing the SST model in the boundary layer, one can assume that this is a model well suited for transient simulations of a wall bounded flow. The amount of modeling in a LES is set by the mesh size, and since the LES cut-off should be placed in the inertia range, the mesh for such a simulation is difficult to generated. One can also assume that since the $\omega$ equation is well defined for a boundary layer, the SAS model will be more "safe" to use on different grids.

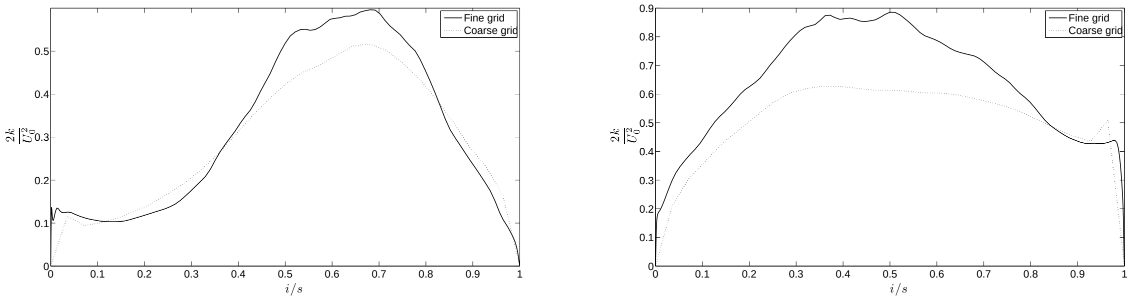

(a) Line 2 (b) Line 3

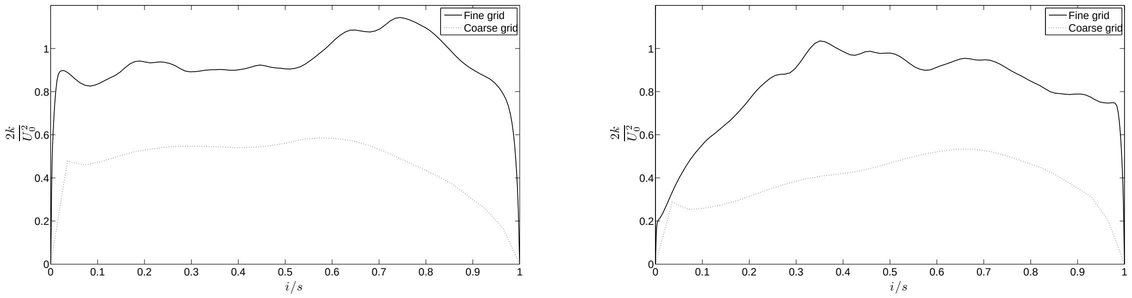

(c) Line 4 (d) Line 5

Figure 3.11: Turbulent kinetic energy divided by the inlet kinetic energy

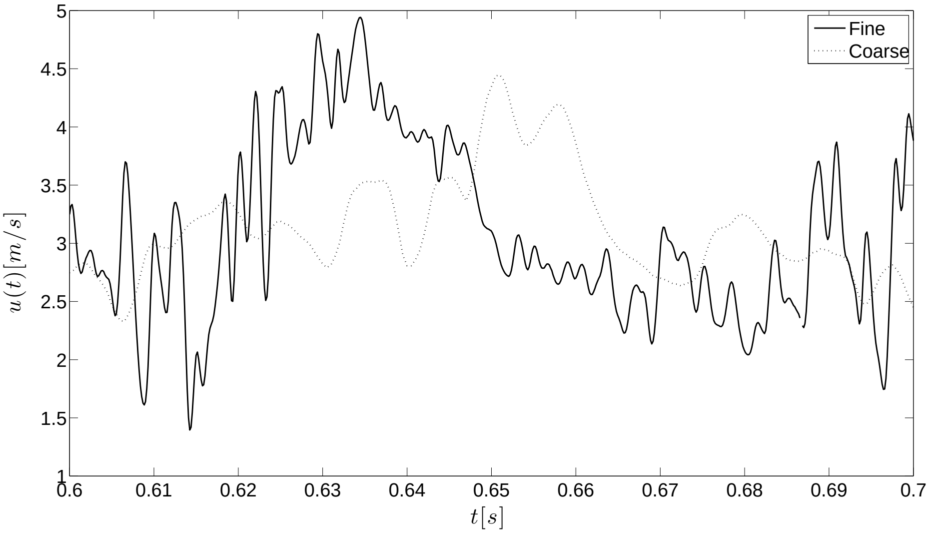

Figure 3.12: Instantaneously velocity for $\frac{i}{s} = 0.96$ on line 5

A coarse LES can give acceptable velocity profiles, but structures are poorly resolved. The pressure losses measured in the lab are assumed most correct, and is really difficult to calculate with CFD, both LES and RANS had a large error. In this section the trend between fine and coarse grids calculations of the pressure loss were unnatural.

## 3.2 Comparing geometry 2 with the reference

In this section, one-phase simulations are coupled with two-phase theory. If a film is generated on the walls, the ideal case would be to ensure that it stays there until it flows into a drainage chamber. The phenomenon of re-entrainment is when liquid gets shredded of a film and will therefore work against the ideal case. A minimum criteria for re-entrainment is that the film surface is wavy. The Kelvin-Helmholtz instability sets the criteria for when the surface becomes wavy (Kolev, 2005). Conclusions are drawn from average velocity and turbulent intensity. The Kelvin-Helmholtz criteria has been calculated with, $\rho_g = 55\frac{kg}{m^3}$, $\rho_l = 775\frac{kg}{m^3}$, $\sigma = 0.0253\frac{N}{m}$.

Figure 3.13 shows the average velocity, $U$, relative to the inlet velocity, $U_0$. The purpose of geo 2 was to remove re-circulation zones, all the plots in figure 3.13 indicate that this has been achieved. Another difference that can be seen is that the average velocity is more evenly distributed in the cross section, although the channel area is smaller. A smaller cross section can be beneficial regarding separation, since a droplet then has a shorter distance to a wall. The maximum velocities for the ref are seen at the low pressure zones on each bend. If a film is present close to a wall, high velocities can cause earlier onset of re-entrainment.

Figure 3.18 shows a photo of the mist flow inside geo 2, flowing from right to left. The arrow numbered 1 in the figure shows the HP zone of bend 2, from the picture it is not clear that there is a film, but it was observed with the naked eye. If this film is wavy, re-entrainment can occur, the plots in figure 3.14 have been made relative to the Kelvin-Helmholtz instability. So if $\frac{U}{U_{g,cr}} > 1$ a wave on a film can occur and thereby re-entrainment will happen. Since the reference geometry has re-circulation zones at the HP zones one can assume that re-entraiment of the film has happened upstream. For this reason ref has not been included in the HP plots, figure 3.14b and 3.14d. Geo2 has possibilities of getting wavy growth at the HP zones, if the film thickness, $\delta_f$ is high enough. For the HP zones the critical thickness for are $\delta_{f,geo2,line2,HP} = 150\mu m$ and for $\delta_{f,geo2,line3,HP} = 125\mu m$. For the LP zones the critical film thickness are approximately $20\mu m$ for both geometries. It has to be mentioned that this is a one-phase simulation and if a second phase was present at the wall the velocity profiles would have looked differently. Velocity profiles adjacent to a wall are typically linear and probably also linear for a film but with a smaller gradient, due to the higher viscosity. This implies that the critical re-entrainment film thickness calculated above can be said to be the absolute minimum. At some test points in the experiment we could observe a wavy film, especially at moderate k and high liquid load.

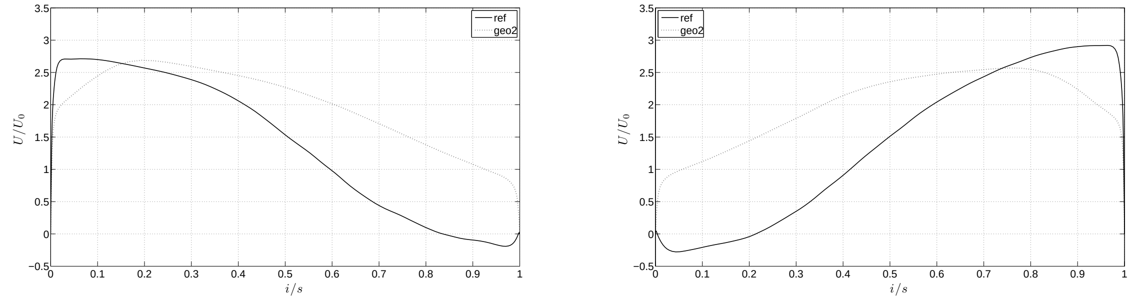

(a) Line 2

(b) Line 3

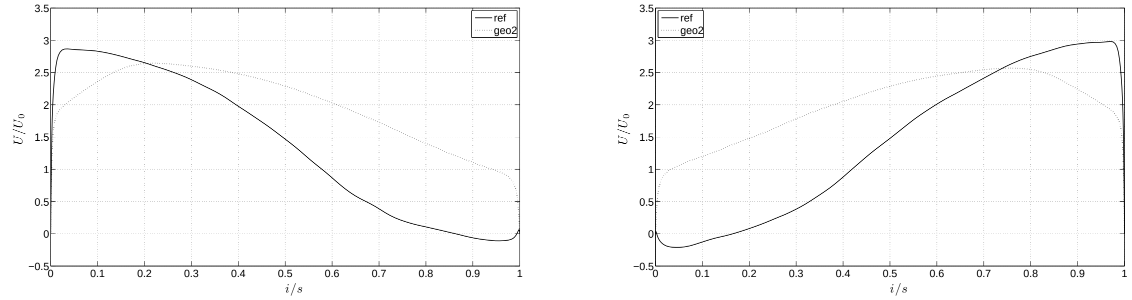

(c) Line 4

(d) Line 5

Figure 3.13: Average velocity relative to the Kelvin-Helmholtz instability

The strategy in (Carlson and Talseth, 2008) was to create a new design with later onset of re-entrainment, by lowering the turbulent intensity, this was done through RANS simulations. The turbulence intensity, $I_{turb}$, for five lines is plotted in figure 3.15, calcu-

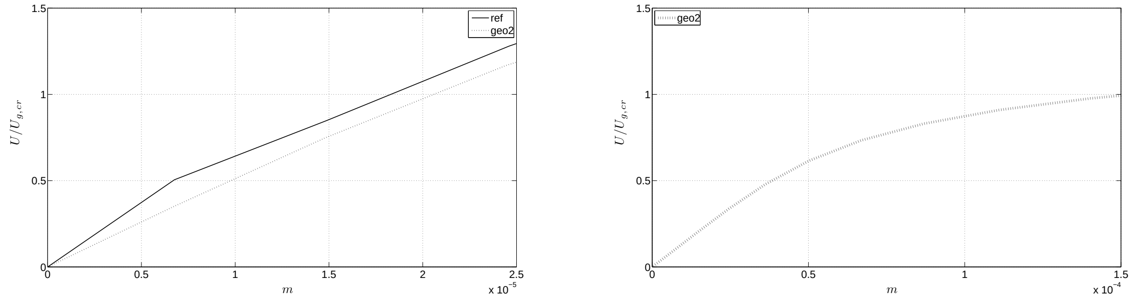

(a) Line 2 LP (b) Line 2 HP

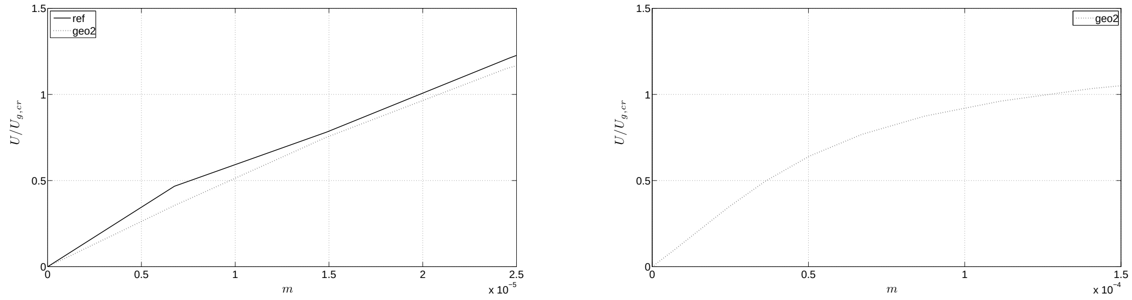

(c) Line 3 LP (d) Line 3 HP

Figure 3.14: Distance from the wall

lated from LES in this thesis. The y-axes are calculated from turbulent kinetic energy as $I_{turb} = \frac{u'_i}{U_i} = \frac{\sqrt{\frac{1}{3}k}}{\sqrt{U^2+V^2+W^2}}$. $U_i$ is the area weighted average for each geometry. Turbulent intensities above 10% is assumed high (Ansys, 2009). The effects of re-entrainment from

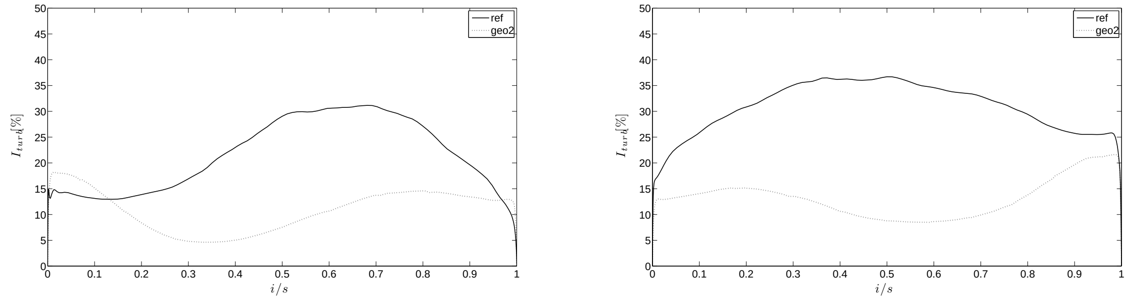

(a) Line 2

(b) Line 3

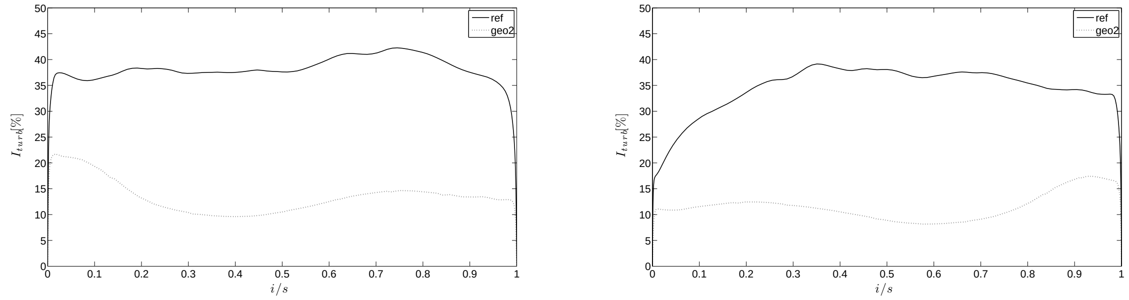

(c) Line 4

(d) Line 5

Figure 3.15: Turbulent intensity, $I_{turb}$, for the two geometries

a liquid film is negative for the separation efficiency. Re-entrainment rate is connected to the turbulence intensity, the higher intensity the more re-entrainment. In addition, turbulence induced fragmentation of a droplet is coupled with the maximum peaks of the fluctuations, due to the fact that such peaks increase the relative velocity between the gas and the droplet, and thereby the Weber number of the droplet, see equation 2.44. Figure 3.15a shows the intensity for line 2, geo 2 has a sligtly higher intensity close to the walls. For the other lines, figure 3.15b,3.15c and 3.15d geo 2 have a noticeably lower profile across the whole channel. Figure 3.16 illustrates the reduced $I_{turb}$ in geo 2 by a vorticity plot. As mention a lower $I_{turb}$ can decrease re-entrainment and turbulence induced fragmentation.

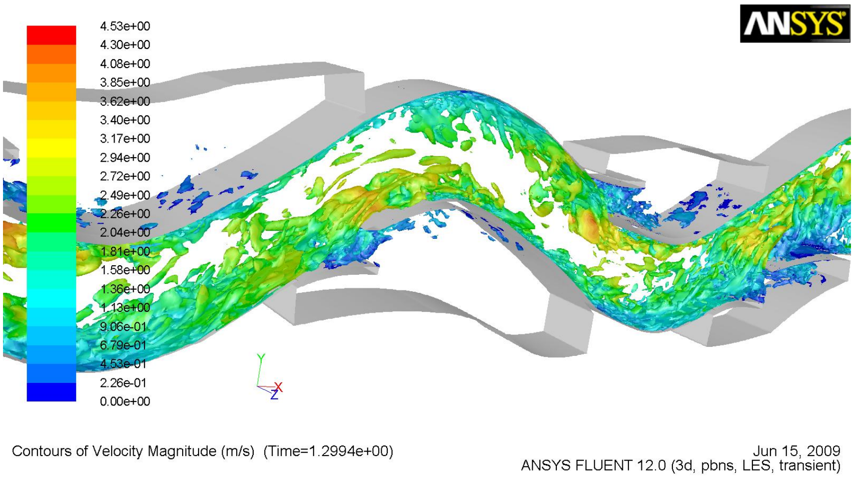

(a) Geometry 2

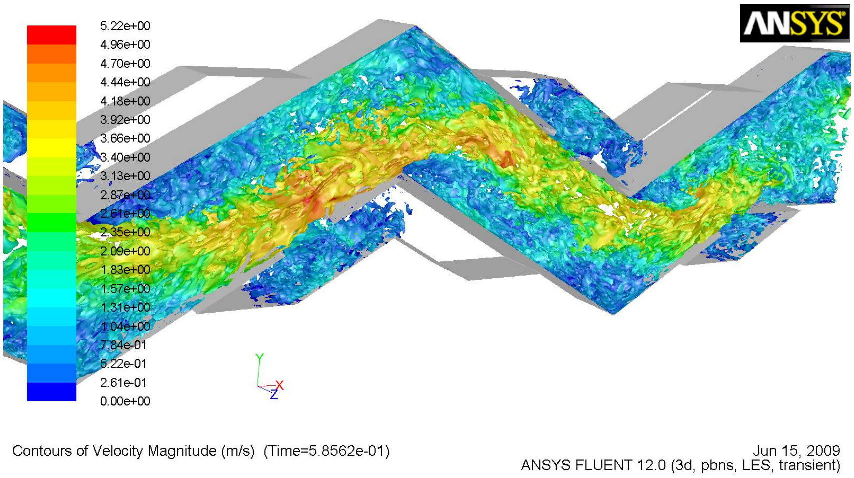

(b) Reference geometry

Figure 3.16: Vorticity contours at 1500 1/s, colored by velocity magnitude.

## 3.3 Phenomena noticed in the laboratory

A phenomenon noticed in the lab was that the mist flow that had been lead into a drainage chamber turned and went out of the chamber, named backflow. The original design of geo 2, designed in (Carlson and Talseth, 2008) had a different drainage chamber and it was not possible to orient the vane pack vertically. The RANS simulations did not show this back flow on the original design, a LES might have. The possibility to orient the vane pack both vertical and horizontal became available if we designed the drainage chambers differently. This re-design was made quickly because the production had to start, a coarse LES was performed without any clear backflow. However when a clear backflow was noticed in the lab this was a big set back. Figure 3.17a shows a photo taken with a digital camera with shutter speed of $\frac{1}{200} = 0.005 sec$. The droplets can be seen as white dots. They give an indication of the flow pattern. The arrow indicated with number 1 in figure 3.17a, shows the backflow. This phenomenon was clearly seen with the naked eye and was reproduced in CFD, see figure 3.17b. The backflow is not a positive feature of this geometry regarding separation. Arrow 2 in figure 3.17 shows a turbulent vortex, this structure was not re-produced in our CFD simulations.

A re-circulating bubble inside the drainage chamber was seen in laboratory and in the CFD, shown in figure 3.19. Figure 3.19a is 10 frames from a movie, the frames have been made partly transparent so that the re-circulation bubble becomes a bit clearer. The movie was taken with 1200 frames per second. As can be seen from the CFD, figure 3.19b, vectors are also directed in and out of the chamber. A force balance between these two velocity differences, might have an effect on wheter a droplet becomes separated or not.

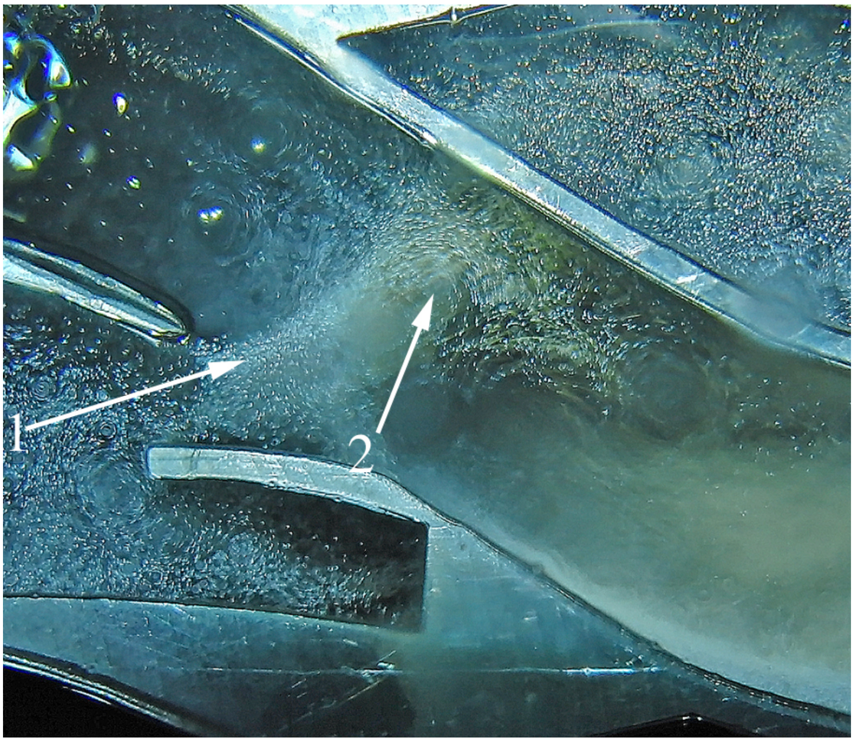

(a) Photo from the lab

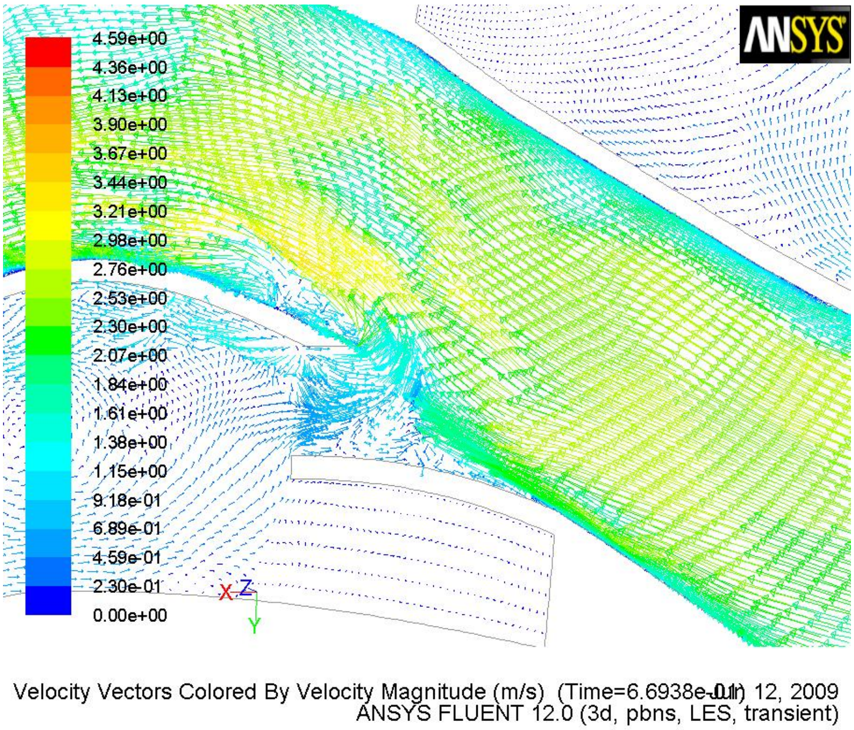

(b) Picture from CFD

Figure 3.17: The phenomena of back flow from the chambers

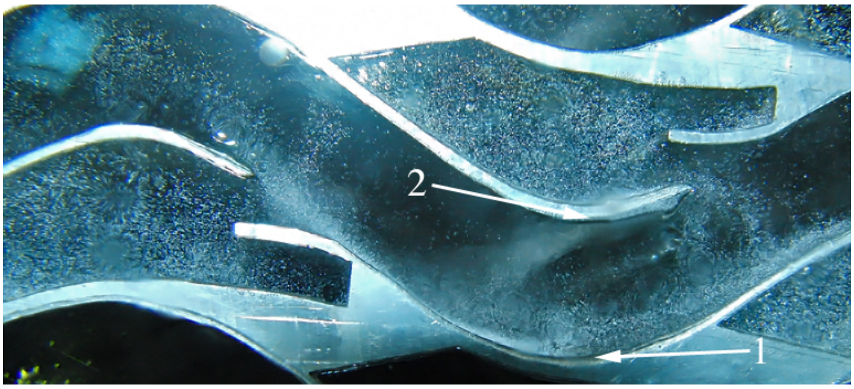

Figure 3.18: Photo of the mist flow inside geometry 2

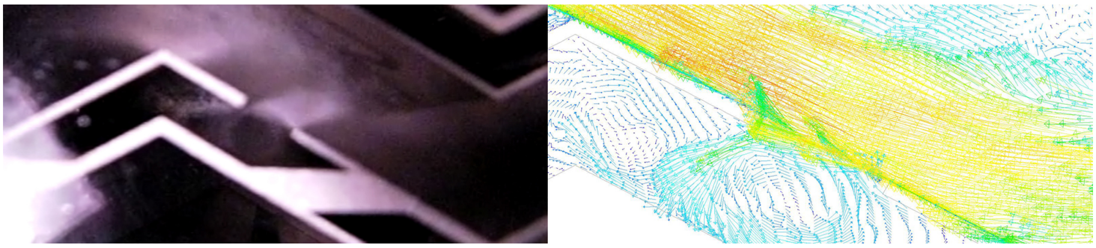

(a) Photo from the lab

(b) Picture from CFD

Figure 3.19: The re-circulation bubble inside the drainage chamber

# Chapter 4

# Two phase simulation

A transient two phase simulation of the reference geometry and geometry 2 could give useful information about the droplet behaviour in the vane pack. The results of the simulations could be compared with experiments, both visual observations and measured efficiencies.

## 4.1 Nummerical setup

A DPM simulation with the use of the fragmentation-, coalescence- and wall-film-model, described in section 2.7 was the chosen approach. This could give more physical realistic results than done by Carlson and Talseth (2008).

As described in section 3.1.3 the chosen turbulence model for the two phase simulation was the SAS model. The grid was built with the same properties as in section 3.1.2, giving a total of 1 599 380 grid cells. Boundary conditions and initial conditions for the continuum were also set in the same manner.

Figure 4.1 shows the domain for the two phase simulation of the reference geometry, with a flow direction from the left- to the right-hand side. Boundary conditions for the discrete phase have to be defined at each physical boundary. Inlet and outlet was defined with the "escape" condition, which terminates the trajectory and reports the droplets as escaped. The drainage chambers, indicated as red surfaces in figure 4.1, were set to the "trapped" condition which is similar to the "escape" condition, but reports the droplets as trapped. The wall-film model, described in section 2.7, was defined on the upper and

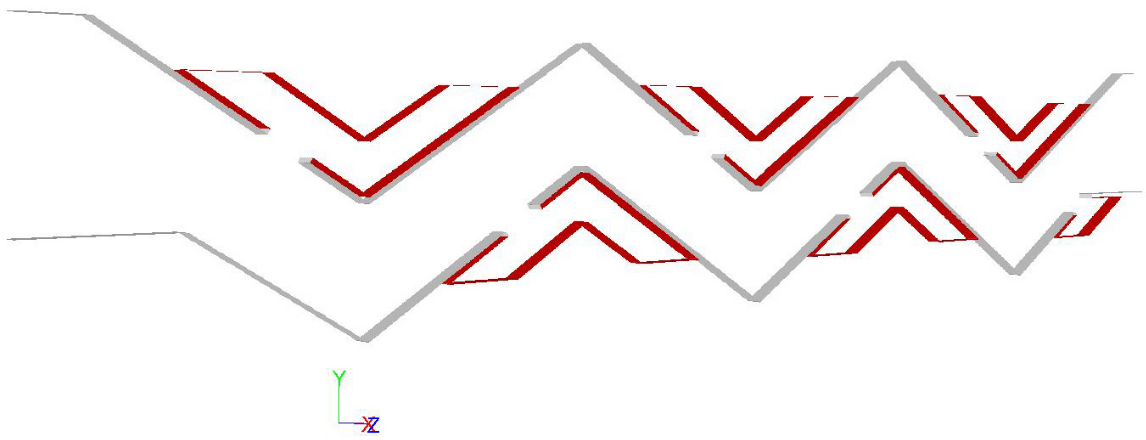

Figure 4.1: The domain for the two phase simulation of the reference geometry

lower wall, indicated as grey surfaces in figure 4.1. Periodic conditions at the boundaries in the z-direction will affect the discrete phase in the same manner as the continuum phase.

There are a number of ways of injecting liquid droplets, please refer to Ansys (2009) for a full presentation. The chosen approach was to import a droplet profile through a text file, with information about coordinates and velocity in all direction, temperature, diameter, mass and name of each droplet. To achieve full control over the diameter distribution, spread and liquid flow rate a code was written in Visual Basic, see appenix E. The code was programmed to give a Rosin Rammler diameter distributed and randomly spread droplets over a given surface based on the following input parameters:

- Coordinates of the surface for the droplet injection.
- The droplet velocity in each direction.
- The initial droplet temperature.
- Maximum, minimum and mean droplet diameter.
- The liquid flow rate and the chosen time-step for the simulation.

To define the particles as droplets one has to enable the energy equation and chemical species. Mixing, transport and chemical reactions is modeled in Fluent by species transport and finite-rate chemistry. The mass transfer between oil and gas, or between the phases in the laboratory has not had any focus in this thesis. All transport and chemical reaction were therefore neglected.

Parallel processing was not possible due to stability problems in the DPM solver in the current Fluent version. The simulation were performed on a 3GHz Intel Xeon processor with 6 Gb RAM and Microsoft Windows XP 64bit operating system.

## 4.2 Results of two phase simulation

A DPM simulation of the reference geometry and geometry 2 were performed. The strategy was to simulate the reference geometry first and geometry 2 afterwards. The objects for the simulation was to study the performance of a transient DPM simulation, in addition to the study of the droplet behavior in a vane pack. Carlson and Talseth (2008) studied the reference geometry and geometry 2 with a steady DPM simulations, different sized droplets were injected and calculated through the domain. The simulation gave interesting results, but a transient simulation with a better performing turbulence model could give additional information.

### 4.2.1 Time consumption of two phase simulation

The reference geometry was simulated first and it was rather time consuming. The gas phase was stabilized after about 2500 time steps with a convergence criteria of $10^{-6}$. Droplets were then injected and to assure a stabilized DPM distributoin in the domain it was calculated for about 4000 time-steps before the sampling started. Due to the large amount of simulated droplets and the required convergence criteria for the DPM solver, each time-step calculation took about 30 $min$. This means that the first simulation lasted approximately 80 days, before the sampling could start. Of this reason, geometry 2 was simulated on a much coarser grid and thereby a larger time step. It would have been of great interest to run the simulations on the Njord cluster, but this was not possible. The Fluent version on the cluster had an older version, with a slower and more unstable DPM solver. It would also been troublesome to post process pictures of the simulation on the the cluster.

### 4.2.2 Reference geometry

Carlson and Talseth (2008) used the steady DPM in Fluent, with and without the discrete random walk model enabled, to investigate the separation trend between ref and geo2.

The properties of the simulation after approximately 7000 time steps is presented in table 4.1. The result of the reference geometry has the main focus since it is simulated on a finer grid and a smaller time step.

Absolute values from the simulation are not trustworthy, because no experimental data of the droplet distribution and behavior outside the visual observation was available. The diameter of the injected droplets were accommodated to the stated diameter distribution for the nozzles which were used in the experiments, but this distribution was not validated with the used fluid and operational condition. The used two phase model is neither validated, and it is not likely on the authors opinion that the model can reproduce the complexity of a highly turbulent two phase flow. The model could however show many interesting trends of the droplet flow, and it is far more complex than the model used by Carlson and Talseth (2008).

Table 4.1: Properties fro the transient DPM simulation

| Property | Value |
|---|---|
| $\rho_g$ | $55[kg/m^3]$ |
| $\rho_d$ | $775[kg/m^3]$ |
| $\sigma$ | $0.0253[N/m]$ |
| Averaged number of droplets over the sampling period. | 85000 |

Samplings of the simulation were taken from surfaces that fill the vane pack cross section at each bend, illustrated as red surfaces in figure 4.2, and at the inlet- and outlet surface, illustrated as blue surfaces in figure 4.2. The surfaces at the bends are called planes with the suffix 1,2,3,4 or 5, based on the placing from left to right respectively. The samplings were taken over a period of 450 time steps, which corresponds to $0.00675s$ with the chosen time step length. This is a very short period and it can not be stated that this is a sufficient period to assure better statistical values. Due to the lack of time was it unfortunately not possible with a longer sampling period.

The transient behavior of coalescence can be seen from the ratio of coalesced droplets

Figure 4.2: Illustration of the sampling surfaces

over the sampling period, figure 4.3. There are assumable some coalescing activity in the droplet injection area, and this can not be ascribed to the vane pack geometry, because it is more likely a consequence of a balancing behavior of the droplets after the injection.

The ratio of the fragmented droplets over the sampling period is shown in figure 4.4a.

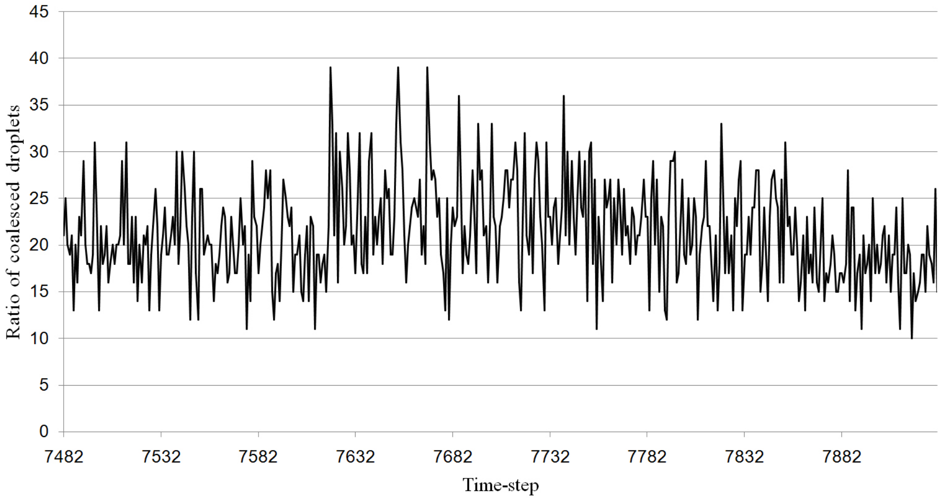

Figure 4.3: Transient behavior of the simulation, illustrated by the ratio of coalesced droplets

The fragmentation ratio is much smaller than the coalescing ratio, and is zero over parts of the sampling period. The critical Weber number, $We_{d,\infty}$, is as mentioned typically set to 12. A picture of the droplets colored by $We_d$ at bend 2 are shown in figure 4.4b. The interval of $We_d$ which the droplets are colored by, is limited from 0 to 12, and means that droplets that have a larger value are colored red. The picture shows clearly that only a few droplets have a $We_d$ larger or close to 12. This implies that only a few droplets are close or above the critical value which impose fragmentation. At the inlet of the drainage chambers there are groups of droplets with a higher $We_d$ than the droplets in the mean flow, and this could most likely be because droplets with a relative high inertia comes into an almost stagnated area. After each bend there can be seen areas with higher $We_d$, this might be because the velocity of the gas is higher after each bend which implies a higher velocity difference between the gas and the droplets. The values of $We_d$ supports the choice for the TAB-model for droplet fragmentation.

The liquid volume fraction in this simulation is approximately 0.5%, and is therefore

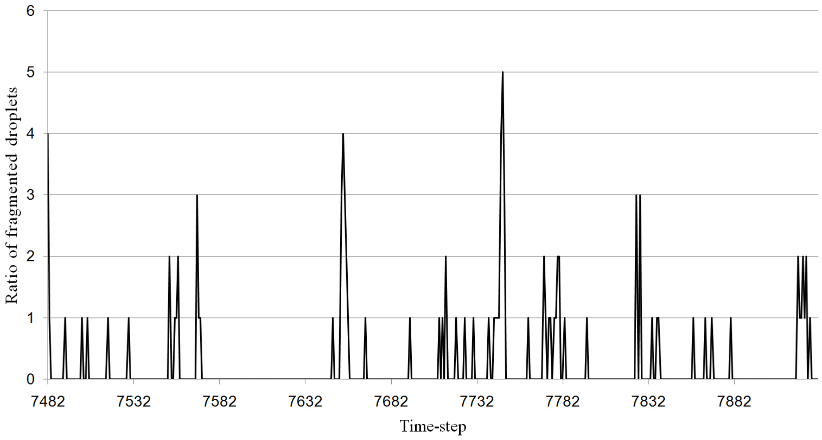

(a) Ratio of fragmented droplets

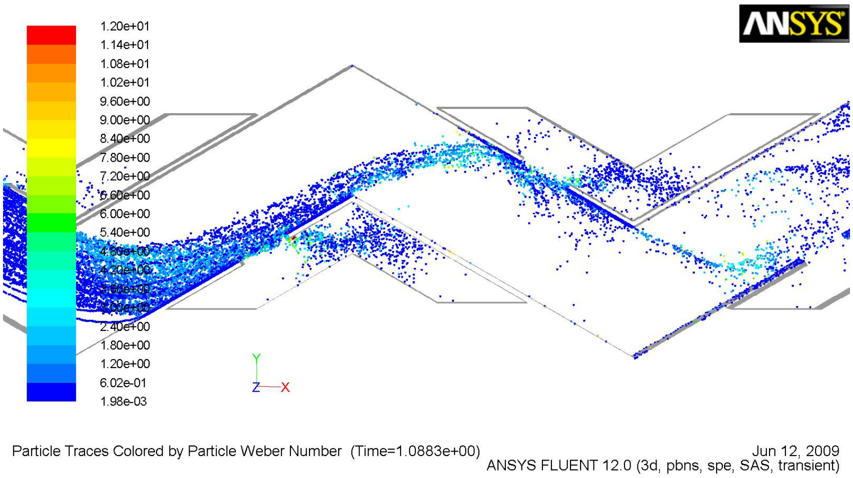

Particle Traces Colored by Particle Weber Number (Time=1.0883e+00) Jun 12, 2009
ANSYS FLUENT 12.0 (3d, pbns, spe, SAS, transient)

(b) $We_d$ of the droplets at bend 3

Figure 4.4: The fragmentation ratio and $We_d$ of the droplets.

higher than under the experiments in the laboratory. This was because the simulation was started before the test matrix for the experiments was stated, and means that there is no experimental data to validate the separation efficiency. The separation efficiency over the sampling period is calculated to 99.8%. Compared to the experimetal results, this seems unaturally high. At $p = 8barg$, $k = 0.25$ and $\alpha_l = 0.15\%$ the reference geometry has a measured seperation efficiency of 94.5%, please refer to section 6.2. The experimental results shows that the separation efficiency increase at increasing $\alpha_l$, but this is not likely the reason for the high separation efficiency calculated from the simulation. The reason for the high separation efficiency is more likely because of the limitation of the wall-film model. The wall-film model, which is used in this simulation, is designed for a mixture process in a port fuel injected engine, described in subsection 2.7.3. This means that the model is designed for droplets that impinges on a wall with a high inertia and thereby splash on the film surface or subsequently evaporates. On the other hand, in a vanepack it is mainly re-entrainment from a vavy film (Verlaan, 1991), or re-entrainment from bends and slits (Swanborn, 1988) that takes place, which the model is poorly designed for. No droplets were reported as splashed under the simulation. The liquid film is a boundary condition and has therefore no 3-dimensonality and is only present at the wall, even if the film height is reported higher than the wall adjecent cell. Some re-entrainment from bends and slits can however be genrated by defining an optional angle where the liquid film will separate from the wall. This angle has been set to $30^o$ in the reference geometry simulation. It is not possible to sample the re-entrainment flowrate. Figure 4.5 shows the simulated film height on the wall. The model is only valid for film heights less than $500\mu m$ and this is clearly exceeded under the simulation, especially on the wall around the slit on the second bend. A liquid film was observated by the naked eye under the experiments at the same locations as figure 4.5 indicates, but the height of the liquid film can not be validated. The wall-film model is still the best alternative from Fluent to simulate a liquid film in DPM simulations in the present version.

Each droplet that crossed one of the sampling surfaces was reported, with information about the location, velocity, mass, diameter and temperature. A plot of the diameter distribution at each surface could then be plotted, to see if the diameter distribution is changed though the geometry. Figure 4.6 shows the relative diameter distribution at each sampling surface. The droplet diameter is classified in intervals with a size of $25\mu m$. The result shows that droplet diameter distribution is narrowing through the domain, with smaller and smaller droplets passing through. Very few droplets with $D > 100$ leaves the

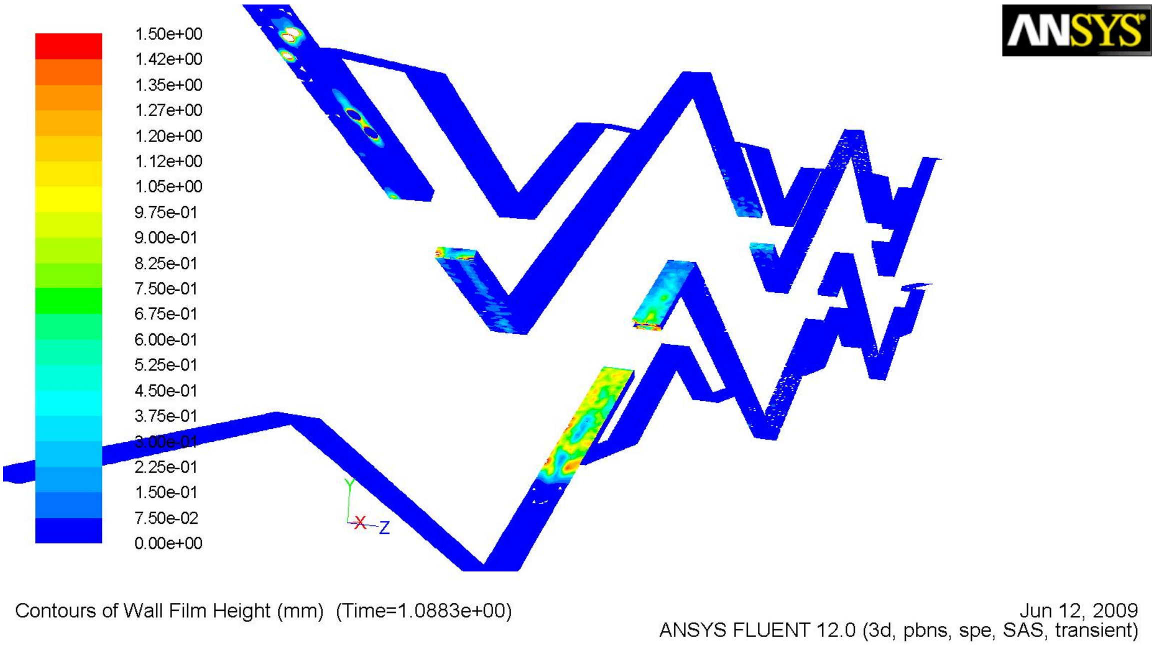

Figure 4.5: Contours of the wall film height.

vane pack. This is in agreement with the steady DPM simulations that were presented in Carlson and Talseth (2008), where the reference geometry has a cut off at approximately $D > 100\mu m$. This shows that a steady DPM simulation has the same capability to predict the diameter cut off for a vane pack geometry as a transient simulation.

### 4.2.3 Geometry 2

As already mentioned the two phase simulation of geometry 2 was performed with a larger time step on a much coarser grid, due to lack of time. The grid had a size of 383 142 grid cells. The coarse grid did not resolve the structures of the continuum adequately which resulted in a poor prediction of the droplet behavior. The fragmentation and coalescence model are dependent of a sufficiently small time step, and this was not controlled, and could have led to a time dependent simulation. Figure 4.7 shows two pictures from the simulation, and the droplet trajectories were not in accordance with the observations in the lab. Figure 4.7a shows a close up of bend two, and the simulations showed some similar trend to the one observed in the experiments at this location. The droplets close to the wall upstream the slit on bend two formed a thin stream which was spitted by the downstream opening of the slit.

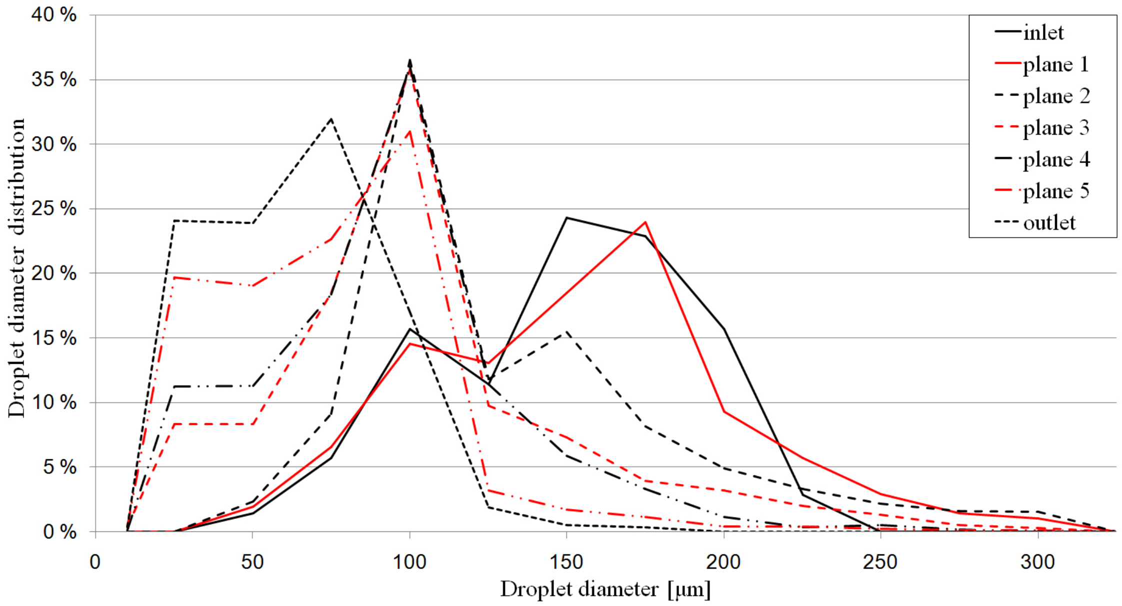

Figure 4.6: Diameter distribution at each sampling surface.

### 4.2.4 Comparisson of observations in the lab and the two phase simulation

Observations of the liquid flow under the reference geometry experiments showed that the droplets had a pulsating behavior. Figure 4.8 shows the chaotic behavior of the injected droplets in the two phase simulation, and indicates the pulsating behavior. The location of the liquid film was also well predicted, even if the film behavior and film height is not trustworthy. Figure 4.9a and 4.9c show two pictures from the simulation at $p = 8bar$ and $k = 0.30$, with $\alpha_l = 0.08\%$ and $\alpha_l = 0.15\%$ respectively. The same trend was shown in the two phase simulation, see figure 4.9b and 4.9d.

### 4.2.5 Summary

The two phase simulations intercepts many interesting phenomena observed under the experiments and shows clearly that it is a useful tool under the designing process, see figure 4.9. Absolute values from the simulation could however not be trusted, due to the many uncertaities in the modeling. The wall film model did not predict the liquid film well. It is important to do the simulation on a sufficient fine grid and small time step to achieve the dynamics in the continuum. A grid- and time- dependency analysis of the simulations would have been interesting, and could minimize the number of required CPU hours.

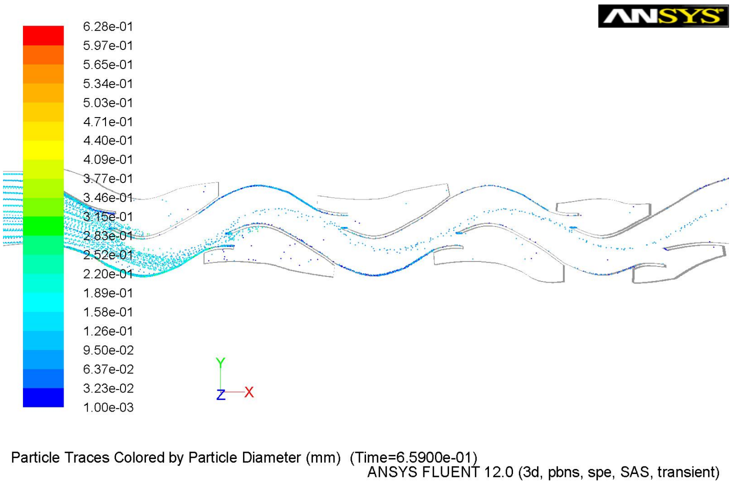

(a) The whole domain.

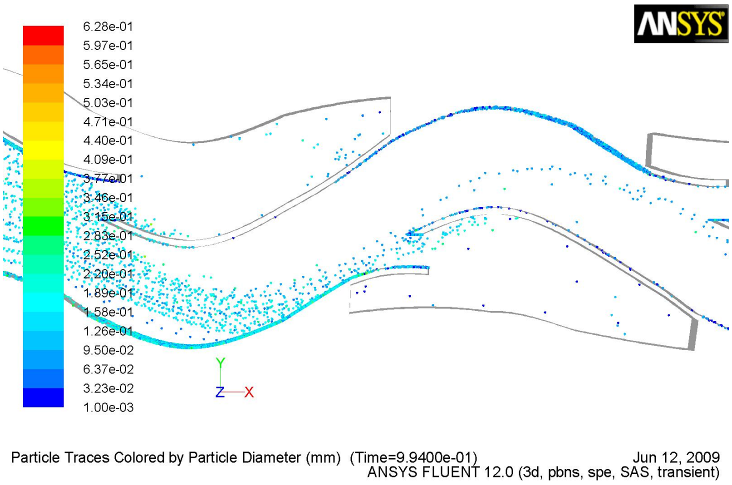

(b) Close up of bend 2

Figure 4.7: Droplet pattern for geometry 2, colored by particle diameter.

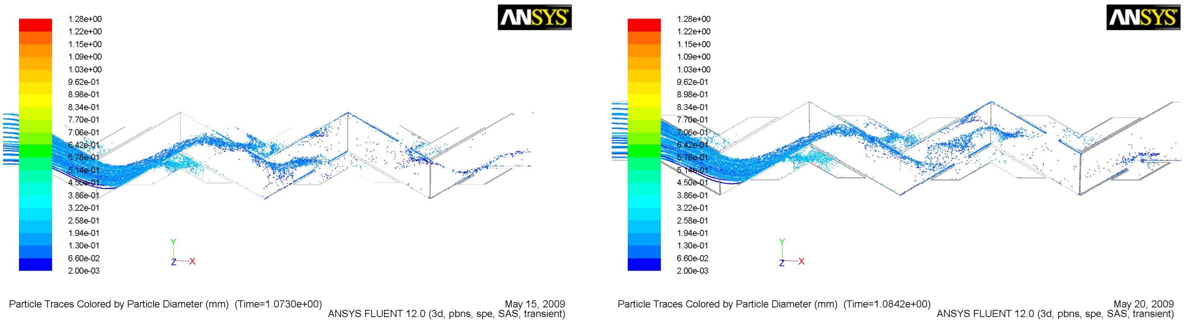

(a) t=1.0730s

(b) t=1.0842s

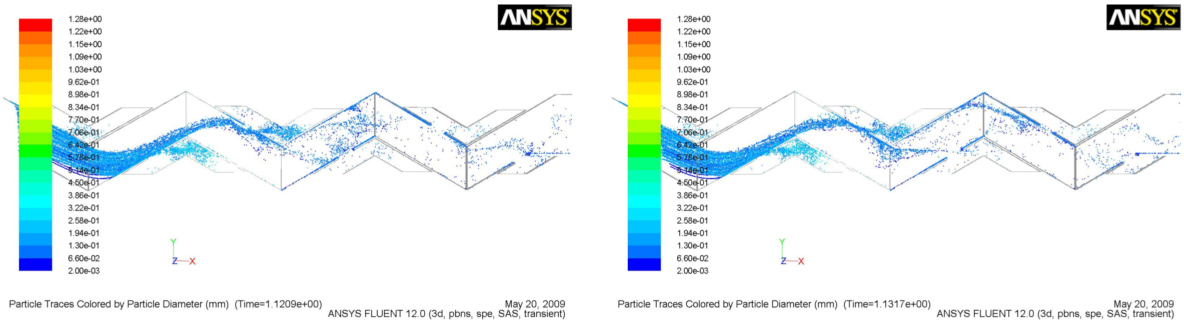

(c) t=1.1209s

(d) t=1.1317s

Figure 4.8: Pulsating behavior of the two phase simulation

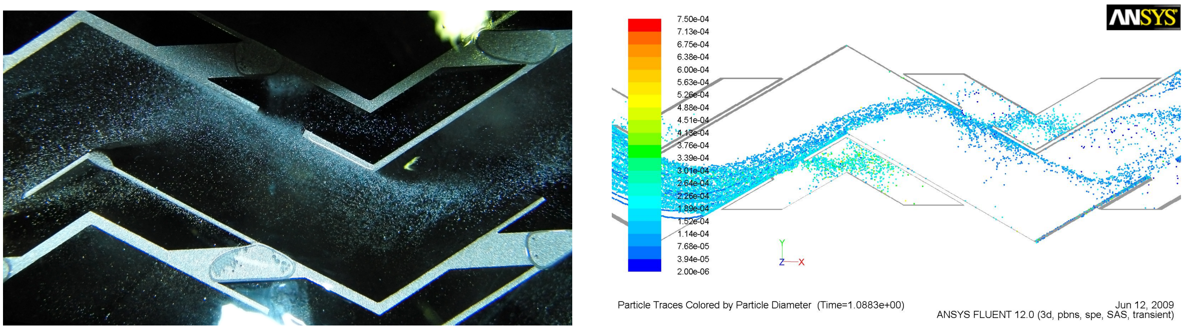

(a) Photo from the experiments (b) Picture from the simulation

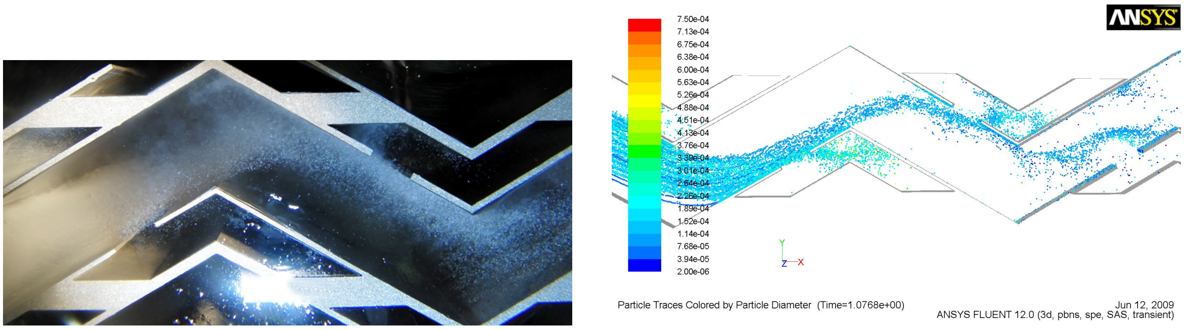

(c) Photo from the experiments (d) Picture the simulation

Figure 4.9: Illustration the similar behavior of the droplets in the experiment and in the two phase simulation

# Chapter 5

# Experimental setup

In order to confirm the CFD simulation and to measure the efficiency of the two different vane pack geometries, experiments are needed. The experimental setup and the test procedure of the test rig is described in Carlson and Talseth (2008). There has been some modification on the test rig to fit a new vessel. The new vessel is designed for testing different horizontally oriented vane pack geometries. The following section will describe these modifications, structural analysis of the test box and the design of the test object.

## 5.1 Test rig modifications

The original loop, described in Carlson and Talseth (2008), was designed to test vertically oriented internals. The chosen approach to test horizontally oriented internals, was to build a new test vessel, called test box, in a parallel loop to the original loop. One of the benefits of this approach, are that the rig became flexible for testing both horizontally and vertically oriented internals without any reconstruction, when it is under operation. The flow sheet of the new test rig is shown in figure 5.1, where the test box is called VG03. The red lines indicates the path for the gas loop, the yellow lines indicates the path for the measuring and draining system, and the blue lines indicates the path for liquid injection. MC1, MC2 and MC3 are the three measuring cups used to measure the efficiency of the test object. The efficiency of the test object is determined by comparing the amount of separated liquid from the test object, MC1, and the separated liquid from the high performance gas/liquid separator, MC2 and MC3. The cost of the modifications have been limited by integrating the new loop into the original loop in such way that most of the old equipment have been utilized, both loops use the same measuring cups, pumps, blower and most of the piping.

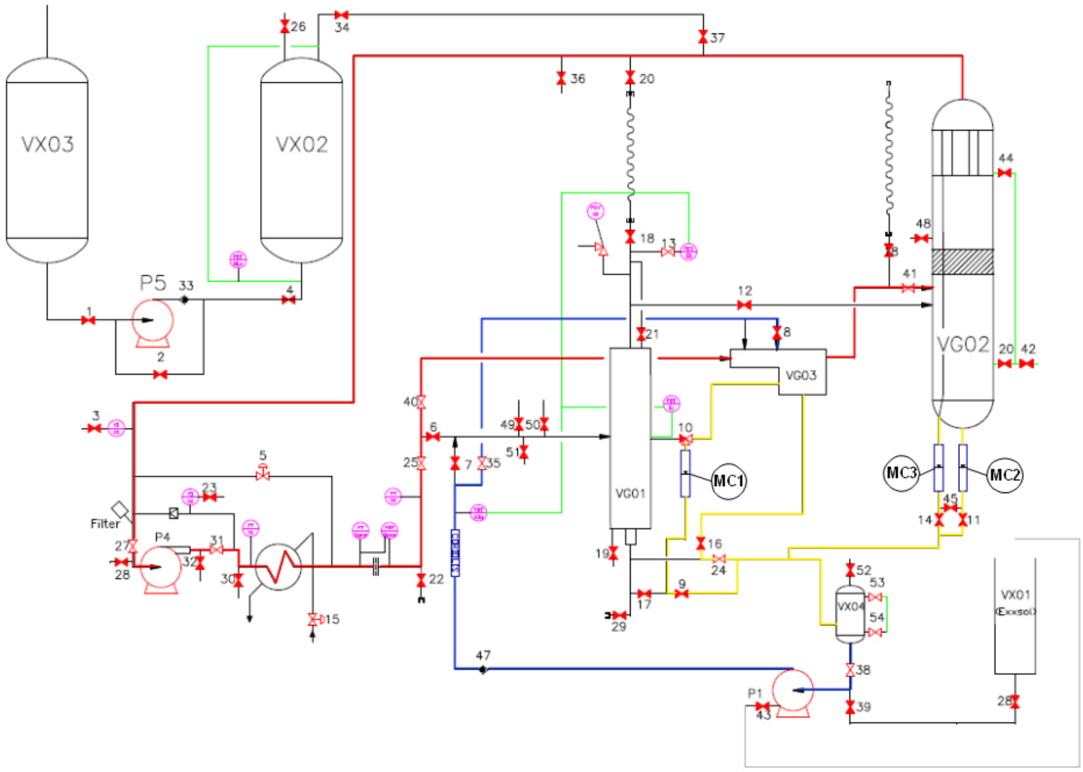

Figure 5.1: Flowsheet of the modified rig.

## 5.2 Test box design

The original design of the test box is presented in Carlson and Talseth (2008). Some modifications are however made to make the test box more flexible for different test objects. The area for the test object is made longer, from 330$mm$ to 383$mm$, so that one can include more bends in the vane pack geometry. Figure 5.2 shows the placing of the test object and the available space for additional bends.

A structural analysis of the box is important to see if it can handle the pressure in the laboratory. An absolute requirement for every objects facing outwards in the flow loop, are that they bear a pressure difference of minimum 15 bar, or in other words, approximately twice the desired operating pressure. The chosen approach was a finite element analysis, FEA, in Solidworks/Cosmoworks 2008.

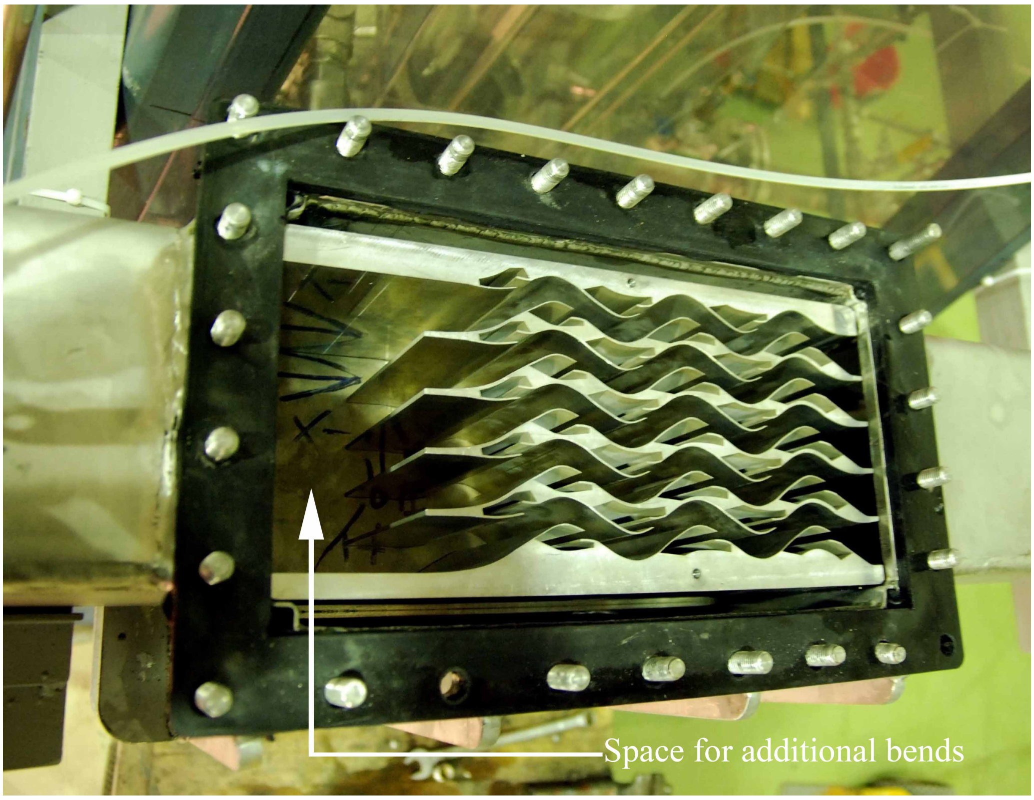

Figure 5.2: Placing of the test object in the test box. Flowing from left to right.

FEA or finite element method, FEM, is a numerical method for solving PDE's as well as integral equations. The fast development of computer hardware and software have made this tool available and usable for desktop computers. 2-D modeling is generally less accurate than 3-D modeling, but less time consuming. The models can insert numerous algorithms, that makes the system behave linearly or non-linearly. Linearly systems are far less complex, and do not account for plastic deformation. Non-linearly on the other hand handles plastic deformation, and one can test the material all the way to fracture, Norrie (1978). The system is divided in elements, 2-D modeling use typically triangle- or quadrilateral- shaped elements and 3-D modeling use typically haxahedral- or tetrahedral- shaped elements. For a tetrahedral element there are usually four vertex nodes or four vertex nodes and six mid-edge nodes Akin (2006). Each node contain structural and material properties which defines how the system react on the loading condition.

The FEA tool in Solidworks/CosmosWorks 2008, includes a five step FEA. This is a useful tool to make a simple structure analysis, and the method consists of the following five steps:

- Choose which type of study that is of interest. E.g. static or dynamic analysis.
- Define which type of material the chosen system consists of.
- Define the attachment points for the system.
- Choose what type of load the system is loaded with, and the placing of the load. E.g. pressure.
- Partitionate the system into elements. The size of the grid is determined by choosing the size of the largest element, and a automated grid function make a grid consisting of tetrahedral elements.

A static analysis of the stresses in the structure caused by the pressure was chosen, and the system was linearly solved. This is satisfying because any stresses beyond the yield strength of the material, which cause plastic deformation, is unacceptable. This is due to the fact that a plastic deformation could lead to leakage in the cover gasket and/or unexpected flow patterns in the box and cause additional measuring error. Two different materials were available from the manufacturer, 316L- and Duplex- stainless steel, and the relevant properties are presented in table 5.1. Stainless steel duplex is a more solid

Table 5.1: Physical properties of the available steel for the test box

| Steel name | Yield strength [MPa] | Tensile strength [Mpa] |
|---|---|---|
| Stainless steel 316L | 301.5 | 623 |
| Stainless steel Duplex | 536 | 775 |

material, but more expensive and the welding is time consuming. Figure 5.3a shows the design of the original box and mesh. The green arrows indicates the chosen fastening points and the mesh has 75378 elements and 144620 nodes.

The result of the stress analysis of the original design, figure 5.4a, shows that the stresses are beyond the yield strength for both types of steel. The largest stresses are located at the side plates of liquid chamber, where the surfaces are largest. Strengthening of these surfaces were required and the chosen approach was to weld $10mm$ wide and $50mm$ high ribs on the surfaces. After some testing, the solution was two ribs each direction all the way around the box, except on the cover, see figure 5.3b. The cover will achieve enough strength through the flange of the see glass. The channel had no need for strengthening, due to relative small heigth of the channel. The mesh was built similar to the one on the original design, and the result of the analysis shows a clear reduction in the stresses in the structure, see figure 5.4b. The largest stresses is approximately $307MPa$ and located at the ribs on the largest surfaces, and it was required that the manufacturer used stainless steel duplex to avoid exceeding the yield strength of the material.

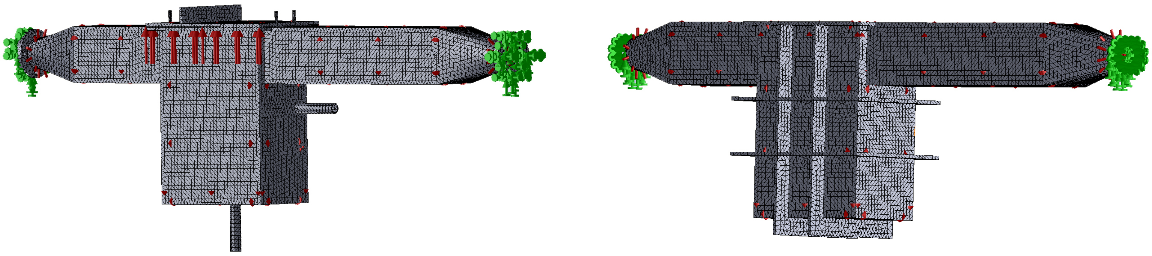
(a) Original design (b) New armoured design

Figure 5.3: Overview of the mesh quality

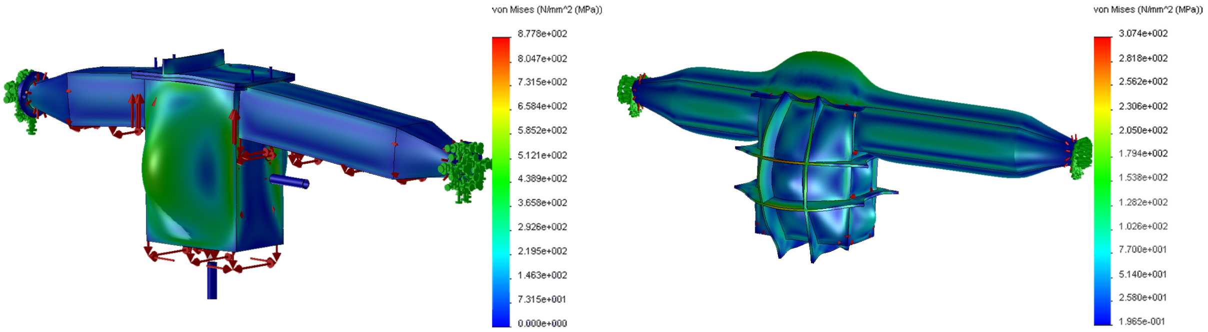

(a) Original design

(b) New armoured design

Figure 5.4: The results of the FEA. Colored by stress in the structure

## 5.3 Placing of liquid nozzle in the test box

A liquid nozzle is placed upstream of the vane pack to inject liquid droplets in the gas flow. The placing of the nozzle, regarding to the vane section, is important to avoid spurious effects. If the nozzle is placed too far away, a major fraction of the liquid can hit the wall before the vane section and if it is placed to close only a part of the vane section will be utilized. A CFD simulation of the channel with the nozzle was executed to determine the placing. The cross-section of the simulated channel is similar to the test box, $158mm\ x\ 157mm$, and the domain has a length of $600mm$. The continuous phase has the same physical properties as the gas used in the laboratory, and the simulation was preformed with the the $k - \epsilon$ turbulence model. The simulations have been executed at three different pressures, at two different k-values and with a medium size nozzle with three different liquid loads given by the pressure difference over the nozzle opening, see table 5.2. The liquid spray from the nozzle has been simulated with the steady state DPM model, with a one-way coupling between the phases. The particles are spread in a cone formation, which agree with data from the manufacturer. The injections have a spread angle of 45 degrees, and an initial velocity and mass transfer given by the manufacturer (BETE Fog Nozzle, 2009). A Rosin-Rammler diameter distribution has been used to simulate a more realistic injection, with a diameter interval from $50\mu m$ to $400\mu m$ and a mean diameter of $175\mu m$. The boundary condition at the channel wall for the particles is the escape condition to better visualize the impact position. The simulations have some clear drawbacks regarding to accuracy, due to the simple turbulence model and DPM injection, but the purpose of the simulation were to show trends of the scattering behavior of the liquid spray at different operating conditions.

Figure 5.5, 5.6, 5.7 and 5.8 shows the results of the simulation, where the green, red, blue and grey colored planes represents $100mm$, $200mm$, $300mm$ and $400mm$ distance from the nozzle opening respectively. At $1.99bara$ and at a k-value of $0.35m/s$, figure 5.5, the scattering of the liquid is unaffected of the gravity for the first $200mm$ and the largest particles impact the wall at approximately $100 - 150mm$ from the nozzle. The effect of liquid loading is small, but higher liquid load tends to increase the scattering due to higher velocity. At $4.96bara$ and a k-value of $0.35m/s$, figure5.6, the biggest particles impact on the wall $150 - 210mm$ from the nozzle. This shows that higher density causes higher drag on the particles and the scattering decreases. At $200mm$ the gravity has a noticeable effect on the particles. At $9.03bara$ and a k-value of $0.35m/s$, figure 5.7, the gravity and the high density of the continuous phase decrease the spread considerably. The largest particles, $225 - 400\mu m$, are almost instantly pulled down, and the largest spread is approximately about $80mm$ from the nozzle. The simulations at the same pressure, but at a k-value of $0.15m/s$, figure 5.8, shows the same tendency as at higher k-values. The result of the simulations shows that the density of the continuous phase together with the effect of the gravity is the most crucial factor for the scattering behavior. Higher density seems to decrease the spread and the gravity pulls down the particles faster. The placing of the nozzle becomes a compromise between largest possible spread and to prevent liquid from floating along the walls. If a considerably part of the liquid floats along the wall it will become a major source of error and a small spread will not utilize the the whole cross section of the vane pack. The conclusion of this simulations were to place the nozzle $100mm$ upstream of the vane pack inlet.

Table 5.2: The different physical properties of the nozzle simulation

| Physical properties | | | |
|---|---|---|---|
| Pressure [bara] | 1.99 | 4.96 | 9.03 |
| k-value [m/s] | 0.15 | 0.35 | |
| $\Delta p$ nozzle [bar] | 1 | 10 | 10 |

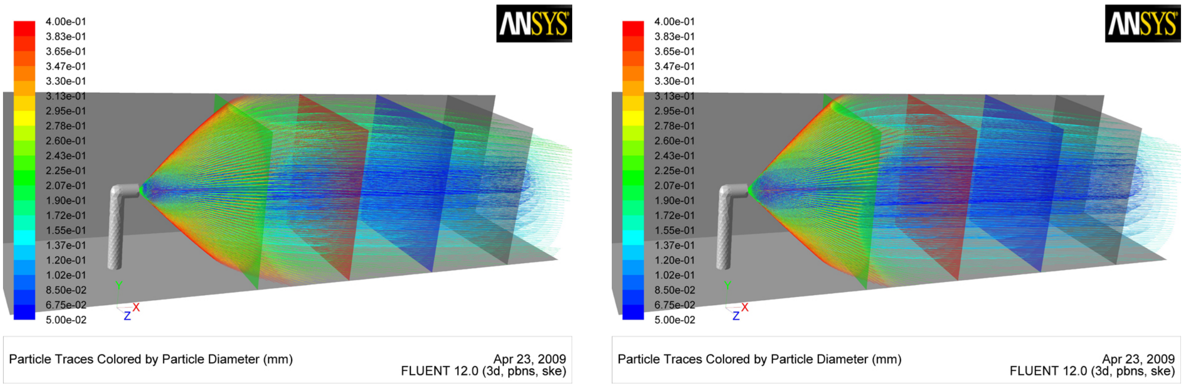

(a) $\Delta p_{nozzle} = 1bar$ (b) $\Delta p_{nozzle} = 10bar$

Figure 5.5: Simulations of liquid nozzle at $1.99bara$ and at a k-value of $0.35m/s$

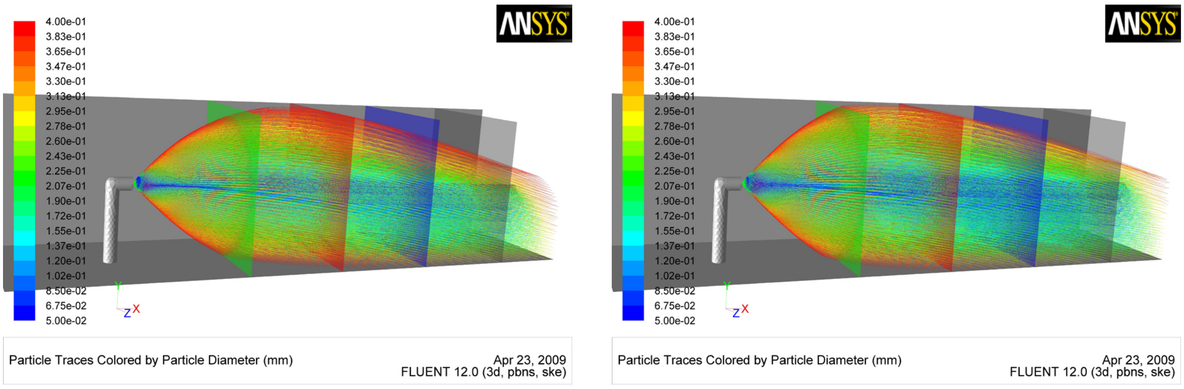

(a) $\Delta p_{nozzle} = 1bar$ (b) $\Delta p_{nozzle} = 10bar$

Figure 5.6: Simulations of liquid nozzle at $4.96bara$ and at a k-value of $0.35m/s$

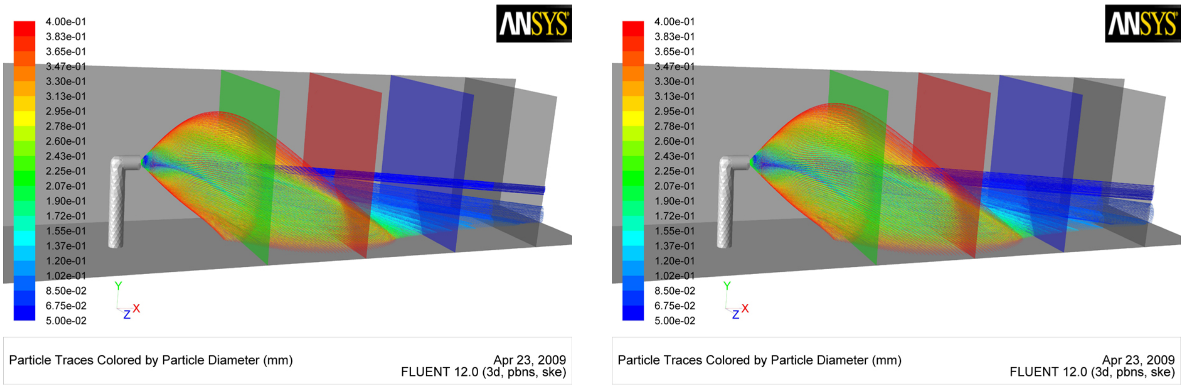

(a) $\Delta p_{nozzle} = 1bar$ (b) $\Delta p_{nozzle} = 10bar$

Figure 5.7: Simulations of liquid nozzle at $9.03bara$ and at a k-value of $0.35m/s$

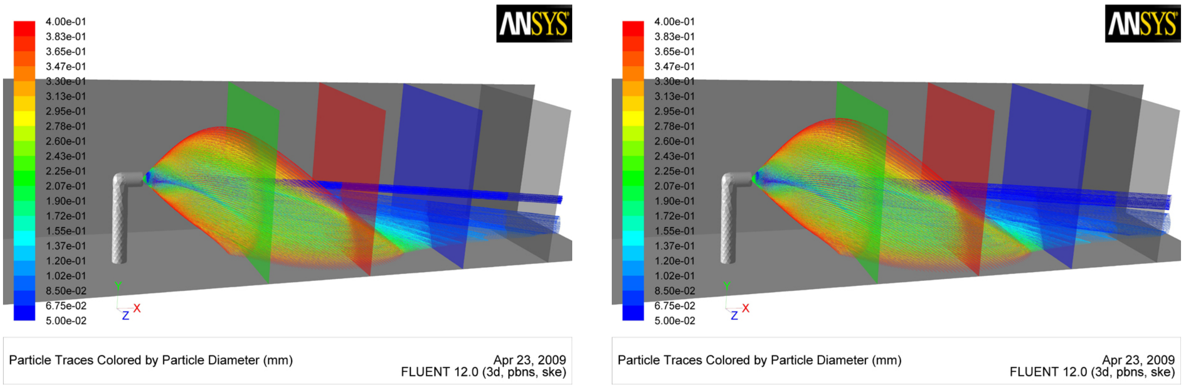

(a) $\Delta p_{nozzle} = 1bar$ (b) $\Delta p_{nozzle} = 10bar$

Figure 5.8: Simulations of liquid nozzle at $9.03bara$ and at a k-value of $0.15m/s$

## 5.4 The design of the vane pack test objects

In order to measure the performance of the reference geometry and geometry 2, they had to be built in such way that they fitted the test box. The number of vanes and the size of them were decided in Carlson and Talseth (2008), but the shape of the test object was not stated. The length of the test object is longer than both geometries, and this area was made like the up- and down-stream channel and placed behind the vane geometry, please refer to figure 5.2.

The chosen approach was to build the test object in a number of parts, and then screw them together. The vane section is placed at the top and a $10mm$ high transition section, only with the drainage chamber areas open, will then direct the separated liquid downwards. The separated liquid will then be directed into a narrowing section with one funnel for each drainage chamber and a height of $10mm$, and finally into a $20mm$ high pipe section, see figure 5.9. 1/4" pipes are screwed into the pipe section and submerged down in the drainage vessel to avoid gas through-put. The height of this submerging had to induce a larger hydrostatic pressure than the pressure difference over the vane pack, this was determined by the CFD result done by Carlson and Talseth (2008). The approach with pipes was chosen to keep the production cost of the test object at a minimum, due to a smaller structure and re-use of the pipes on all test objects. Other benefits with pipes are that one can easily test different parts of the vane pack by plugging some of the pipe holes, and the effect of submerging the vane pack drainage. From the top of the test object to the underside of the top cover there are a distance of approximately $20mm$.

The test object is open on the top, and to avoid an expansion of the flow area a glass cover was placed on top of the test object.

The actual vane pack section, see figure 5.10a, is $157mm$ high and the thinest walls are $1mm$. If these walls are not rigid, they could affect the flow patterns by oscillations, and thereby result in measuring error or in worst case, a fatal damage on the test object. Several manufactures were contacted, but only a few could achieve the given specifications. Two manufactures, using aluminum and limestone material respectively, were chosen to give a sample of the thinnest walls. The aluminum sample was superior compared to the limestone material, and the test objects were therefore machined in aluminum.

To make the transition from the drainage chambers to the pipes, funnels were constructed. The chosen pipe size was 1/4", and this is larger than the cross section of the chambers. Another challenge was to avoid the drainage chambers to puncture each other, which could cause gas through-put. The solution was to make a triangle shaped top which fitted the drainage chamber and a funnel to the pipe shaped bottom, see figure 5.10b. To make this funnel a VBA script was made to plot the edges in gambit, see appendix [APPENDIX HVOR KODEN STR].

Figure 5.11 shows a picture of the constructed geometries, the right hand side shows the reference geometry and the left hand side shows geometry 2. The construction of the

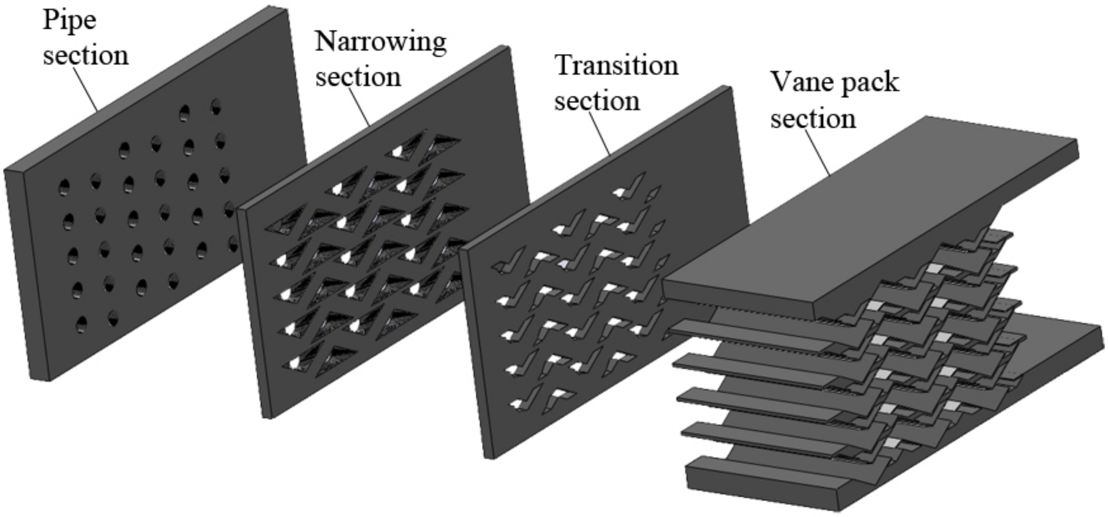

Figure 5.9: Seperated parts of the vane pack test object

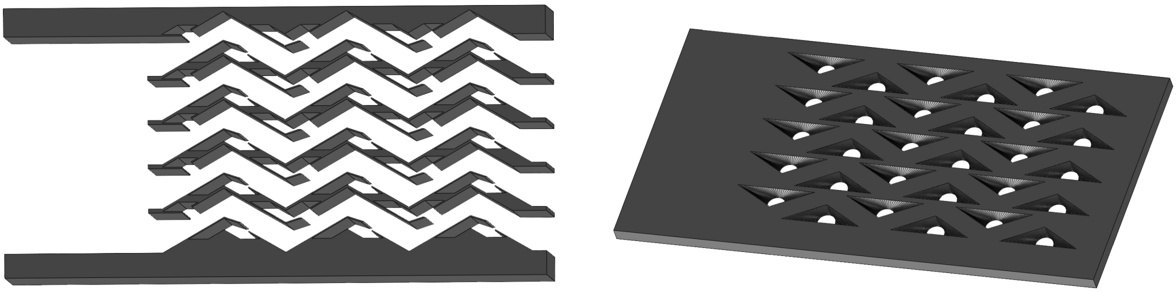

(a) The vane section (b) The narrowing section from triangle shape to pipe shape

Figure 5.10: Details of the vane pack test object

geometries were well performed, but due to the complex design of geometry 2 there were some fault in the construction. The curvature of the drainage slit had a sudden change, figure 5.12, that could cause unwanted flow patterns.

## 5.5 Imitation of high pressure natural gas

The gas used in the laboratory is Sulphur Hexafluoride, SF6. The gas is not hazardous for humans and it has a high density. Due to the high density it is therefore possible to do experiments with the same gas density as high pressure natural gas, at a lower pressure. Figure 5.13 shows the density of SF6 and natural gas, as a function of the pressure, calculated by HYSYS 3.2. The rig is operated with pressures ranging from $0.3barg$ and $10barg$. This corresponds to natural gas at pressures ranging from $8barg$ to $65barg$, see figure 5.13.

## 5.6 Test matrix

Before the experiments could start, the desired test variables and intervals had to be stated in a test matrix. Different intervals of pressure levels, liquid volume fractions and k-values were chosen and are shown in table 5.3.

Test matrix for all operating pressures are presented in tables 5.4, 5.5 and 5.6. The liquid flow varies from $1.08l/h$ to $369.66l/h$. The liquid pump in the test rig can operate with a maximum pressure difference of $10bar$, and the liquid nozzles are recommended to operate with a minimum pressure difference of $1bar$. None of the nozzles from the selected

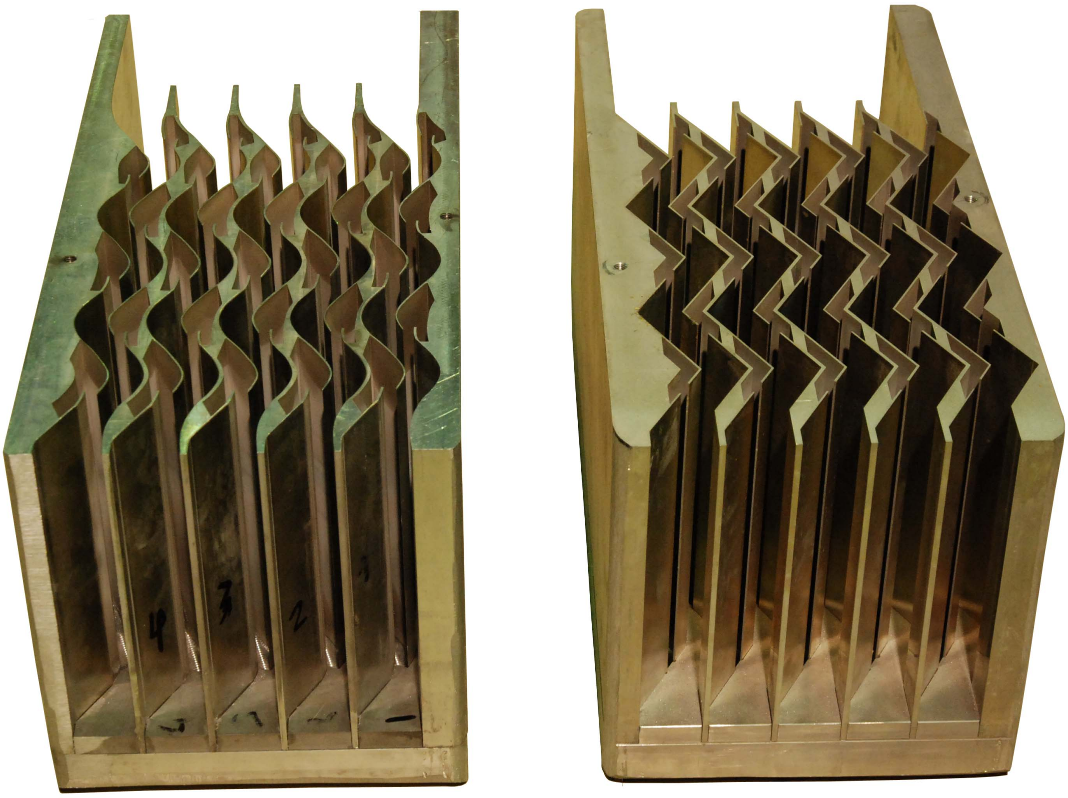

Figure 5.11: Both of the constucted geometries.

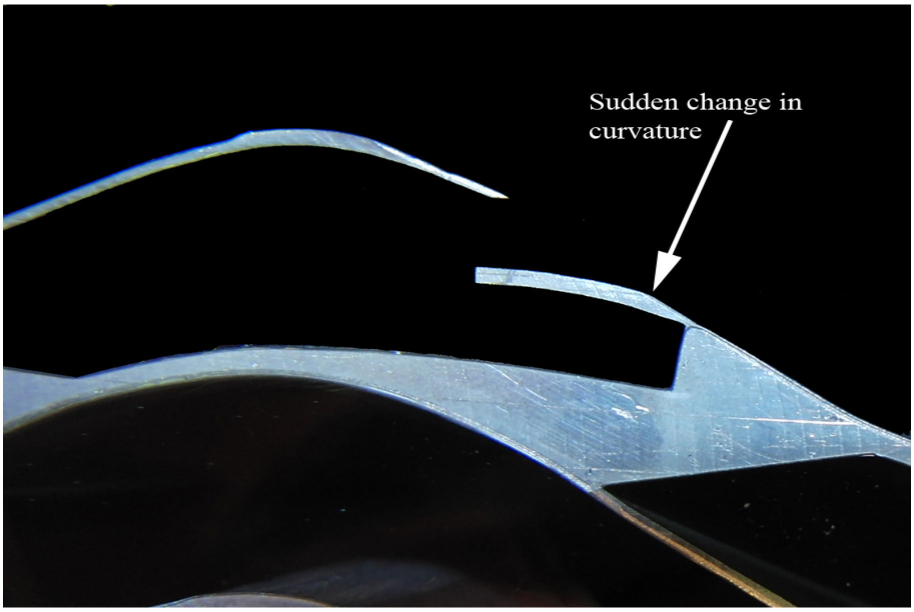

Figure 5.12: Close up of a drainage slit to the optimized geometry.

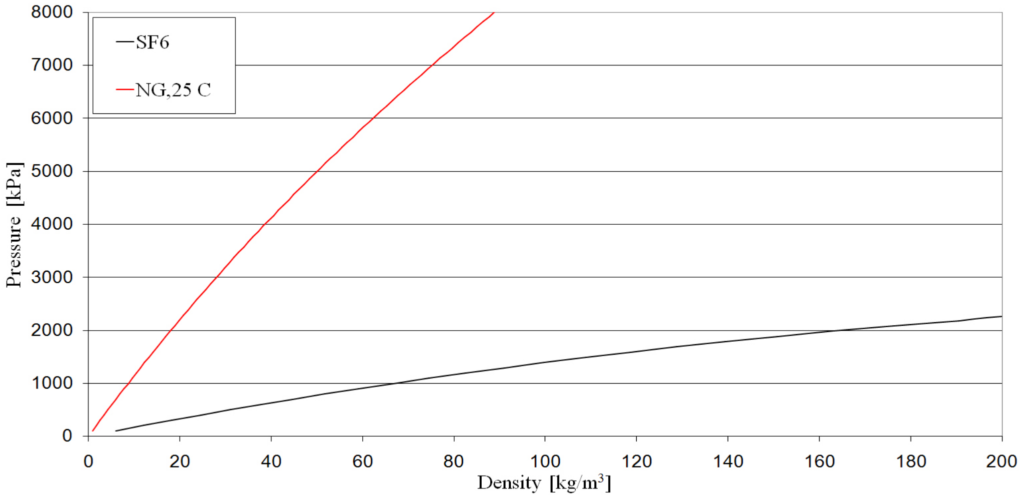

Figure 5.13: $\rho_{SF6}$ and $\rho_{NG}$ as function of pressure.

Table 5.3: The different intervals and variables for the test matrix

| Variables | Minimum value | Maximum value |
|---|---|---|
| Pressure [barg] | 1 | 8 |
| k-value [m/s] | 0.15 | 0.40 |
| Liquid volume fraction [%] | 0.02 | 0.15 |

manufacturer handles the variation presented in the test matrix, and it is necessary to replace and use several different nozzles, which is a time consuming process. To confine this replacement time, three nozzles were chosen, P20, P32 and P54. Nozzle data are presented in appendix B and shows the liquid flow at different $\Delta p_{nozzle}$. The lowest possible flow rate for the smallest nozzle, P20, is approximately $9.18 l/h$ and the highest flow rate for the largest nozzle, P54, is approximately $229.55 l/h$, some of the test points are therefore not feasible. An overview of the interval for each nozzle at the different k-value, liquid volume fraction and pressure level are presented in table 5.7. If one nozzle start or stop at the same k-value in table 5.7 as the next or previous nozzle, it means that the nozzles overlap each other. If a nozzle start and stop at the same k-value, it means that it is used at one k-value only.

Table 5.4: Test matrix for experiments at $0.99 barg$

| Temperature [$K$] | Pressure [$barg$] | Z-factor | $\rho_{SF6}$ [$kg/m^3$] | $\rho_{Exxsol}$ [$kg/m^3$] |
|---|---|---|---|---|
| 298 | 0.99 | 0.977 | 12.01 | 739.88 |

| | | Liquid volume fraction | | |
|---|---|---|---|---|
| | | 0.02% | 0.085% | 0.15% |
| k-value [$m/s$] | $Q_{blower}$ [$m^3/h$] | Liquid Flow [$l/h$] | | |
| 0.02 | 12.32 | 2.46 | 10.47 | 18.48 |
| 0.05 | 30.81 | 6.16 | 26.18 | 46.21 |
| 0.10 | 61.61 | 12.32 | 52.37 | 92.42 |
| 0.15 | 92.42 | 18.48 | 78.55 | 138.62 |
| 0.20 | 123.22 | 24.64 | 104.74 | 184.83 |
| 0.25 | 154.03 | 30.81 | 130.92 | 231.04 |
| 0.30 | 184.83 | 36.97 | 157.11 | 277.25 |
| 0.35 | 215.64 | 43.13 | 183.29 | 323.45 |
| 0.40 | 246.44 | 49.29 | 209.47 | 369.66 |

Table 5.5: Test matrix for experiments at $3.96 barg$

| Temperature $[K]$ | Pressure $[barg]$ | Z-factor | $\rho_{SF6}$ $[kg/m^3]$ | $\rho_{Exxsol}$ $[kg/m^3]$ |
|---|---|---|---|---|
| 298 | 3.96 | 0.941 | 31.06 | 740.23 |

| | | Liquid volume fraction | | |
|---|---|---|---|---|
| | | 0.02% | 0.085% | 0.15% |
| k-value $[m/s]$ | Q$_{blower}$ $[m^3/h]$ | Liquid Flow $[l/h]$ | | |
| 0.02 | 7.56 | 1.51 | 6.43 | 11.43 |
| 0.05 | 18.91 | 3.78 | 16.07 | 28.36 |
| 0.10 | 37.81 | 7.56 | 32.14 | 56.72 |
| 0.15 | 56.72 | 11.34 | 48.21 | 85.07 |
| 0.20 | 75.62 | 15.12 | 64.28 | 113.43 |
| 0.25 | 94.53 | 18.91 | 80.35 | 141.79 |
| 0.30 | 113.43 | 22.69 | 96.42 | 170.15 |
| 0.35 | 132.34 | 26.47 | 112.49 | 198.51 |
| 0.40 | 151.24 | 30.25 | 128.56 | 226.86 |

Table 5.6: Test matrix for experiments at $8.03 barg$

| Temperature $[K]$ | Pressure $[barg]$ | Z-factor | $\rho_{SF6}$ $[kg/m^3]$ | $\rho_{Exxsol}$ $[kg/m^3]$ |
|---|---|---|---|---|
| 298 | 8.03 | 0.8891 | 59.87 | 740.70 |

| | | Liquid volume fraction | | |
|---|---|---|---|---|
| | | 0.02% | 0.085% | 0.15% |
| k-value $[m/s]$ | Q$_{blower}$ $[m^3/h]$ | Liquid Flow $[l/h]$ | | |
| 0.02 | 5.34 | 1.07 | 4.54 | 8.00 |
| 0.05 | 13.34 | 2.67 | 11.34 | 20.01 |
| 0.10 | 26.68 | 5.34 | 22.68 | 40.02 |
| 0.15 | 40.02 | 8.00 | 34.02 | 60.04 |
| 0.20 | 53.36 | 10.67 | 45.36 | 80.05 |
| 0.25 | 66.71 | 13.34 | 56.70 | 100.06 |
| 0.30 | 80.05 | 16.01 | 68.04 | 120.07 |
| 0.35 | 93.39 | 18.68 | 79.38 | 140.08 |
| 0.40 | 106.73 | 21.35 | 90.72 | 160.09 |

Table 5.7: Overview over area of application for the different nozzles, $k$ refers to the k-value [m/s]

| p=1barg | | | | | | |
|---|---|---|---|---|---|---|
| | $\alpha_l = 0.02\%$ | | $\alpha_l = 0.085\%$ | | $\alpha_l = 0.15\%$ | |
| Nozzle | start at $k$ | stop at $k$ | start at $k$ | stop at $k$ | start at $k$ | stop at $k$ |
| P20 | 0.10 | 0.20 | 0.02 | 0.05 | 0.02 | 0.02 |
| P32 | 0.20 | 0.40 | 0.05 | 0.10 | 0.05 | 0.05 |
| P54 | – | – | 0.15 | 0.40 | 0.10 | 0.20 |
| p=4barg | | | | | | |
| | $\alpha_l = 0.02\%$ | | $\alpha_l = 0.085\%$ | | $\alpha_l = 0.15\%$ | |
| Nozzle | start at $k$ | stop at $k$ | start at $k$ | stop at $k$ | start at $k$ | stop at $k$ |
| P20 | 0.15 | 0.35 | 0.05 | 0.05 | 0.02 | 0.05 |
| P32 | 0.35 | 0.40 | 0.10 | 0.20 | 0.05 | 0.10 |
| P54 | – | – | 0.25 | 0.40 | 0.15 | 0.40 |
| p=8barg | | | | | | |
| | $\alpha_l = 0.02\%$ | | $\alpha_l = 0.085\%$ | | $\alpha_l = 0.15\%$ | |
| Nozzle | start at $k$ | stop at $k$ | start at $k$ | stop at $k$ | start at $k$ | stop at $k$ |
| P20 | 0.20 | 0.40 | 0.05 | 0.10 | 0.05 | 0.05 |
| P32 | – | – | 0.15 | 0.30 | 0.10 | 0.15 |
| P54 | – | – | 0.35 | 0.40 | 0.20 | 0.40 |

# Chapter 6

# Results

## 6.1 Measurements, uncertainty and boundary effects

This section discuses the measurement method, uncertainties and errors caused by the equipment and human, and the boundary effects of the experiments.

### Measurements in the laboratory

The rig is controlled by Labview, a computer program that controls the different outputs, e.g. blower and liquid pump, and records the desired input values, e.g. pressure and temperature in the test loop. The different outputs and inputs are listed in table 6.1. Every output and input signal is an electrical current varying from $4mA$ to $20mA$. The electrical currents are transformed into the desired parameters through a scaling matrix, with a chosen interval for each signal. *Controller* 1 and 2 are sent to a frequency converter and calibrated to give $0Hz$ at a signal of $4mA$ and $50Hz$ at a signal of $20mA$. *Controller* 3 is calibrated with a closed cooling water valve for $4mA$ and fully open for $20mA$. The input signals come from pressure differential cells and a temperature transmitter. The pressure differential cells are constructed to operate over a certain pressure difference, and the calibration was done by defining a minimum transmission point, $4mA$. The maximum transmission point, $20mA$, could then be checked by a hearth communicator. To avoid measuring errors it was important to ensure that the pipe connection between the measuring point and the cell was filled by a homogeneous compound. The temperature transmitter is working and calibrated in the same manner as the pressure differential cells. Labview is capable to report several more parameter than the input signals, e.g. mass flow, density and k-value. This is achieved by using the input signals and chosen constants

Table 6.1: The different outputs and inputs in Labview

| Outputs | |
|---|---|
| Name of parameter | Description |
| $Controller$ 1 | Managing gas blower |
| $Controller$ 2 | Managing liquid pump |
| $Controller$ 3 | Managing water cooling valve |

| Inputs | |
|---|---|
| Name of parameter | Description |
| $P_{Q_{gas}}$ | Pressure in pipe vs. atmosphere upstream the gas metering orifice [$barg$] |
| $\Delta P_{Q_{gas}}$ | Pressure drop over gas metering orifice [$bar$] |
| $P_{Testbox}$ | Pressure in test box vs. atmosphere [$barg$] |
| $T_{gas}$ | Temperature in pipe downstream metering orifice [$^oC$] |
| $\Delta P_{Nozzle}$ | Pressure drop over liquid injection nozzle [$bar$] |
| $\Delta P_{VP}$ | Pressure drop over vane pack section [$bar$] |

in programmed formulas.

The different measuring points at each pressure level in the test matrix are defined by the k-value at the vane pack inlet and the liquid flow rate. The liquid injection flow rate is estimated by the given nozzle data, appendix B, and the reported pressure drop over the liquid injection nozzle, $\Delta P_{Nozzle}$. The reported k-value is calculated from the following formulas:

$$k = \frac{Q_{gas}}{3600\ A_{vaneinlet}} \sqrt{\frac{\rho_{testbox}}{790 - \rho_{testbox}}} \tag{6.1}$$

where:

$$Q_{gas} = \frac{\dot{m}_{gas}}{\rho_{testbox}} \tag{6.2}$$

$$\rho_{testbox} = \frac{P_{Testbox} * 100000 + P_{std}}{R(T_{gas} + 273.15)(1 - 0,014(P_{Q_{gas}} + 1))} \tag{6.3}$$

$$\dot{m}_{gas} = 3600\ E\ C_{D_{SF6}}\ A_t \sqrt{\frac{2\rho\ \ MAX(0.0001, \Delta P_{Q_{gas}})100000}{\sqrt{1 - B^4}}} \tag{6.4}$$

Definitions of $E$, $C_{D_{SF6}}$, $A_t$, $\rho$ and $B$ can be found in appendix C.

Flow rates of the separated liquid and of the liquid carry over, LCO, at each test point were calculated by measuring the liquid volume in MC1, MC2 and MC3 at two different times, $Q_{liquid} = \frac{\Delta V}{\Delta t}$. It was assumed that the high performance gas/liquid separator, VG02, was removing 100% of the LCO from the test object. Since VG02 has a mesh pad, two cyclones and a larger cross section, which gives a lower k-value, this assumtion is satisfactorily. The separation efficiency of the vane pack geometries is then found by comparing the separated liquid flow rate and the LCO flow rate by the following formula:

$$\eta = 1 - \frac{Q_{LCO}}{Q_{separated\ liquid} + Q_{LCO}} \tag{6.5}$$

## Uncertainty of the laboratory experiments

An uncertainty analysis of the experiments is a useful tool to analyse the results of the experiments, and can be calculated based on the measuring equipment and methods. All equipment has a uncertainty and is given by the producer. The inaccuracy and uncertainty in measurements together with noise and varying physical properties reduces the accuracy of the derived values, e.g. gas flow rate and density of the gas. The tables in appendix C describes the given uncertainty of the equipment and constants in the laboratory. Generally, the error in a derived variable, $F(x_1, x_2, x_3, ...x_n)$, can be expressed as:

$$dF = \sum_{i=1}^{n} |\Delta x_i \frac{\partial F}{\partial x_i}| \tag{6.6}$$

Human and systematic errors in experimental measurements are usually the dominating one, and it is important to include these in the analysis. Possible human errors of measurements in the experiments are inaccurate reading of the measuring cups and stop watch. These uncertainties are set to $1mm$ and $1s$ for the measuring cup and stop watch respectively, and implemented in the calculation of error in the derived variables. An other important source of error can arise if each test point is not given sufficient time to stabilize, this is reduced by calculating the flow rate in the measuring cups continuously. Each test point has been measured at least five times to reduce the standard deviation of each test point. Equation 6.7 shows how the uncertainty for the reading reduce as the sampling size N increase.

$$s_{\overline{x}} = \frac{s}{\sqrt{N-1}} \tag{6.7}$$

where $N$ is the number of samplings and $s$ is the individual standard deviation (Doebelin, 1990).

The used formulas for the derived variables and their calculated error is presented in appendix C. The separation efficiency is defined in 6.5 and the uncertainty of the separation efficiency defined as:

$$\Delta\eta = \frac{1}{Q_{injected\ liquid}}\Delta Q_{LCO} + \frac{Q_{LCO}}{(Q_{injected\ liquid})^2}\Delta Q_{injected\ liquid} \tag{6.8}$$

Where:

$$Q_{liquid\ injection} = Q_{separated\ liquid} + Q_{LCO} \tag{6.9}$$

$$\Delta Q_{liquid\ injection} = \Delta Q_{separated\ liquid} + \Delta Q_{LCO} \tag{6.10}$$

Figure 6.1 shows clearly that the uncertainty in the experiments with the reference geometry, ref, is dependent of which nozzle is used. At a separation efficiency of 90% the uncertainty of nozzle P54 is approximately 6 times less than nozzle P32. The uncertainty in the experiments with Geometry 2, geo2, has not the same dependence on which nozzle that is used, figure 6.2. At 90% separation efficiency nozzle P20 gives an uncertainty of approximately 0.8% in the ref experiments and approximately 1.1% in the geo2 experiments. At 90% separation efficiency nozzle P32 gives an uncertainty of approximately

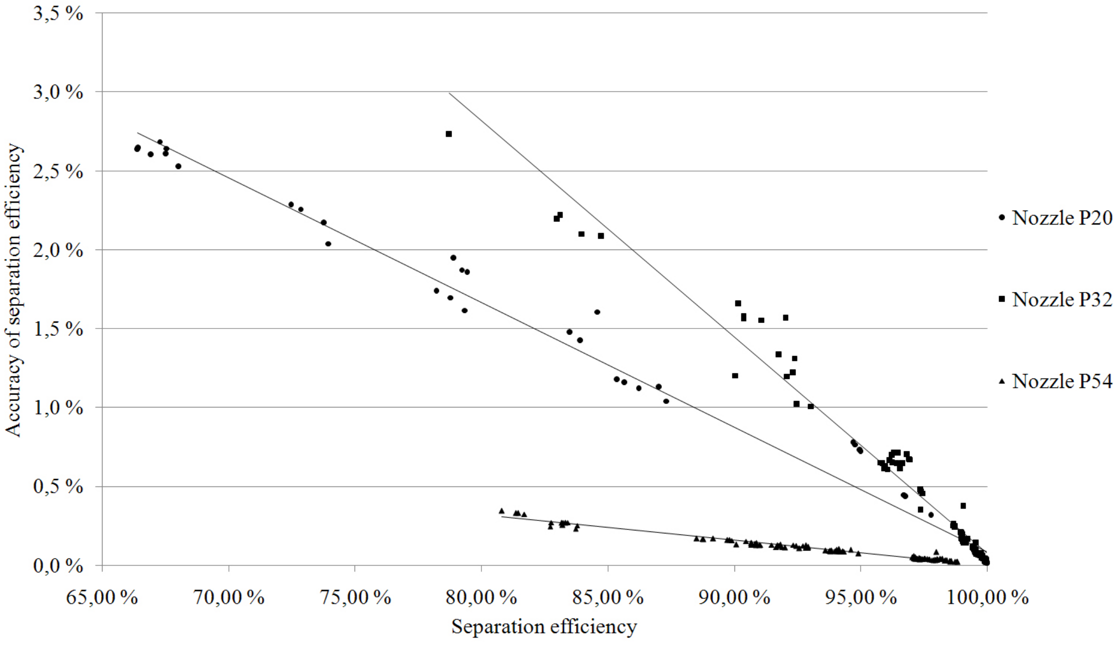

Figure 6.1: Accuracy analysis of the experiments with the reference geometry

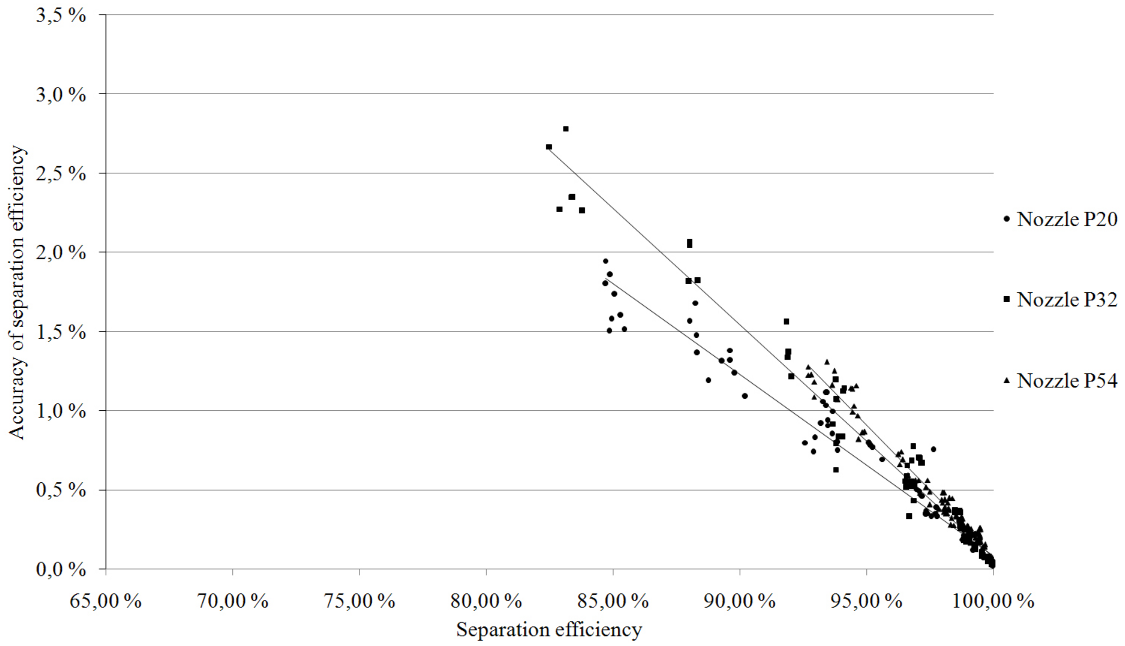

Figure 6.2: Accuracy analysis of the experiments with geometry 2

1.4% in the ref experiments and approximately 1.5% in the geo2 experiments. Both nozzle shows a similar uncertainty which is expected, but Nozzle P54 goes from beeing the least uncertaint in ref experiments to the most uncertaint in the experiments with geo2. Nozzle P54 at 95% gives an uncertainty of approximately 0.1% in the ref experiments and approximately 0.9% in the geo2 experiments. This relatively large difference, 12 times more uncertainty in the geo2 experiments, was unexpected. Higher flowrates gives a smaller uncertainty. The LCO flowrate at the measurements of geo2, was reduced due to the higher efficiency. This causes an decrased LCO flow rate and an almost constant separated liquid flowrate.

## Boundary effects of the experiments

The nozzles form the basis for a major boundary effects in the experiments, poor spread and liquid on the walls/glass cover. Figure 6.3 illustrates the orientation of the camera lens regarding figure 6.4, 6.5 and 6.4a. It should be mentioned that achieving snapshots under running experiments gave some difficulties. This was mainly due to light reflection from the glass cover over the test object and the see glass on the test box cover in addition to the bright vane pack metal. It was not possible to place any light sources inside the test box, so all light had to come from the same opening as the pictures were taken. This lead to various light conditions and it was thereby difficult to take comparable and representative pictures.

The trends in the CFD simulation of the nozzle performance in section 5.3 was visually confirmed by the experiments. Figure 6.4 shows the liquid spread with nozzle P32 at two different k-values. Although it is not clear from the picture, it was clearly seen by naked eye during the experiments that the liquid spread was nearly unaffected by the k-value, refer figure 5.7 and 5.8. The visible channels had a similar liquid load respectively, but this was unfortunately not possible to confirm with the available equipment in the rig.

The pressure in the rig influenced the liquid spread greatly, figure 6.5, and confirm the behavior that was shown in the nozzle CFD simulation, figure 5.5, 5.6 and 5.7. Figure 6.5a illustrates the liquid spread of nozzle P54 at $p = 1 barg$ and $k = 0.35 m/s$ and shows

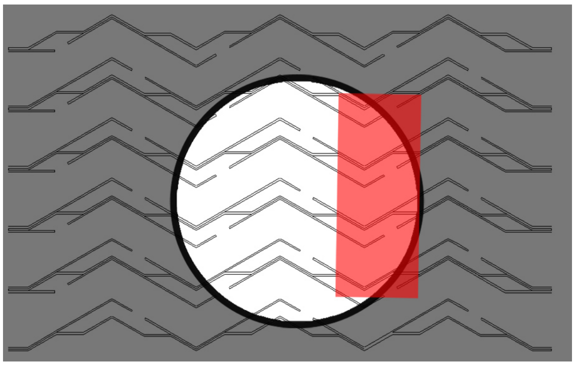

Figure 6.3: Orientation of the camera lens. Flowing from right to left.

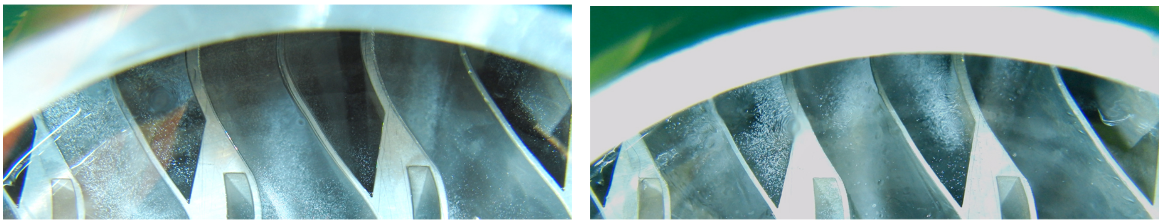

(a) $k = 0.05 m/s$

(b) $k = 0.40 m/s$

Figure 6.4: Pictures of the spread with nozzle P32 at $1 barg$ and two different k-values. Flowing from the top and downwards.

that at least three channels are utilized even if the channel in the middle had a greater load. Some of the liquid flows along the glass cover which fits well with the simulations in figure 5.5. At $p = 4barg$ and $k = 0.35m/s$, figure 6.5b, the spread was clearly reduced with a major fraction hitting the channel in the middle, and some liquid utilizing the two channels next to the middle one. The height of the spread was also reduced. Figure 6.5c shows the spread at $p = 8barg$ and $k = 0.35m/s$, and shows a similar scattering as at $p = 4barg$ and $k = 0.35m/s$. It could seem like the spread is larger at $p = 8barg$, but this is probably a result of challenging light conditions. The nozzle CFD simulations at these pressures, figure 5.6 and 5.7, shows the same tendency, but the effect of pressure was larger in the laboratory, especially at $p = 4barg$. This could be because the droplet diameter is reduced at higher pressures, and this was not taken into account in the simulations. One can however see from the simulations that the spread for the smaller droplet diameters, $d < 200\mu m$, are not reduced in the same manner as for the larger diameters, $d > 200\mu m$. The result of the different spread, due to different nozzle and operational condition, were unfortunate and the varying utilization of the vane pack channels could most likely affect the measurements.

At high liquid load there was flow along the glass cover at all pressures, figure 6.6a shows this at $p = 8barg$, $k = 0.35m/s$ and $\alpha_{liquid} = 0.15\%$. A small liquid river at the bottom of the vane pack was observed at all pressures, k-values and liquid loads, figure 6.6b, but particulary at high liquid load and a low k-value. The effect of these two phenomena is uncertain, due to the unknown fate of the liquid. Some of the liquid that hit the wall and glass cover was drained via the dranaige chambers and via the small openings at the start and end of the test object. It is presumable to believe that some of the liquid was also draged with the gas flow and counted as LCO, especially the liquid on the glas cover. This phenomena could effect the efficiency measurements a great deal.

A consequence of the boundary effects mentioned above are that the flow capacity of the drainage chambers could have been reached. To secure the flow in the vertical drainage pipes the dimensioning of pipe sizes was based on a maximum liquid froude number, $Fr$, of 0.30. $Fr$ compares the ratio between the inertia forces and the gravitational forces and defined as, (Hills, 1983):

$$Fr = \frac{u_{l_p}}{\sqrt{g d_{pipe}}} \sqrt{\frac{\rho_l}{\rho_l - \rho_g}} \tag{6.11}$$

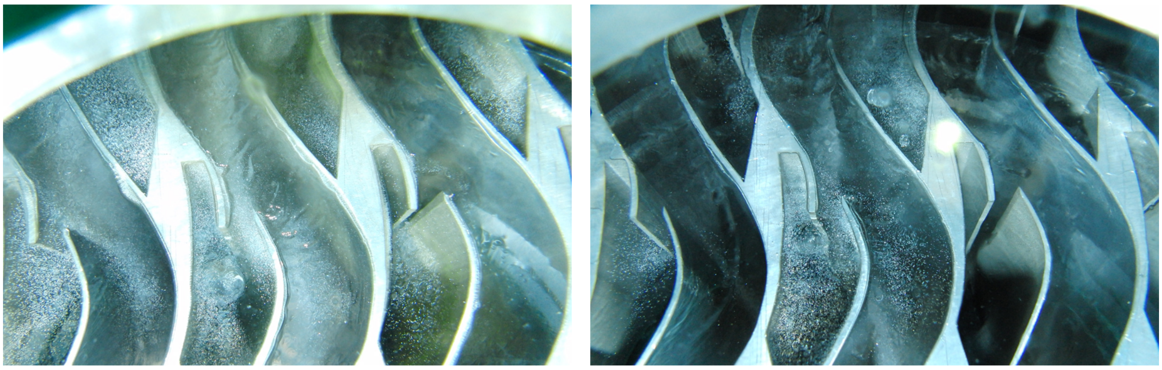

(a) $p = 1barg$ (b) $p = 4barg$

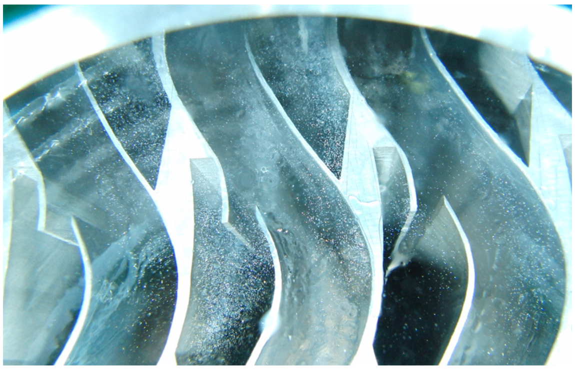

(c) $p = 8barg$

Figure 6.5: Pictures of the spread with nozzle P54 at $k = 0.35m/s$ and three different pressures. Flowing from the top and downwards.

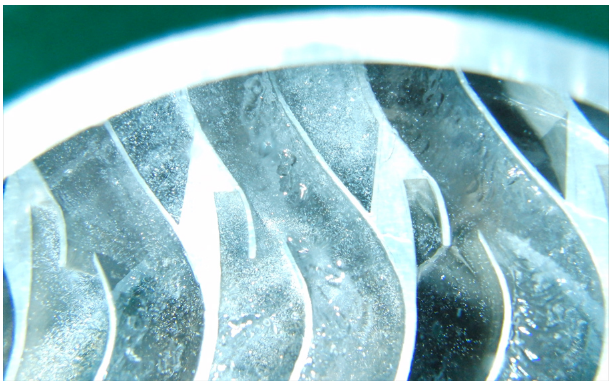

(a) Flow at glas cover.

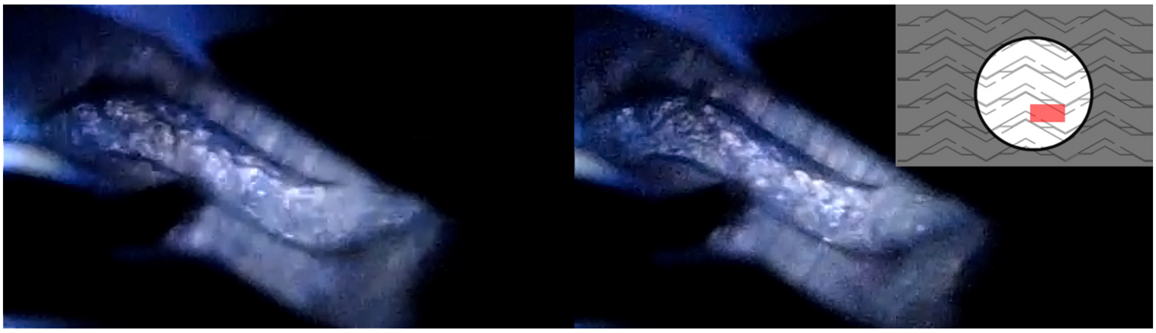

(b) Flow at vane pack bottom.

Figure 6.6: Pictures illustrating liquid flow at the glass cover and vane pack bottom

where $u_{l_p}$ is the superficial liquid velocity in the pipe and defined as:

$$u_{l_p} = \frac{Q_l}{\pi/4d_{pipe}^2} \tag{6.12}$$

The maximum criteria of $Fr = 0.30$ is set to ensure an annular liquid flow, which will prevent gas from being sucked down and obtain a necessary low superficial velocity (Simpson, 1968). The maximum value of $Fr = 0.30$ is also recommended by NORSOK (1996).

The maximum liquid injection in the experiments with nozzle P54 is calculated to $226.86 l/h$. Based on this the following criteria for the drainage was set:

- The drainage pipe on the test box should at least handle a liquid flow of $240 l/h$ under the given specification for $Fr$.

- The first row of drainage pipes in the test object, five pipes, should be capable to drain 100% of the maximum liquid injection, $240 l/h$.

A drainage pipe with a diameter of 1" was then installed in the test box, which obtained $Fr = 0.225$ at $Q_l = 240 l/h$. The size of the pipes for the drainage chambers were decided to have a diameter of 1/4". This was not sufficient to drain the given maximum liquid load, but a flow capacity of $209.5 l/h$ for the first row of drainage pipes was determined to be sufficient because it was not likely that the first row had a separation efficiency of 100%.

The CFD simulation of the nozzle spread and the experiments showed that not all of the channels were utilized, and thereby that the liquid load on a part of the channels was higher than expected. Unfortunately this was not discovered before the construction was started. To examine how this drawback could have affected the separation efficiency measurements a plot of the minimum number of drainage pipes in the test object needed to drain a given liquid load at $Fr = 0.30$ was plotted, figure 6.7. One pipe in the test box has a maximum flow capacity of approximately $30 l/h$. This means that if less than four channels are utilized the maximum flow capacity of the drainage pipes in the test box could have been reached in a number of test points, and thereby lowering the separation efficiency and cause measuring error.

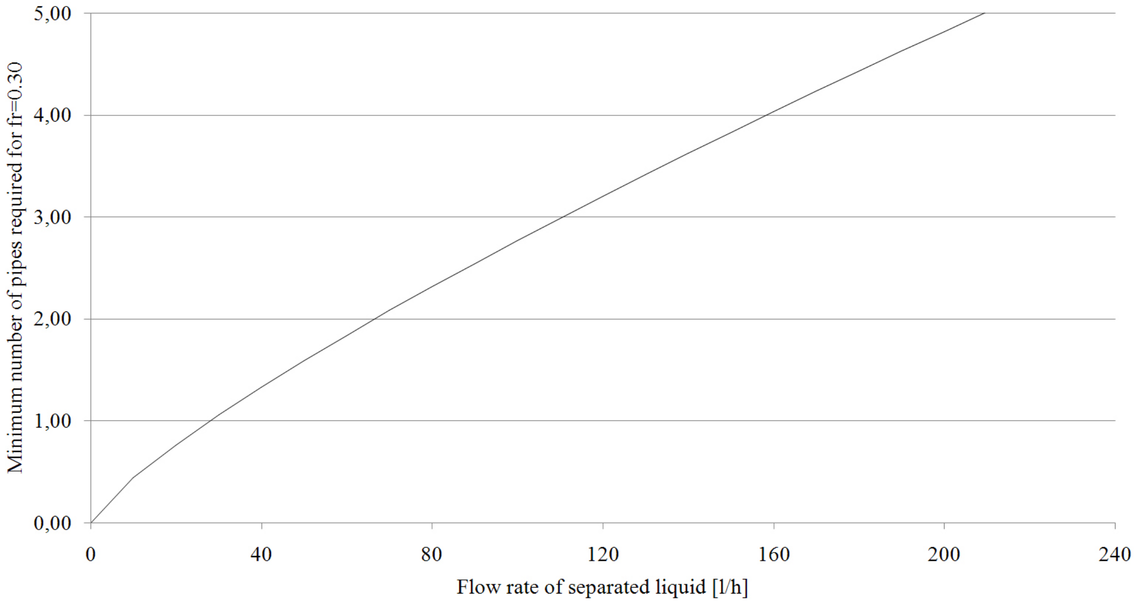

Figure 6.7: Plot of the minimum number of pipes needed to drain a given liquid load at $Fr = 0.30$

## 6.2 Experimental result

### Separation efficiency measurements

The separation efficiencies are presented in this section. They are calculated by taking the average of stabilized measurements of each test point. The result of the experiments are presented in figure 6.9, 6.11 and 6.12. Black lines represent the reference geometry, ref, and red lines represent geometry 2, geo2.

The standard deviation was checked for five samples at every test point and plotted for $\alpha_l = 0.08\%$, which is representative for all $\alpha_l$, to see if the samples are congruent, see figure 6.8. The plot shows that the standard deviation is quite small, and that geo2 generally has a smaller deviation in the samples. The standard deviation increases at higher $k$, due to the lower efficiency and larger uncertaity in the samplings. Ref has a peak at $p = 8barg$ and $k = 0.30m/s$ with a standard deviation of nearly 1%, which is twice as high as the second highest value, figure 6.8c. This might have been caused by a unstabilized sampling.

Figure 6.9 shows the results from the separation efficiency, $\eta$, measurements at $p = 1barg$. $\eta$ for the reference geometry is called $\eta_{ref}$ and $\eta$ for geometry 2 is called $\eta_{geo2}$. The results

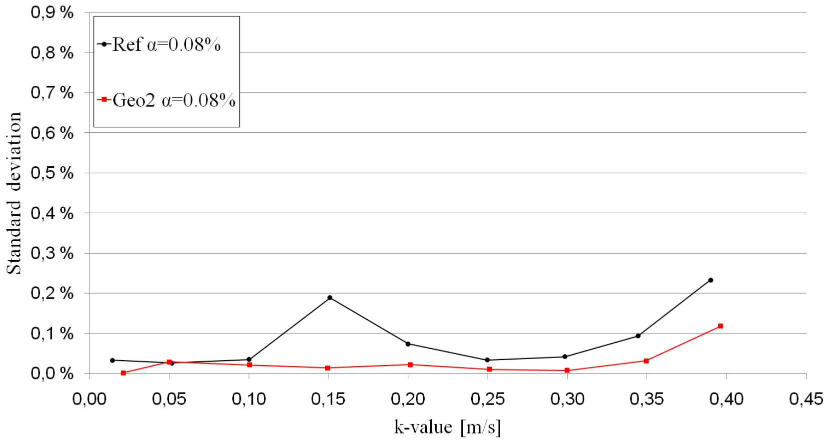

(a) $p = 1barg$

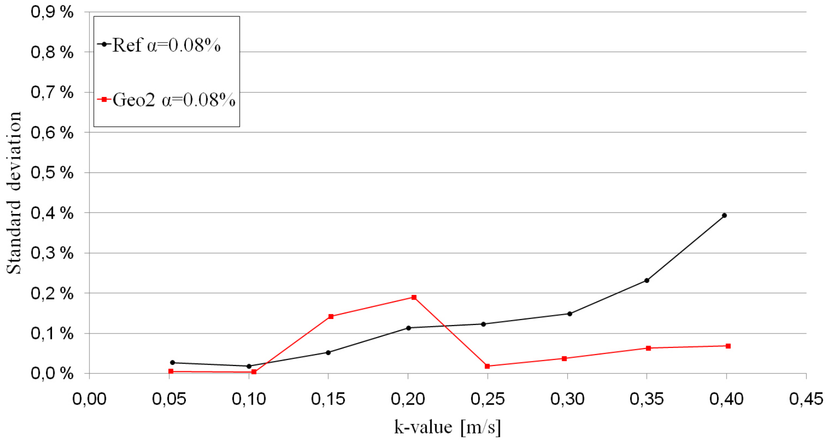

(b) $p = 4barg$

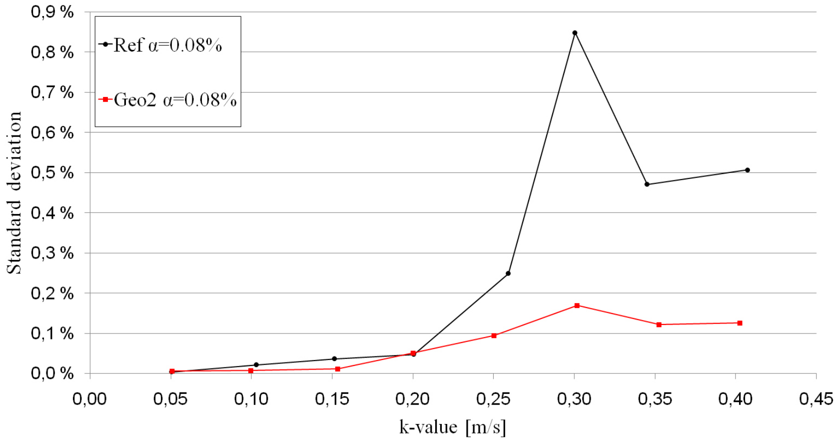

(c) $p = 8barg$

Figure 6.8: The standard deviation for the test points at the different pressures and $\alpha_0.08\%$

for both geometries at all liquid loads are unified and shows a similar performance and tendency, and $\eta$ is above 97% until $k > 0.30$ where $\eta$ decrease. At $\alpha_l = 0.02\%$ $\eta_{ref}$ decrease and stabilize about 96% for $k > 0.35m/s$, while $\eta_{geo2}$ decrease from 98.7% at $k = 0.35m/s$ to 83% at $k = 0.40m/s$. It was unexpected that $\eta_{geo2}$ decreased in this manner compared to ref, the standard deviation for geo2 is 0.5% and do not explain the large difference in performance. With a $\alpha_l = 0.08\%$ geo2 perform better when $k > 0.10m/s$. $\eta$ drops for both geometries at $k = 0.35m/s$. Geo2 seems to have a higher $\eta$ for all the measured test points at $\alpha_l = 0.15\%$. The result for geo2 shows a better performance at higher $\alpha_l$, and this trend could not be seen for ref where higher $\alpha_l$ decreased the performance. The difference in the performance were nevertheless not large. Based on the perfomance in the experiments at $p = 1barg$ non of the geometries seems to differ from the other.

The influence of the boundary effects on $\eta$ was not measured, but the experimental results could give an indication. The different nozzles have different openings, which leads to a variation in spread and droplet diameter. Table 5.7 shows at which test point the different nozzles have been used. The nozzle dependency is more noticeable with geo2, especially at $\alpha_l = 0.02\%$ from $k = 0.15m/s$ to $k = 0.20m/s$ and $\alpha_l = 0.08\%$ from $k = 0.10m/s$ to $k = 0.15m/s$, figure 6.9. It should be noticed that the effect of the nozzle replacement is of minor importance for the performance at this pressure level. The liquid flow rate at $p = 1barg$ is largest, and might therefore create problems of draining the liquid. At the same time, the spread of the nozzles was largest at this pressure level, and at least three channels where utilized. This gives an estimated liquid drainage capacity of minimum $130l/h$, please refer to figure 6.7, for the first row, which covers most of the test points. The last test point with $\alpha_l = 0.15\%$ and the three latest test points with $\alpha_l = 0.08\%$ have a larger liquid flow rate than $130l/h$. The effect of drianage problem is as mentioned uncertain and could give a higher or lower $\eta$, it is still likely that liquid that hit the walls in the upstream channel were counted as separated liquid. This will favour $\eta$ at low pressure, due to the largest spread, see figure 5.5 of the CFD simulation of the nozzle.

Results from the experiments at $p = 4barg$ are presented in figure 6.11. The results are more scattered at $p = 4barg$ than at $p = 1barg$. For $0.02 \leqslant k \leqslant 0.10m/s$ $\eta$ is high and approximately equal, and the performance decreases for $k > 0.10m/s$ for both geometries, except for geo2 with $\alpha_l = 0.15\%$. $\eta_{geo2}$ is generally higher at all test points than $\eta_{ref}$ for $k > 0.10m/s$. At $\alpha_l = 0.02\%$ $\eta_{ref}$ decreases more rapidly for $k > 0.15m/s$, and $\eta_{ref}$ drops

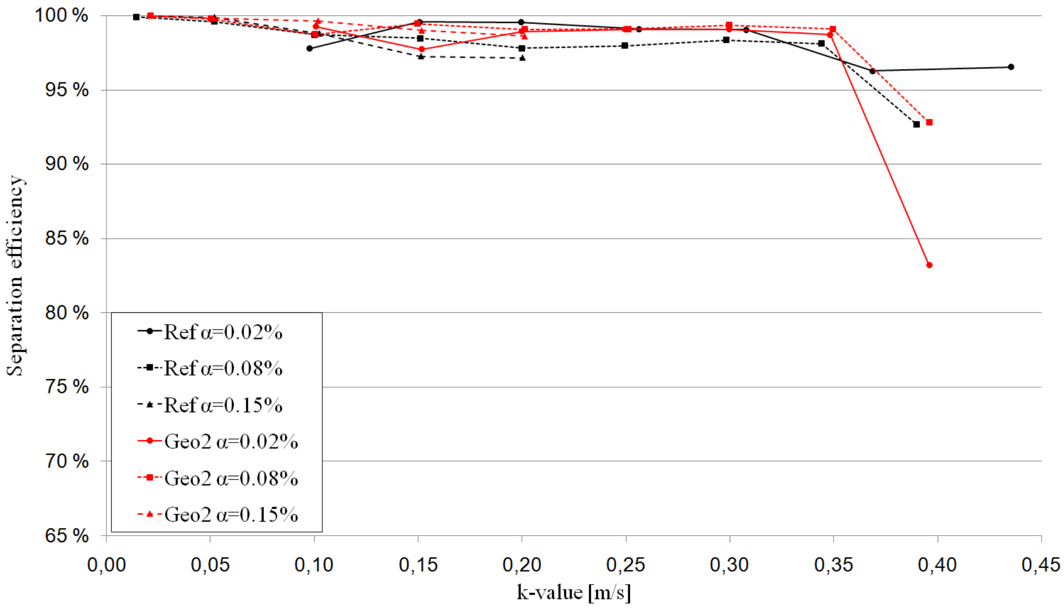

Figure 6.9: Separation efficiency of the reference geometry and geometry 2 at $p = 1barg$ and different liquid load plotted against k-value

to $\approx 79\%$ while geo2 stabilizes at $\eta \approx 93\%$. At $k = 0.30m/s$ $\eta_{ref}$ increase, and this marked tendency is not found for geo2. Observations in the experiments of ref showed that at a certain $k$, the droplet stream hit the drainage slit almost perfectly, which increased the performance. This was observed by the naked eye at $k = 0.35$, see figure 6.10, and could therefore explain the sudden increase in performance.

Both geometries have a sudden increase in the performance at $k = 0.25m/s$ when $\alpha_l = 0.08\%$, figure 6.11. The reason for these phenomena might be that there was a nozzle replacement between $k = 0.20m/s$ and $k = 0.25m/s$, which results in a varying spread and droplet size. The nozzle depency is particularly noticeably at this point since both geometries show the same trend. At $\alpha_l = 0.15\%$ $\eta_{geo2}$ is relativly high compared to $\eta_{ref}$, and is stable until $k = 0.35m/s$ where $\eta_{geo2}$ decreases.

Geo2 at $\alpha_l = 0.15$ from $k = 0.10m/s$ to $k = 0.15m/s$ shows an unexpected increase in performance which could have been caused by the use of different nozzles, figure 6.11, but this is of minor importance for the performance. The spread of the nozzle at $p = 4barg$ is considerably smaller compared to the spread at $p = 1barg$, and one or two channels are fully utilized. This means that the drainage capacity for the first row is reduced to

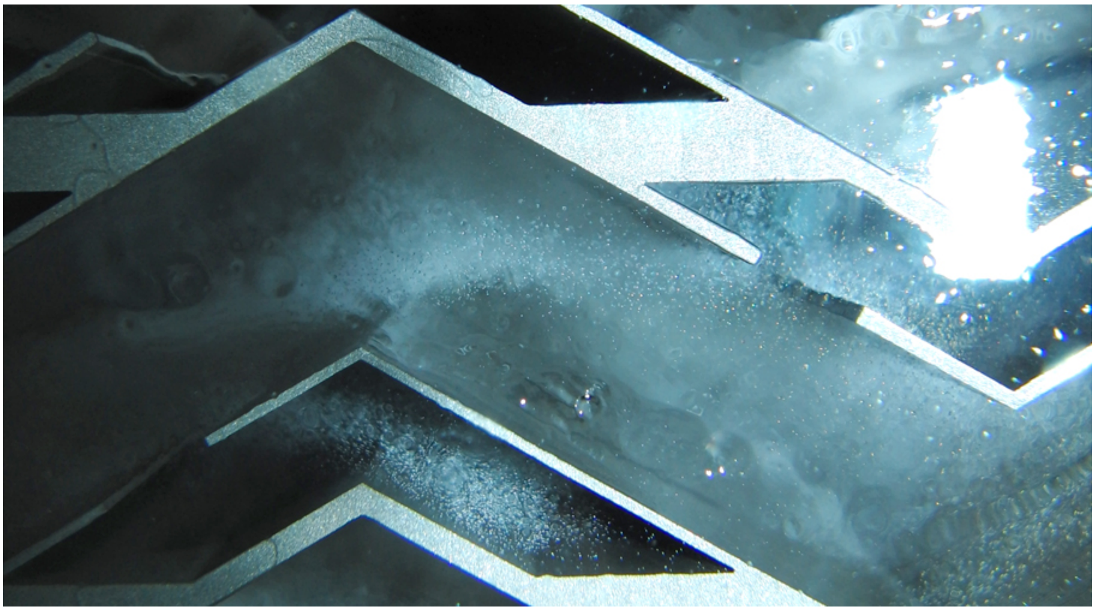

Figure 6.10: Droplet stream hitting the drainage slit. Flowing from left to right.

approximately $35-75 l/h$, which again could have caused problems of draining the liquid at some test points.

Based on the experiments at $p = 4barg$, it is clear that geo2 has a better performance than ref. The difference in $\eta$ increases generally with higher $k$ and both geometries shows a better performance at higher $\alpha_l$, figure 6.11. The performance of geo2 is more stable, and has not the same dependency on $\alpha_l$ at this pressure as ref.

The performance for the geometries from the experiments at $p = 8barg$ is presented in figure 6.12, and shows a similar tendency as the experiments at $p = 4barg$, but $\eta$ is more uniform for $k \leqslant 0.20m/s$. $\eta$ drops gradually for both geometries when $\alpha_l = 0.02\%$ for higher $k$, but geo2 has a better performance. From $k = 0.30m/s$ to $k = 0.35m/s$ both geometries have a sudden rise in $\eta$ for $\alpha_l = 0.08\%$, and this has most likely the same explanation as in the experiments at $p = 4barg$ and with $\alpha_l = 0.08\%$. $\eta_{geo2}$ is higher than $\eta_{ref}$ when $\alpha_l = 0.15\%$, and both geometries drop gradually for higher $k$. The results from the experiments at $p = 4barg$ and at $p = 8barg$ are similar and show the same trends. It should be mentioned that some of this congruent behavior could have been caused by the boundary effect, because both experiments experienced an almost homogeneous nozzle spread and the nozzle setup is similar.

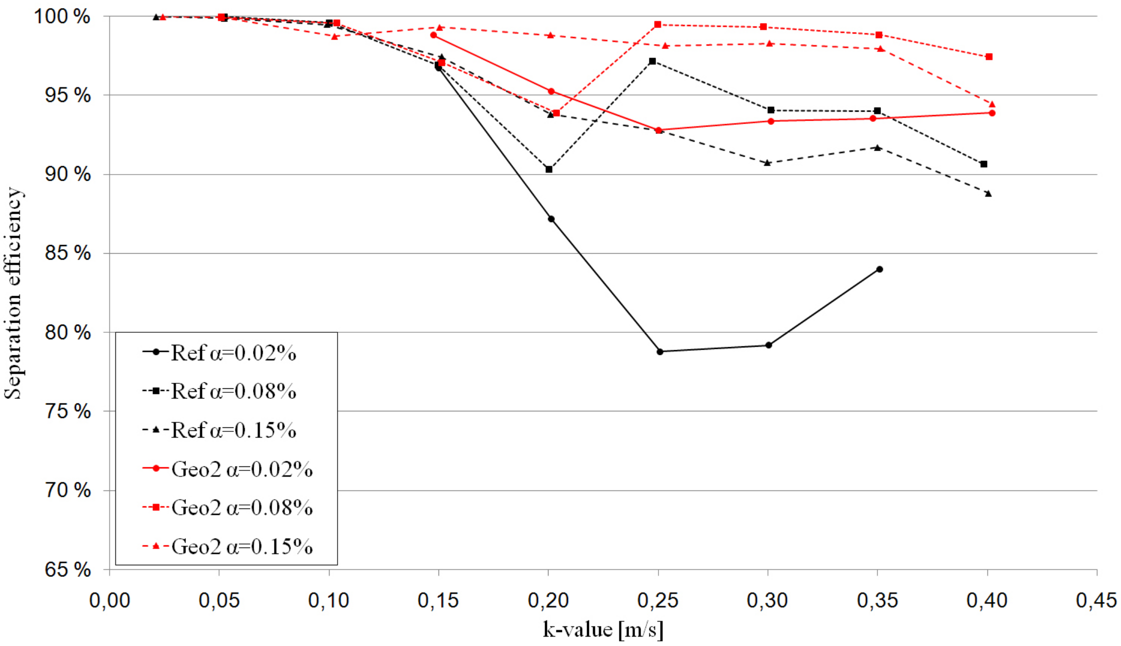

Figure 6.11: Separation efficiency of the reference geometry and geometry 2 at $p = 4barg$ and different liquid load plotted against k-value

Both geometries shows a similar $\eta$ at the lowest $k$ and have a decrease in $\eta$ at approximately the same $k$ at each pressure level. $\eta$ at $p = 1barg$ has a higher value over a larger interval of $k$ than at higher pressure levels. The result for $\eta$ from the experiments shows that $\eta_{geo2}$ generally is higher compared to ref, especially at higher $\alpha_l$ and $k$. Higher pressure does also emphasize the difference in performance of the two geometries. The turbulence intensity in the vane pack is increasing at higher $k$. As described in section 3.2, a reduction of turbulence intensity has been one of the main objectives for the geo2 design. Turbulent fluctuations affect the droplet less at low pressure, due to the large density ratio and surface tension. When the pressure rises, the surface tension decreases, and thereby the stability of the droplet decreases. This might lead to easier fragmentation. If droplets are fragmented they will be more difficult to separate, due to the smaller inertia. The change in trajectory could direct the droplet against the wall or outwards from the wall, but this is hard to predict. By reducing the turbulent intensity, the droplet trajectory gets more predictable and thereby easier to separate. The chance for turbulence induced fragmentation will also be reduced. As already mentioned in section 3.2, a backflow was observed out of the drainage chamber on geo2. This was a major setback since it most likely reduced the performance of geo2.

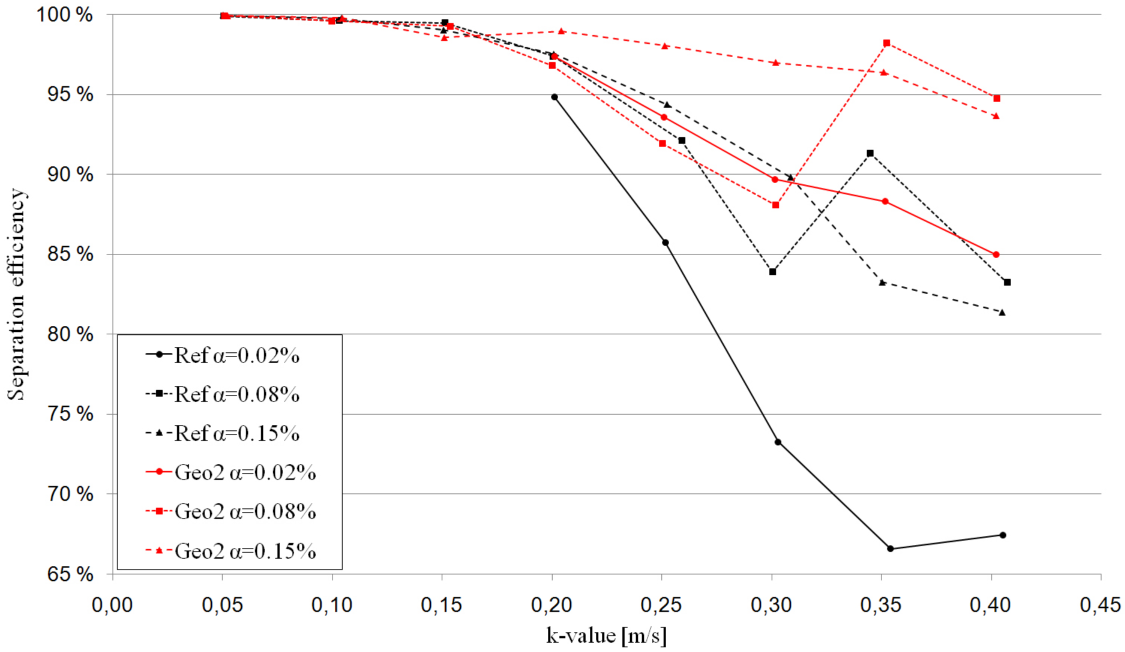

Figure 6.12: Separation efficiency of the reference geometry and geometry 2 at $p = 8barg$ and different liquid load plotted against k-value

Reducing LCO was the main objective for redesigning the reference geometry. LCO from geo2 relative to ref, $(1 - \eta_{geo2})/(1 - \eta_{ref})$, called LCO$_{rel}$, is plotted in figure 6.13. This means that test points with LCO$_{rel}$ $< 100\%$ are a reduction of LCO. Figure 6.13a shows LCO$_{rel}$ at $p = 1barg$. The performance of both geometries was as mentioned quite similar for both geometries at $k < 0.35$. Comparing LCO at a lower $k$ would involve a certaint uncertainty, because measuring errors and the standard deviation in the sampling might effect LCO$_{rel}$ much. The large value of LCO$_{rel}$ at $\alpha_l = 0.02\%$ at $k = 0.40$ is caused by the sudden fall in performance of geo2.

At $p = 4barg$ both geometries performed equally for $k \leqslant 0.15$, and LCO$_{rel}$ is therefore only commented for higher $k$. At $k > 0.15m/s$ geo2 has a clear reduction of LCO to approximately 25% for $\alpha_l = 0.15\%$ and to approximately 37% for $\alpha_l = 0.02\%$. The line for $\alpha_l = 0.08\%$ decrease gradually for $0.15 < k \leqslant 0.30m/s$ from 95% to 11%. The comparisson of LCO$_{rel}$ at this pressure emphasizes the better performance of geo2 shown in figure 6.11. One can roughly say that geo2 more than halves the LCO at higher $k$.

Figure 6.13c shows LCO$_{rel}$ at $p = 8barg$. Once again, due to the equal performance LCO$_{rel}$ will not be commented for $k < 0.20m/s$. At $\alpha_l = 0.02\%$ geo2 reduce LCO to 51% at $k = 0.20m/s$ and further down to 35% at $k = 35m/s$. LCO$_{rel}$ gradually decreases from 122% to 26% when $\alpha_l = 0.08\%$. The line for $\alpha_l = 0.15$ has a similar shape as at $p = 4barg$, but is staggered one test point to the right hand side. The result of LCO$_{rel}$ is in accordance with the result at $p = 4barg$.

Figure 6.13 visualizes the experimental results in a more practical fashion, and shows how the improvements turn out. Generally geo2 reduced LCO considerably at higher $k$. The reduction improves at higher pressure levels when $\alpha_l = 0.02\%$, which is the opposite case for $\alpha_l = 0.08\%$. The line for $\alpha_l = 0.15\%$ LCO$_{rel}$ shows the same trend and similar curvature at all pressure levels, but is staggered to a higher $k$ at higher pressure levels. The sudden increase and decrease in the line for $\alpha_l = 0.15\%$ can propably be ascribed to nozzle depedency, since it occurs between test points where the nozzle has been changed.

In scrubber in the oil and gas industry, the separation efficiency requirements for last stage demisting internals are very high, refer section 1.2. Typically the industry focuses on the performance above $97 - 98\%$. Figure 6.14 shows a close up of $\eta$ from $97 - 100\%$. All lines, except for $\alpha_l = 0.15\%$ due to the few test points, have a $\eta$ above 97% until $k \geqslant 0.30m/s$ where they suddenly decrease rapidly, figure 6.14a. The same trend, generally, can be found at $p = 4barg$ and $p = 8barg$, but at a lower $k$, $k \geqslant 0.15m/s$ and $k \geqslant 0.20m/s$ respectively. Geo2 with a $\alpha_l = 0.15$ separates from the other results and cross $\eta = 97\%$ at $k \geqslant 0.35m/s$ when $p = 4barg$ and at $k \geqslant 0.30m/s$ when $p = 8barg$. The results are plotted against $k$, which at some extent makes the plots independent of the pressure, because the effect of higher density is accounted for. It is however not right that $k$ ensures a pressure indepent study. Both the surface tension and the Kelvin helmholtz stability criterion for a wavy film are reduced at higher pressure. It was therefore expected that $\eta$ would cross 97% at a lower $k$ when the pressure level became higher, as the result for geo 2 with $\alpha_l = 0.15$ shows. Austrheim (2006) showed that the $We$ for the liquid film is a more suitable variable for achieving a pressure independent plot. Due to the lack of time this was not performed. Traditionally, separation experiments with vane pack are performed with water and air at low pressure (Verlaan, 1991). Based on this vane pack manufactorers claim a satisfactory $\eta$ up to $k = 0.20 - 0.25m/s$ (Natco, 2009). The experiments at $p = 1barg$ support this statement, but the experiments at $p = 4barg$ and

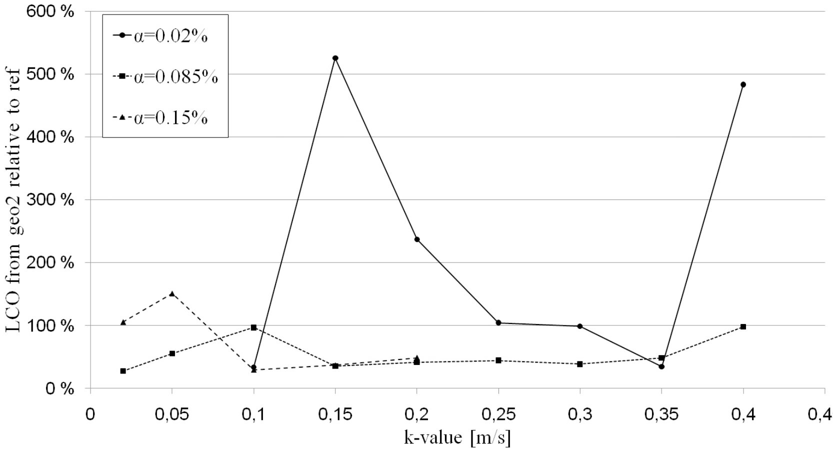

(a) $p = 1barg$

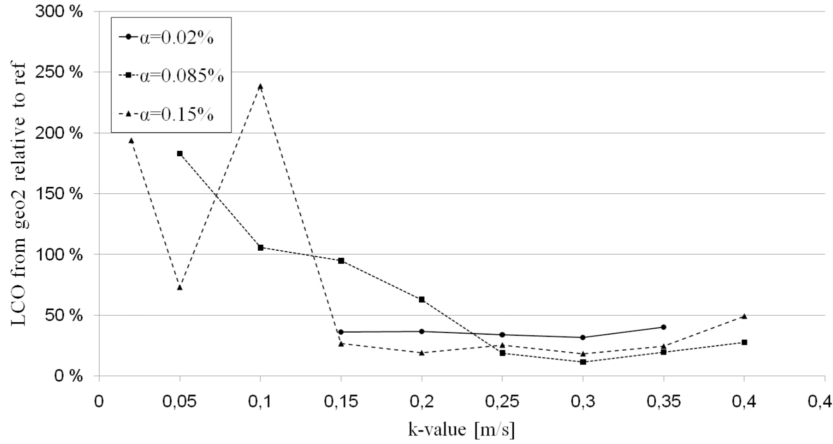

(b) $p = 4barg$

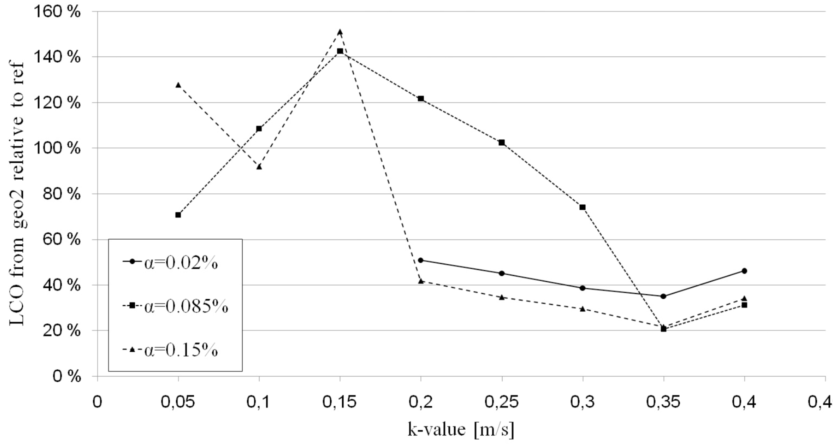

(c) $p = 8barg$

Figure 6.13: Comparing of LCO from the geometry 2 relative to the reference geometry

$p = 8barg$ show that this could be incorrect. Geo2 with $\alpha_l = 0.15\%$ is the only experiment which supports this claim.

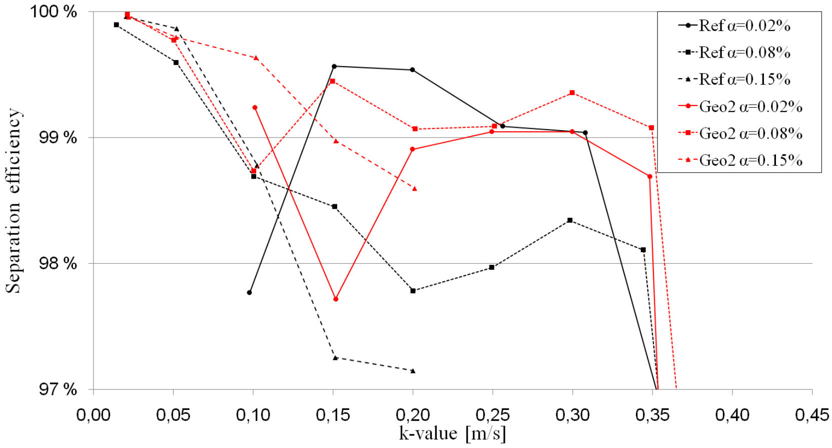

(a) $p = 1barg$

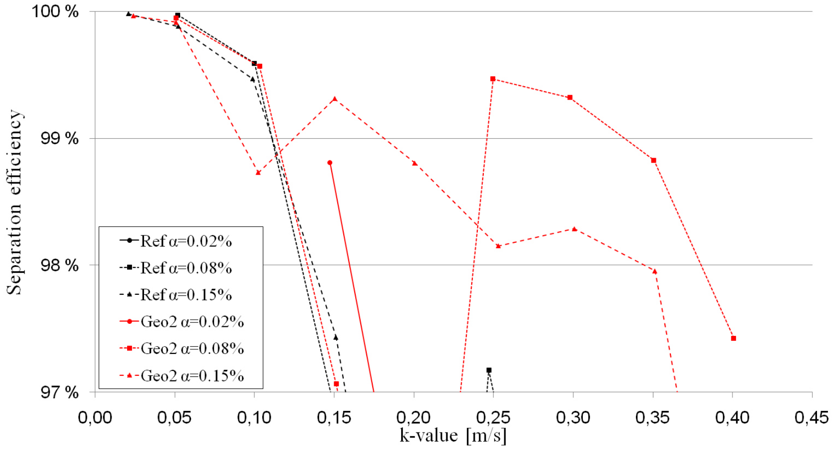

(b) $p = 4barg$

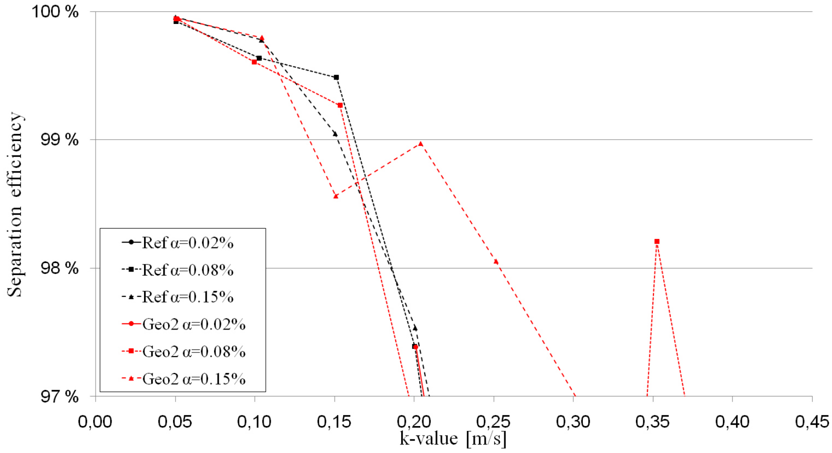

(c) $p = 8barg$

Figure 6.14: Close-up of the separation efficiency of the reference geometry and geometry 2 at different pressures and liquid load plotted against k-value

# Chapter 7

# Conclusion

Two vane packs have been studied, geometry 2 and the reference. Geometry 2 has a streamlined bends while the reference has sharp bends. Different transient turbulence models were compared for a simplified vane pack geometry. The standard SST model resolved no fluctuations, due to a high dissipation from the turbulent viscosity. The dissipating effects from the turbulent viscosity were also too large in the DES, due to a inappropriate grid for this model. SAS and LES were the only models that generated a turbulent three-dimensional solution and the mean velocities were almost congruent. The $P_{SAS}$ term in the SAS model worked as the developers said, it reduced the turbulent viscosity and promoted a unstable solution.

The design criteria for geometry 2 were to reduce the turbulence intensity and remove re-circulation zones, this were confirmed by the transient simulations. The predicted pressure loss using CFD for the reference geometry did not match the measured data, but the predicted pressure loss for geometry 2 was similar. Observations in the laboratory showed backflow from the drainage chambers, this was also confirmed by the one-phase simulation. The intention of the drainage chambers are to retain the droplets in the chamber, so this backflow is clearly a design defect. Several turbulent structures were reproduced by the one-phase simulation for the reference geometry.

The transient DPM simulation of the reference geometry showed a promising performance of the models for fragmentation and coalescence. The used wall-film model, gave an indication of where the droplets hit the wall and how the concentration of liquid on the wall are distributed. Re-entrainment from the film was only possible to generate at sharp bends, and the rate of re-entrainment was not possible to track. The fate of droplets that hit the wall are sharply divided into four regimes, based on the impact energy, and experiments indicates that the fate of the droplets have a more stochastic behavior. The simulation predicted a high separation efficiency, and was not trustworthy due to the wall-film models lack of capability to model re-entrainment from the liquid film. Droplet diameter distribution were plotted at each bend, and showed that the droplet diameter were reduced through the vane pack. The diameter cut-off was approximately $100 \mu m$ and in accordance with results from steady DPM simulations. Visual observation under the experiments with the reference vane pack confirmed the predicted droplet pattern. The simulation did indicated the pulsating behavior of the droplet stream in the vane pack.

The simulation of geometry 2, on a coarse grid and with a large time step, did not show satisfactory results and the droplet behavior was not well predicted. It was therefore not possible to compare the effect of the possible design improvements from the two simulation. A sufficiently large grid and well adjusted time step are crucial factors for a well calculated simulation.

The results from the experiments showed that both geometries had an equal performance at low k-values, generally $k < 0.15 m/s$. At low pressure, $p = 1 barg$, was the performance of both geometries congruent and the best performing geometry could therefore not be pointed out. In the high pressure experiments, $p = 4 barg$ and $p = 8 barg$, the performance of Geometry 2 was better at higher k-value and liquid volume fraction.

The mist flow were generated by a nozzle upstream the vane pack. The spread for the different nozzles were reduced at higher pressure, which impose an unevenly utilization of the channels, and increase the possibility for flooding of the drainage chambers. Droplets that hit the wall in the upstream channel were most likely counted as separated liquid and will therefore favor the low pressure experiments.

A common used separation efficiency criteria for natural scrubber is that the liquid carry over should be less than $13 l/MSm^3$. The criteria was not achieved at any pressure or liquid volume fraction, except at $k \leqslant 0.05 m/s$. Plots of the measured separation efficiency above 97%, showed a sharp decrese in efficiency at a certain k-value. The sharp decrease in efficiency appeared at a lower k-value at higher pressure. Separation efficiency fell below 97% at $k = 0.30 m/s$, $k = 0.15 m/s$ and $k = 0.20 m/s$, at a pressure of $p = 1 barg$, $p = 4 barg$ and $p = 8 barg$ respectively.

# Chapter 8

# Recommendations for further work

A study of the grid- and time- dependency of the transient discrete phase model, would improve the understanding of the model and minimize the number of CPU hours. Further study of the wall-film model and implementation of user defined functions might improve the models capability to predict re-entrainment from a wavy film.

Further development of the code that produce Rosin-Rammler diameter distributed and randomly spread droplets could give a more realistic and stochastic behavior of the droplet injection.

The streamlined geometry should be tested with drainage chambers that reduce the back-flow, this will most likely increase the performance.

Plot the results against $We$ for the liquid film to achieve pressure independent study. Improvements of the measurements in the laboratory might be achieved by a reduction of the boundary effects.

The liquid spread could be improved by changing the nozzle arrangement. Liquid that hit the upstream channel should be drained before the vane section, which could increase reliability of the measurement.

High speed photos of the channel to predict droplet diameter and trajectories, might improve the understanding of the droplet behavior.

The drainage pipes in the lab can be plugged, and the efficencies for the different sections in the vane packs can thereby be stated.

The oil and gas industry pratice the use of a mesh pad upstream vane packs. The effects of such a arrangement can be done in the existing lab. Perform experiments with a mesh pad downstream the liquid nozzle, to see if the efficiency increase due to larger droplets. The effects of surface tension can be tested by changing the liquid.

# Bibliography

In *Discussion with Dr. Richard Lechner, ANSYS software developer*, 2008.

J.E. Akin. Concepts of stress analysis with cosmoworks. September 2006.

Ansys. Turbulence workshop. Guthenburg, 28-30 October 2008. ANSYS.

Ansys. *Fluent version 12.0 userguide*, 2009.

Trond Austrheim. *Experimental characterization of high-pressure natural gas scrubbers.* PhD thesis, Univeristy of Bergen, Bergen, 2006.

Inc. BETE Fog Nozzle. *Spray manual.* BETE Fog Nozzle, Inc., 50 Greenfield Street Greenfield, MA 01301, 2009.

Alexandre H. M. Brigadeau. *Modeling and numerical investigation of high pressure gasliquid separation.* PhD thesis, Norwegian University of Science and Technology, Trondheim, September 2007.

Fredrik Carlson and Mauritz Talseth. Vane pack optimalization and rig setup for high pressure testing. Project thesis, Department of Energy and Process Engineering, NTNU, 2008.

CT Crowe. *Multiphase Flow Handbook.* 2006.

Lars Davidson. Evaluation of the sst-sas model: Channel flow, asymmetric diffuser and axi-symmetric hill. In *European Conference on Computational Fluid Dynamics*, 2006.

E O Doebelin. *Measurement Systems: Application and Design.* ISBN 0-07-100697-4. McGraw-Hill, fourth edition edition, 1990.

C. Duez. Making a splash with water repellency. *Nature Physics*, 3(3), 2007.

K. Feind. *Strömungsuntersuchungen bei gegenstrom von Rieselfilmen und Gas in lotrechten Rohren*. VDI-Verl., 1960.

F.Menter and Y.Egorov. *SAS Turbulence Modelling of Technical Flows*. Number Part XV. Springer Netherlands, 2006. ISBN 978-1-4020-5152-2.

FC Haas. Stability of droplets suddenly exposed to a high velocity gas stream. *Aiche Journal*, 10(6):920–924, 1964.

P.D. Hills. Designing piping for gravity flows. *Chemical Engineering*, 5 September 1983.

NI Kolev. *Multiphase Flow Dynamics 2*, volume 2nd edition. Springer Berlin/ Heidelberg, 2005.

FR Menter. Two-equation eddy-viscosity turbulence models for engineering applications. *AIAA journal*, 32(8), 1994.

Norway AS Natco. Sluppenveien 12E, 7035 Trondheim, 2009.

F Nicoud and F Ducros. Subgrid-scale stress modelling based on the square of the velocity gradient tensor. *Flow Turbulence and Combustion*, 62(3):183–200, 1999.

DH Norrie. *An introduction to finite element analysis*. Number ISBN-10: 0125216602. Academic Press Inc.,U.S., 1978.

NORSOK. Process systems, p-cr-001 rev.2. *Norwegian Technology Center*, 1996.

NORSOK. Process systems, p-100 rev.2. *Norwegian Technology Center*, 2001.

Oljedirektoratet. Fakta norsk petroleumsverksemd. *Olje- og energidepartementet*, 2008.

P.J. O'Rourke and A.A. Amsden. The tab method for numerical calculation of spray droplet breakup. Technical Report OSTI ID: 6118786, Los Alamos National Lab., NM (USA), 1987.

M. Pilch, C.A. Erdman, and Reynolds A.B. Acceleration induced fragmentation of liquid drops. Technical report NUREG/CR-2247, Department of Nuclear engineering University of Virginia, Charlottesville, VA 22901, March 1981.

U. Piomelli. Large-eddy simulation: achievements and challenges. *Progress in Aerospace Sciences*, 35(4):335–362, 1999.

Schroede.RR and RC Kintner. Oscillations of drops falling in a liquid field. *Aiche Journal*, 11(1):5–&, 1965.

Larry L. Simpson. Sizing piping for process plants. *Chemical Engineering*, 17 June 1968.

J Smagorinsky. General circulation experiments with the primitive equations. *Monthly Weather Review*, 91(3), 1963.

DW Stanton. Modeling fuel film formation and wall interaction in diesel engines. *SAE Technical Papers*, 1995.

Rombout Adriaan Swanborn. *A new approach to the design of gas-liquid separators for the oil industry*. PhD thesis, Delft University of Technology, S.l., 1988.

H. Tennekes and John L. Lumley. *A first course in turbulence*. MIT Press, Cambridge, Mass., c1972. ISBN 0-262-20019-8.

Cornelis Christoffel Johannes Verlaan. *Performance of novel mist eliminators*. PhD thesis, Delft University of Technology, Faculty of Mechanical Engineering and Marine Technology, S.l., 1991.

H.K. Versteeg. *An introduction to computational fluid dynamics : the finite volume method*. Number ISBN: 978-0-13-127498-3. Pearson Education Limited, second edition edition, 2007.

# Appendix A

# Grid

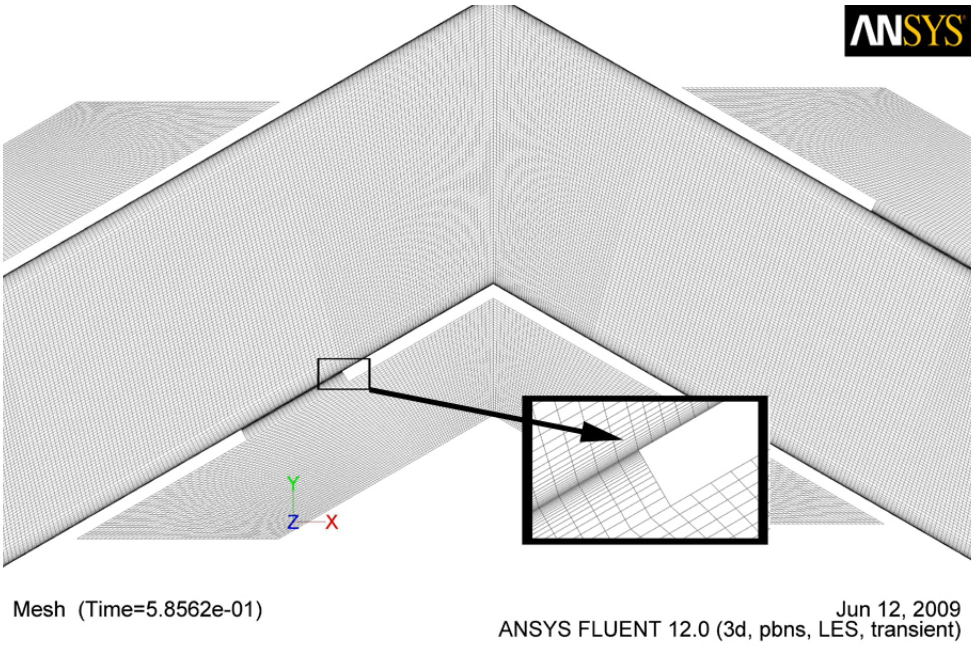

(a) Reference geometry

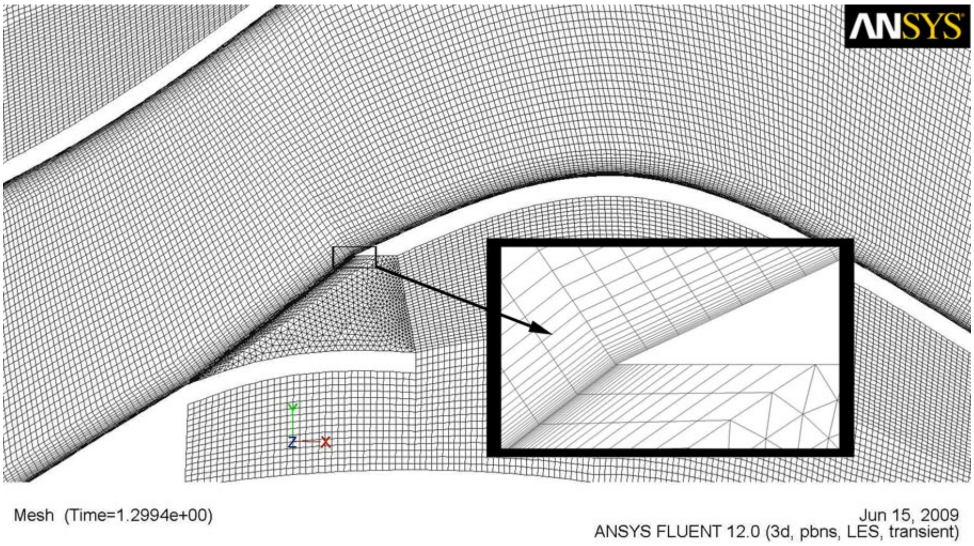

(b) Geometry 2

Figure A.1: Body-fitted grids for both geometries.

# Appendix B

# Nozzel data sheet

# P

## Fine Atomization

**Metal**

### DESIGN FEATURES

- High energy efficiency
- One-piece construction
- No whirl vanes or internal parts
- Highly efficient laminar jet impinges on target pin generating fine fog
- Male connection

### SPRAY CHARACTERISTICS

- Finest fog of any direct pressure nozzle
- Produces high percentage of droplets in the 25-400 micron range; ideal for dust suppression

**Spray pattern:** Cone-shaped Fog

**Spray angle:** 90°. For best 90° pattern operate nozzle at or above 4 bar

**Flow rates:** 0.153 to 30.3 l/min

Fog

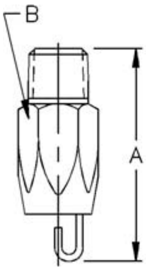

Male

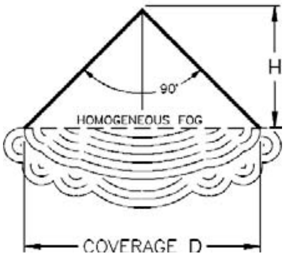

Fog Pattern

**Dimensions are approximate. Check with BETE for critical dimension applications.**

### *P Flow Rates and Dimensions*

*Cone-Shaped Fog, 90° Spray Angle, 1/4" Pipe Size, BSP or NPT*

| Male Pipe Size | Nozzle Number | K Factor | LITERS PER MINUTE @ BAR | | | | | | | | Approx. Orifice Dia. (mm) | Approx. Coverage (mm) D | Approx. Spray Height H (mm) | Approx. Dim. (mm) | | Wt. (g) Metal |
|---|---|---|---|---|---|---|---|---|---|---|---|---|---|---|---|---|
| | | | 1 bar | 2 bar | 3 bar | 5 bar | 7 bar | 10 bar | 20 bar | 30 bar | | | | A | B | |
| 1/4 | **P20** | 0.153 | 0.153 | 0.216 | 0.264 | 0.341 | 0.404 | 0.483 | 0.683 | 0.836 | 0.508 | 300 | 150 | 46.5 | 16.0 | 57 |
| | **P24** | 0.228 | 0.228 | 0.322 | 0.395 | 0.510 | 0.603 | 0.721 | 1.02 | 1.25 | 0.610 | 400 | 200 | | | |
| | **P28** | 0.296 | 0.296 | 0.419 | 0.513 | 0.662 | 0.784 | 0.937 | 1.32 | 1.62 | 0.711 | 460 | 230 | | | |
| | **P32** | 0.410 | 0.410 | 0.580 | 0.710 | 0.917 | 1.09 | 1.30 | 1.83 | 2.25 | 0.813 | 560 | 280 | | | |
| | **P40** | 0.638 | 0.638 | 0.902 | 1.11 | 1.43 | 1.69 | 2.02 | 2.85 | 3.49 | 1.02 | 610 | 305 | | | |
| | **P48** | 0.912 | 0.912 | 1.29 | 1.58 | 2.04 | 2.41 | 2.88 | 4.08 | 4.99 | 1.22 | 710 | 355 | | | |
| | **P54** | 1.21 | 1.21 | 1.71 | 2.09 | 2.70 | 3.20 | 3.82 | 5.40 | 6.62 | 1.37 | 760 | 380 | | | |
| | **P66** | 1.71 | 1.71 | 2.42 | 2.96 | 3.82 | 4.52 | 5.40 | 7.64 | 9.36 | 1.68 | 910 | 455 | | | |
| | **P80** | 2.46 | 2.46 | 3.48 | 4.26 | 5.50 | 6.51 | 7.78 | 11.0 | 13.5 | 2.03 | 1200 | 600 | | | |
| | **P120** | 5.54 | 5.54 | 7.83 | 9.59 | 12.4 | 14.7 | 17.5 | 24.8 | 30.3 | 3.05 | 1500 | 750 | | | |

*Flow Rate* $(l/\text{min}) = K\sqrt{bar}$

**Standard Materials: Brass, 303 Stainless Steel and 316 Stainless Steel.**

**Spray angle performance varies with pressure. Contact BETE for specific data on critical applications.**

***TO ORDER:** specify pipe size, connection type, nozzle number, spray angle, and material.*

# Appendix C

# Uncertainty of laboratory equipment

# Measurements and accuracy in the laboratory

| Name | Range | Accuracy | Comments |
|---|---|---|---|
| $P_{Qgas}$ | 0 – 10 barg | ± 7.5mbar | Measuring pressure (barg) upstream of gas metering orifice |
| $P_{Testbox}$ | 0 – 40 barg | ± 15mbar | Measuring absolute pressure (bara) at inlet of the vane pack section |
| $\Delta P_{Qgas}$ | 0 – 1 bar | ± 0.75mbar | Measuring pressure drop (bar) across gas metering orifice |
| $\Delta P_{Nozzle}$ | 0 – 10 bar | ± 15mbar | Measuring pressure drop (bar) across liquid injection nozzles |
| $T_{gass}$ | 0 – 100 °C | ± 0.1°C | Measuring gas temperature downstream of gas metering orifice |

Table with range and accuracy of the instruments used under the tests

| Name | Unit | Value | Accuracy | Comment |
|---|---|---|---|---|
| MW SF6 | (kg/kmol) | 146 | ± 3.0 | Molweight SF6 |
| D throat | (m) | 0.0350 | ± 0.00020 | Diameter in metering orifice |
| D pipe | (m) | 0.0445 | ± 0.00020 | Pipe Diameter in metering section |
| Cd | (-) | 0.59 | ± 0.02 | Drag coefficient gas measurement |
| Kappa SF6 | (-) | 1.1 | ± 0.05 | |
| □ liq | ($kg/m^3$) | 780 | ± 7.0 | Liquid density ExxsolD60 |
| $k_{nozzle}$ | (-) | Varies | ± 3 % | Pressure drop coefficient nozzles |
| $h_1$ | (mm) | Varies | ± 1 | Start height measuring liquid carry over |
| $h_2$ | (mm) | Varies | ± 1 | End height measuring liquid carry over |
| t | (sec) | Varies | ± 2 | Time from start to end of carry over measurement |

Table with values and accuracy of used numbers in calculations.

## Equations used for measurements and accuracy evaluation

The gas mass flow rate is calculated from the following equation:

$$\dot{m} = \frac{E\cdot C_d \cdot A_t \cdot \sqrt{2\cdot\rho\cdot\Delta P_{gas}}}{(1-\mathrm{B}^4)^{0.5}}$$

$$E = 1 - \frac{(0.41+0.35\cdot B^4)\Delta P_{Q_{gas}}}{(\kappa\cdot \mathrm{P}_{\mathrm{Q}_{\mathrm{gas}}})}$$

$$\rho = \frac{(P_{\mathrm{Q}_{\mathrm{gas}}} + P_{std})MW}{\overline{R}\cdot(T+273.9)\cdot Z}$$

$$B = \frac{D_{troat}}{D_{pipe}}$$

The error in the derived variables is expressed as:

$$\Delta B = \frac{\partial B}{\partial D_t}\Delta D_t + \frac{\partial B}{\partial D_p}\Delta D_p = \frac{1}{D_p}\Delta D_t + \frac{D_t}{D_t^2}\Delta D_t$$

$$\Delta E = \frac{\partial E}{\partial B}\cdot\Delta B + \frac{\partial E}{\partial \Delta P}\cdot\Delta\Delta P + \frac{\partial E}{\partial \kappa}\cdot\Delta\kappa + \frac{\partial E}{\partial P_{Q_{gas}}}\cdot\Delta P_{Q_{gas}}$$

$$\Delta E = \frac{0.35\cdot\Delta P\cdot 4\cdot B^3}{\kappa\cdot P_{Q_{gas}}}\cdot\Delta B + \frac{(0.41+0.35\cdot B^4)}{\kappa\cdot P_{Q_{gas}}}\cdot\Delta\Delta P_{Q_{gas}} + \frac{(0.41+0.35\cdot B^4)}{\kappa\cdot P_{Q_{gas}}{}^2}\cdot\Delta P_{Q_{gas}} + \frac{(0.41+0.35\cdot B^4)}{P_{Q_{gas}}\cdot\kappa^2}\cdot\Delta\kappa$$

$$\rho = \frac{(P_{\mathrm{Q}_{\mathrm{gas}}} + P_{std})MW}{\overline{R}\cdot(T+273.9)}$$

$$\Delta\rho = \frac{\partial\rho}{\partial P_{\mathrm{Q}_{\mathrm{gas}}}}\Delta P_{\mathrm{Q}_{\mathrm{gas}}} + \frac{\partial\rho}{\partial MW}\Delta MW + \frac{\partial\rho}{\partial T}\Delta T$$

$$\Rightarrow \Delta\rho = \frac{MW}{\overline{R}\cdot(T+273.9)}\Delta P_{Q_{gas}} + \frac{(P_{\mathrm{Q}_{\mathrm{gas}}} + P_{std})}{\overline{R}\cdot(T+273.9)}\Delta MW + \frac{(P_{\mathrm{Q}_{\mathrm{gas}}} + P_{std})\cdot MW}{2\cdot\overline{R}\cdot(T+273.9)^2}\Delta T$$

$$\Delta\dot{m} = \frac{\partial Q_m}{\partial E}\cdot\Delta E + \frac{\partial Q_m}{\partial C_d}\cdot\Delta C_d + \frac{\partial Q_m}{\partial A_t}\cdot\Delta A_t + \frac{\partial Q_m}{\partial \rho}\cdot\Delta\rho + \frac{\partial Q_m}{\partial \Delta P}\cdot\Delta\Delta P + \frac{\partial Q_m}{\partial B}\cdot\Delta B$$

$$\Delta\dot{m}_m = \frac{C_d\cdot A_t\cdot\sqrt{2\cdot\rho\cdot\Delta P_{Q_{gas}}}}{(1-\mathrm{B}^4)^{0.5}}\cdot\Delta E + \frac{EA_t\cdot\sqrt{2\cdot\rho\cdot\Delta P_{Q_{gas}}}}{(1-\mathrm{B}^4)^{0.5}}\cdot\Delta C_d + \frac{EC_d\cdot\sqrt{2\cdot\rho\cdot\Delta P_{Q_{gas}}}}{(1-\mathrm{B}^4)^{0.5}}\cdot\Delta A_t +$$

$$\frac{EC_d\cdot A_t\cdot 2\cdot\Delta P_{Q_{gas}}}{(1-\mathrm{B}^4)^{0.5}\cdot\sqrt{2\cdot\rho\cdot\Delta P_{Q_{gas}}}}\cdot\Delta\rho + \frac{EC_d\cdot A_t\cdot 2\cdot\rho}{(1-\mathrm{B}^4)^{0.5}\cdot\sqrt{2\cdot\rho\cdot\Delta P_{Q_{gas}}}}\cdot\Delta\Delta P_{Q_{gas}} +$$

$$\frac{E\cdot C_d\cdot A_t\cdot\sqrt{2\cdot\rho\cdot\Delta P_{Q_{gas}}}\cdot 4B^3}{(1-\mathrm{B}^4)^{1.5}}\cdot\Delta B$$

$$Q_{gas} = \frac{\dot{m}}{\rho}$$

$$\Delta Q_{gas} = \frac{1}{\rho}\cdot\Delta\dot{m} + \frac{\dot{m}}{\rho^2}\Delta\rho$$

The separated liquid and liquid carry over are calculated from the following equation:

$$V = \frac{\pi}{4}D_{pipe}{}^2(h_2 - h_1)$$

$$h = h_2 - h_1$$

$$Q = \frac{V}{t}$$

$$Q_{liquid\_injection} = Q_{separated\_liquid} + Q_{LCO}$$

The error in the derived variables is expressed as:

$$\Delta V = \frac{\pi}{2}\cdot D_{pipe}\cdot\Delta D_{pipe}(h_2 - h_1) + \frac{\pi}{4}\cdot D_{pipe}{}^2(\Delta h_2 + \Delta h_1)$$

$$\Delta Q = \frac{1}{t}\Delta V + \frac{V}{t^2}\Delta t$$

$$\Delta Q_{liquid\_injection} = \Delta Q_{separated\_liquid} + \Delta Q_{LCO}$$

$h_1$ and $h_2$ are the height from where the measurements are started. The accuracy is ± 1mm.

t = ± 1 sec

Separation efficiency is defined as:

$$\eta = \frac{Q_{separated\_liquid}}{Q_{liquid\_injection}} = 1 - \frac{Q_{liquid\_carry\_over}}{Q_{liquid\_injection}}$$

The efficiency error is expressed as:

$$\Delta\eta = \frac{1}{Q_{liquid\_injection}} \cdot \Delta Q_{LCO} + \frac{Q_{LCO}}{Q_{liquid\_injection}{}^{2}} \cdot \Delta Q_{liquid\_injection}$$

# Appendix D

# Visual Basic code: Importing CFD data

This code was written in Microsoft Visual Basic, for importing data files from the desktop computer and the Linux cluster. A data file contains velocity or turbulent kinetic energy at different lines. Shortly described the code imports the data to a variable, then splits the variable into a vector at the character ENTER. Then it seek the type of delimiter that has been used, which is different from Windows and Linux. Then it sorts the different data for each line into different excel documents. A progress bar was added to the code since it has been optimized. And the time to import 20.000 data files was reduce by almost a factor of 1000, by reducing the amount of times VBA had to write to excel. To save even more time the VBA code was saved as a dll file, meaning that the VBA avoids to compile the code each time it is being used. The time it now uses is mostly because it needs to open and close the data files it read from.

```
Option Explicit
Sub LesFraEnTekstFil()
On Error GoTo ExitHere
Dim fs As Scripting.FileSystemObject, f As Scripting.TextStream
Dim m_colTimer As New Collection
Dim m_Timer As clsTimer
Set m_Timer = New clsTimer
m_Timer.ResetTimer
Dim ExecutionTime As Variant
Dim inputpath As String 'inputpath
Dim filenames As String 'name of the files
Dim timesteps As String 'how many sample data are available
Dim Outputfile1 As String 'Name of outfile 1
Dim Outputfile2 As String 'Name of outfile 2
Dim Outputfile3 As String 'Name of outfile 3
Dim Outputfile4 As String 'Name of outfile 4
Dim Outputfile5 As String 'Name of outfile 5
Dim skip As Long 'if the statistical data shall be achieved by skipping some data
Dim m As Long 'counter for number of available time steps
Dim n1 As Long 'nr of points at line1
Dim n2 As Long 'nr of points at line2
Dim n3 As Long 'nr of points at line3
Dim n4 As Long 'nr of points at line4
Dim n5 As Long 'nr of points at line5
Dim i As Long 'counter for non usable data
Dim q As Long 'help counter for where to print
Dim d As Long 'help counter
Dim inputfile As String 'the total path and filename with extension
Dim dump 'position to dump non ustable data
Dim pos As Variant 'y-position for the velocity data
Dim vel As Variant 'velocity data at a spsific y-position
Dim start_print As Long 'specifies where to start printing the vel data
Dim start_print_pos As Long 'specifies where to print the pos data
Dim a As Long, aSheet1, aSheet2, aSheet3, aSheet4, aSheet5
Dim l As Long
Dim nr_of_first_file
Dim strVel As String, aOut As Variant, ant, linje As Long, aOut2
Dim NyLine As Boolean, Søkestreng As String, FilTekst As String

inputpath = Cells(2, 2) 'the path of the files
filenames = Cells(3, 2)
nr_of_first_file = MainSheet.Cells(7, 2) 'The number of the first timestep dumped
timesteps = Cells(4, 2) 'how many timesteps do you have data for
skip = Cells(5, 5) 'how many timestep do you want to skip to achive statistical data
Outputfile1 = Cells(2, 7) 'The file for line1
Outputfile2 = Cells(3, 7) 'The file for line2
Outputfile3 = Cells(4, 7) 'The file for line3
Outputfile4 = Cells(5, 7) 'The file for line4
Outputfile5 = Cells(6, 7) 'The file for line5
start_print = Cells(8, 5) 'Where to start print in the outfiles
```

```
start_print_pos = Cells(7, 5) 'Where to print the position vector in the outfiles
frmProgressBar.LabelProgress.Width = 0
frmProgressBar.Label3 = "Excecution time..."
frmProgressBar.Show False
Excel.Application.ScreenUpdating = False
ReDim aSheet1(1 To timesteps, 1 To 250) 'resize the dynamic array
ReDim aSheet2(1 To timesteps, 1 To 250) 'resize the dynamic array
ReDim aSheet3(1 To timesteps, 1 To 250) 'resize the dynamic array
ReDim aSheet4(1 To timesteps, 1 To 250) 'resize the dynamic array
ReDim aSheet5(1 To timesteps, 1 To 250) 'resize the dynamic array
ReDim posVec1(1 To 1, 1 To 250) 'resize the dynamic array
ReDim posVec2(1 To 1, 1 To 250) 'resize the dynamic array
ReDim posVec3(1 To 1, 1 To 250) 'resize the dynamic array
ReDim posVec4(1 To 1, 1 To 250) 'resize the dynamic array
ReDim posVec5(1 To 1, 1 To 250) 'resize the dynamic array

For m = 1 To timesteps Step skip 'Runs through all the data files
    q = m + nr_of_first_file - 1 'A counter that starts at your first data file
    inputfile = inputpath + filenames + VBA.Format(q, "0000") + ".txt"
    d = VBA.Len(VBA.Dir(inputfile)) 'if file exsist bigger than 1
    If d > 1 Then 'checks if the file exists
    frmProgressBar.Label1 = filenames + VBA.Format(q, "0000") + ".txt"
    Call updateProgressbar(VBA.CLng(m), VBA.CLng(timesteps))
    linje = 0 'resets case
    Set fs = New FileSystemObject
    Set f = fs.OpenTextFile(inputfile, ForReading, False)
    With f
        l = 0
        strVel = .ReadAll ' put all content in d
        aOut = VBA.Split(strVel, VBA.Chr(10)) 'splits the content on ENTER

        For l = 1 To UBound(aOut) 'runs through aOut
            'Check if tab is included in text string
            If VBA.InStr(1, aOut(l), VBA.Chr(9)) = 0 Then
                ReDim aOut2(0 To 0)
                aOut2(0) = aOut(l) 'No tab is found

            ElseIf VBA.InStr(1, aOut(l), VBA.Chr(9)) <> 0 Then
                aOut2 = VBA.Split(aOut(l), VBA.Chr(9)) 'tab found
            Else
                ReDim aOut2(0 To 0)
                aOut2(0) = aOut(l) 'No tab is found
            End If
            ant = UBound(aOut2)
            Dim strLen As Long
            If l < UBound(aOut) Then
                strLen = VBA.Len(aOut2(0))
                If strLen > 1 Then 'Remove linefeed if found
                    If VBA.InStr(strLen, aOut2(0), VBA.Chr(13)) <> 0 Then
                        aOut2(0) = VBA.Left(aOut2(0), strLen - 1)
```

```
        End If
    End If

    aOut2(0) = VBA.Trim(aOut2(0))
    FilTekst = VBA.Right(aOut2(0), 3)
    Søkestreng = VBA.CStr(linje + 1) & Chr(34) & ")"

    If VBA.InStr(1, FilTekst, VBA.Chr(10)) = 0 Then
        FilTekst = FilTekst "i.e no linefeed found
    Else
        FilTekst = VBA.Replace(FilTekst, VBA.Chr(10), "")
    End If

    If VBA.InStr(1, FilTekst, VBA.Chr(13)) = 0 Then
        FilTekst = FilTekst
    Else
        FilTekst = VBA.Replace(FilTekst, VBA.Chr(13), "")
    End If

    If FilTekst = Søkestreng Or l = UBound(aOut) Then
        NyLine = True
    Else
        NyLine = False
    End If
ElseIf l = UBound(aOut) Then
    NyLine = True
End If

If ant >= 0 Or l = UBound(aOut) Then
    If NyLine Then
        linje = linje + 1
    End If
End If

frmProgressBar.Label2 = "Linjenr.: " & VBA.CStr(linje)
Call updateProgressbar2(VBA.CLng(l), VBA.CLng(UBound(aOut)))


If ant > 0 Then

    If VBA.IsNumeric(aOut2(0)) Then
        pos = VBA.CDbl(aOut2(0))
        vel = VBA.CDbl(aOut2(1))
        If m = 1 Then 'writes the position in the excel doc.only _
        needed for one timestep

            Select Case linje 'places each line in the correct matrix
                Case 1
                    n1 = n1 + 1
                    aSheet1(m, n1) = vel
```

```
                                posVec1(m, n1) = pos
                            Case 2
                                n2 = n2 + 1
                                aSheet2(m, n2) = vel
                                posVec2(m, n2) = pos
                            Case 3
                                n3 = n3 + 1
                                aSheet3(m, n3) = vel
                                posVec3(m, n3) = pos
                            Case 4
                                n4 = n4 + 1
                                aSheet4(m, n4) = vel
                                posVec4(m, n4) = pos
                            Case 5
                                n5 = n5 + 1
                                aSheet5(m, n5) = vel
                                posVec5(m, n5) = pos
                            End Select
                        Else
                        Select Case linje
                            Case 1
                                n1 = n1 + 1
                                aSheet1(m, n1) = vel
                            Case 2
                                n2 = n2 + 1
                                aSheet2(m, n2) = vel
                            Case 3
                                n3 = n3 + 1
                                aSheet3(m, n3) = vel
                            Case 4
                                n4 = n4 + 1
                                aSheet4(m, n4) = vel
                            Case 5
                                n5 = n5 + 1
                                aSheet5(m, n5) = vel
                        End Select
                    End If
                End If
            End If
        Next l
        .Close
    End With
    Set f = Nothing
    Set fs = Nothing
    Else
    a = 1
    End If
If m = timesteps Then
        If n1 = 0 Then n1 = 1
        If n2 = 0 Then n2 = 1
```

```
        If n3 = 0 Then n3 = 1
        If n4 = 0 Then n4 = 1
        If n5 = 0 Then n5 = 1

        ReDim Preserve aSheet1(1 To timesteps, 1 To n1)
        Workbooks(Outputfile1) _
        .Worksheets(1).Cells(start_print, 3).Resize(timesteps, n1) = aSheet1
        ReDim Preserve posVec1(1 To 1, 1 To n1)
        Workbooks(Outputfile1) _
        .Worksheets(1).Cells(start_print_pos, 3).Resize(1, n1) = posVec1

        ReDim Preserve aSheet2(1 To timesteps, 1 To n2)
        Workbooks(Outputfile2) _
        .Worksheets(1).Cells(start_print, 3).Resize(timesteps, n2) = aSheet2
        ReDim Preserve posVec2(1 To 1, 1 To n2)
        Workbooks(Outputfile2) _
        .Worksheets(1).Cells(start_print_pos, 3).Resize(1, n2) = posVec2

        ReDim Preserve aSheet3(1 To timesteps, 1 To n3)
        Workbooks(Outputfile3) _
        .Worksheets(1).Cells(start_print, 3).Resize(timesteps, n3) = aSheet3
        ReDim Preserve posVec3(1 To 1, 1 To n3)
        Workbooks(Outputfile3) _
        .Worksheets(1).Cells(start_print_pos, 3).Resize(1, n3) = posVec3

        ReDim Preserve aSheet4(1 To timesteps, 1 To n4)
        Workbooks(Outputfile4) _
        .Worksheets(1).Cells(start_print, 3).Resize(timesteps, n4) = aSheet4
        ReDim Preserve posVec4(1 To 1, 1 To n4)
        Workbooks(Outputfile4) _
        .Worksheets(1).Cells(start_print_pos, 3).Resize(1, n4) = posVec4

        ReDim Preserve aSheet5(1 To timesteps, 1 To n5)
        Workbooks(Outputfile5) _
        .Worksheets(1).Cells(start_print, 3).Resize(timesteps, n5) = aSheet5
        ReDim Preserve posVec5(1 To 1, 1 To n5)
        Workbooks(Outputfile5) _
        .Worksheets(1).Cells(start_print_pos, 3).Resize(1, n5) = posVec5

    End If

    n1 = 0
    n2 = 0
    n3 = 0
    n4 = 0
    n5 = 0

    Next m
```

```
m_Timer.StopTimer
m_colTimer.Add m_Timer.Elapsed

ExecutionTime = "Total time: " & vbTab & VBA.Format(m_colTimer(1) / 1000, "0.000 s")

frmProgressBar.CommandButton1.Visible = True
frmProgressBar.Label3 = ExecutionTime
Set m_Timer = Nothing
Excel.Application.ScreenUpdating = True
'frmProgressBar.Hide
Exit Sub
ExitHere:
   m_Timer.StopTimer
   m_colTimer.Add m_Timer.Elapsed
   ExecutionTime = "Total time: " & VBA.vbTab & VBA.Format(m_colTimer(1) / 1000, "0.000 s")

   frmProgressBar.CommandButton1.Visible = True
   frmProgressBar.Label3 = "Excecution error!!" & VBA.vbLf & ExecutionTime
   Set m_Timer = Nothing
   Excel.Application.ScreenUpdating = True
   'frmProgressBar.Hide
End Sub
----------------------------------------------------------------------------------------------------------
Private Sub updateProgressbar(it As Long, totIteration As Long)
Dim counter As Long
Dim PctDone As Double
counter = it
PctDone = counter / totIteration '(RowMax * ColMax)
With frmProgressBar
   .FrameProgress.Caption = VBA.Format(PctDone, "0%")
   .LabelProgress.Width = PctDone * (.FrameProgress.Width - 10)
End With
'      The DoEvents statement is responsible for the form updating
       DoEvents
End Sub
----------------------------------------------------------------------------------------------------------
Private Sub updateProgressbar2(it As Long, totIteration As Long)
Dim counter As Long
Dim PctDone As Double
counter = it
PctDone = counter / totIteration '(RowMax * ColMax)
With frmProgressBar
   .FrameProgress2.Caption = VBA.Format(PctDone, "0%")
   .LabelProgress2.Width = PctDone * (.FrameProgress.Width - 10)
End With
'      The DoEvents statement is responsible for the form updating
       DoEvents

End Sub
```

# Appendix E

# Visual Basic Code: Generating droplet profil

```
Option Explicit
Sub outfile()

'This sub rouine creates a droplet profile for Fluent DPM injections
'The the droplet profile has a rosin rammler distribution and the droplets are _
randomly spread in the given plane

'Declares all the used variables inthe routine
Dim rowNo#
Dim rngLastRow As Excel.Range
Dim m_timestep As Double, m_flowrate As Double, d_mean As Double, dens_exxsol As Double
Dim n_spread As Double, pi As Double, height As Double, wid As Double, m_fractot As Double
Dim mtot As Double, Rn As Double, root As Double, d As Double, m_d As Double, m_frac As Double
Dim c As Double
Dim wid_step As Double, w As Double
Dim counter As Long, s As Long, m As Long, h As Long, num As Long, k As Long
Dim Leftcol As String, rightcol As String
Dim PctDone As Single



'Prepares the size of the progressbar
Set rngLastRow = Me.Range("rngStartOutput").End(xlDown)
rngLastRow = rngLastRow.Row

rowNo = rngLastRow - Me.Range("rngStartOutput").Row + 1

Me.Range("rngStartOutput").Resize(rowNo, 9).ClearContents

'This section collects all the parameters for the droplet profile
m_timestep = Sheet1.Cells(20, 2)                    'The liquid flow for one timestep
m_flowrate = Sheet1.Cells(19, 2)                    'The liquid flowrate
counter = 0                                         'Initialize the counter
d_mean = Sheet1.Cells(7, 2)                         'The mean diameter of the droplets
dens_exxsol = Sheet1.Cells(11, 2)                   'Density of the liquid
n_spread = Sheet1.Cells(8, 2)                       'The spread of the diameter
pi = WorksheetFunction.pi
height = Sheet1.Cells(27, 2) - Sheet1.Cells(26, 2)
wid = Sheet1.Cells(29, 2) - Sheet1.Cells(28, 2)


'This section sets the random number start point, based on the CPU clock
s = Second(Time)
m = 60 * Minute(Time)
h = Hour(Time)
num = s * m * h
Randomize [num]
m_fractot = 0

'Starting the progress bar
frmProgressBar.LabelProgress.Width = 0
frmProgressBar.Label1 = "Making Rosin-ramler distributed diameter"
frmProgressBar.Show False

'This while loop makes the Rosin-ramler distributed diameter
'The loop will continue until mass of the droplets exceed the total mass for one timestep
Do While mtot < m_timestep
        Rn = (Int((10 ^ 6 - 0 + 1) * Rnd + 0)) / 10 ^ 6
        root = -VBA.Math.Log(Rn)
       ' d = 175
       d = d_mean * (root) ^ (1 / n_spread)     'Making the diameter for one droplet
        counter = counter + 1
        m_d = pi / 6 * (d * 10 ^ (-6)) ^ 3 * dens_exxsol    'Calculating the mass of the droplet
        m_frac = m_d / m_timestep
        mtot = mtot + m_d                                   'Summarize the total mass of the made drop
let
        m_fractot = m_fractot + m_frac
        Sheet1.Cells(50 + counter, 10) = d * 10 ^ (-6)
         Sheet1.Cells(50 + counter, 11) = 300
        Sheet1.Cells(50 + counter, 12) = m_frac * m_flowrate
```

```
        PctDone = mtot / (m_timestep)
        With frmProgressBar
            .FrameProgress.Caption = Format(PctDone, "0%")
            .LabelProgress.Width = PctDone * (.FrameProgress.Width - 10)
        End With
'       The DoEvents statement is responsible for the form updating
        DoEvents

    Loop

Unload frmProgressBar
Sheet1.Cells(48, 6) = counter
wid_step = wid / 5
c = 1
w = wid_step / 2
'Restarting the progress bar
frmProgressBar.LabelProgress.Width = 0
frmProgressBar.Label1 = "Making random coordinates for the droplets"
frmProgressBar.Show False
Leftcol = Sheet1.Cells(30, 1)
rightcol = Sheet1.Cells(30, 2)
'This while loop makes the random coordinates for the droplets
For k = 1 To counter
            Rn = (Int((10 ^ 6 - 0 + 1) * Rnd + 0)) / 10 ^ 6
            w = wid * Rn
            Rn = (Int((10 ^ 6 - 0 + 1) * Rnd + 0)) / 10 ^ 6
            h = height * Rn + Sheet1.Cells(26, 2)
            Sheet1.Cells(50 + c + k - 1, 3) = Leftcol
            Sheet1.Cells(50 + c + k - 1, 4) = 5 / 1000
            Sheet1.Cells(50 + c + k - 1, 5) = h / 1000
            Sheet1.Cells(50 + c + k - 1, 6) = w / 1000
            Sheet1.Cells(50 + c + k - 1, 7) = 1.013078
            Sheet1.Cells(50 + c + k - 1, 8) = 0
            Sheet1.Cells(50 + c + k - 1, 9) = 0
            Sheet1.Cells(50 + c + k - 1, 13) = rightcol

              PctDone = k / (counter)
        With frmProgressBar
            .FrameProgress.Caption = Format(PctDone, "0%")
            .LabelProgress.Width = PctDone * (.FrameProgress.Width - 10)
        End With
'       The DoEvents statement is responsible for the form updating
        DoEvents
Next k
Unload frmProgressBar
End Sub
```